Two phase magnetoelectric epitaxial composite thin films

Li Yan

Dissertation submitted to the faculty of the
Virginia Polytechnic Institute and State University
In partial fulfillment of the requirement for the degree of
Doctor of Philosophy
In
Materials Science and Engineering

Dwight D. Viehland (Chair)
JieFang Li
David Clark
Shashank Priya

November 3rd, 2009
Blacksburg, Virginia

Keywords: Magnetoelectric, multiferroic, ferroelectric, ferromagnetic, piezoelectric, magnetostrictive, self-assemble, epitaxial, composite, thin film, pulsed laser deposition, x-ray diffraction, piezoresponse force microscopy, magnetic force microscopy, focused ion beam, lithography

Two phase magnetoelectric epitaxial composite thin films

Li Yan

Abstract

Magnetoelectricity (ME) is a physical property that results from an exchange between polar (electric dipole) and spin (magnetic dipole) subsystem: i.e., a change in polarization (P) with application of magnetic field (H), or a change in magnetization (M) with applied electric field (E). Magnetoelectricity can be found both in single phase and composite materials. Compared with single phase multiferroic materials, composite multiferroics have higher ME effects. Through a strictive interaction between the piezoelectricity of the ferroelectric phase and the magnetostriction of the ferromagnetic phase, said multiferroic composites are capable of producing relatively large ME coefficients.

This Dissertation focused on the deposition and characterization of two-phase composite magnetoelectric thin films. First, single phase ferroelectric thin films were studied to improve the multiferroic properties of the composite thin films. Then structural, ferroelectric, ferromagnetic, and magnetoelectric properties of composite thin films were researched. Finally, regular nano-array composite films were deposited and characterized.

First, for single phase ferroelectric thin films, the phase stability was controlled by epitaxial engineering. Because ferroelectric properties are strongly related to their crystal structure, it is necessary to study the crystal structures in single phase ferroelectric thin films. Through constraint of the substrates, the phase stability of the ferroelectric thin films were able to be altered. Epitaxial thin-layers of $Pb(Fe_{1/2}Nb_{1/2})O_3$ (or PFN) grown on (001), (110), and (111) $SrTiO_3$ substrates are tetragonal, orthorhombic, and rhombohedral respectively. The larger constraint stress induces higher piezoelectric constants in tetragonal PFN thin film. Epitaxial

thin-layers of $Pb(Zr_{0.52}Ti_{0.48})O_3$ (or PZT) grown on (001), (110), and (111) $SrTiO_3$ substrates are tetragonal, monoclinic C, and rhombohedral respectively. Enhanced ferroelectric properties were found in the low symmetry monoclinic phase. A triclinic phase in BFO was observed when it was deposited on tilted (001) STO substrates by selecting low symmetry (or interim) orientations of single crystal substrates.

Then, in two phase composite magnetoelectric thin films, the morphology stability was controlled by epitaxial engineering. Because multiferroic properties are strongly related to the nano-structures of the composite thin films, it is necessary to research the nano-structures in composite thin films. Nano-belt structures were observed in both $BaTiO_3$-$CoFe_2O_4$ and $BiFeO_3$-$CoFe_2O_4$ systems: by changing the orientation of substrates or annealing condition, the nano-pillar structure could be changed into nano-belts structure. By doing so, the anisotropy of ferromagnetic properties changes accordingly. The multi-ferroic properties and magnetoelectric properties or (001), (110) and (111) self-assembled $BiFeO_3$-$CoFe_2O_4$ nano-composite thin film were also measured.

Finally, the regular $CoFe_2O_4$-$BiFeO_3$ nano-array composite was deposited by pulsed laser deposition patterned using a focused ion beam. Top and cross-section views of the composite thin film showed an ordered $CoFe_2O_4$ nano-array embedded in a $BiFeO_3$ matrix. Multiferroic and magnetoelectric properties were measured by piezoresponse force microscopy and magnetic force microscopy. Results show (i) switching of the magnetization in ferromagnetic $CoFe_2O_4$ and of the polarization in ferroelectric $BiFeO_3$ phases under external magnetic and electric field respectively, and (ii) changes of the magnetization of $CoFe_2O_4$ by applying an electric field to the $BiFeO_3$ phase.

Dedicated to my parents, wife and son

ACKNOWLEDGMENTS

I would like to express my sincere gratitude to my advisors, Professor Dwight Viehland and Professor Jiefang Li, for their faith, guidance, and support throughout the course of my doctoral research.

I have tremendous respect for Professor Dwight Viehland for his knowledge, wisdom, and passion for research. I benefited from his guidance in every aspect and step during my doctoral study. The discussions and suggestions he made regarding my research, his patience when correcting my papers, proposals and thesis, and his assistance on my preparation for conference talks, all of which were important in my growth and maturity as a researcher. I deeply appreciate all these invaluable help. He has made me into a confident and perseverant scientist who is ready to start my academic career.

Equally important, Professor Jiefang Li has given me great help in almost all equipment and facilities setup. She has generously shared her knowledge and experience in experimental techniques. Her profound understanding and solid theory in materials science lead me to a high standard in research habits.

In particular, I would also like to thank Professor Shuxiang Dong for all the instruction, discussion, and cooperation in the piezoelectric motor and magnetoelectric devices, which are the applications of the materials I studied.

I would like to give my thanks as well to Professor Yu Wang for the many valuable discussions on nano-twin structure in ferromagnetic thin films and nano-belts structure in multiferroic composite thin films; to Professor Shashank Priya for the valuable discussions about the deposition and characterization of thin films in the project meetings and prelim test; to

Professor David Clark for serving in my committee and taking time out of his busy schedule to evaluate my work.

I especially thank Dr. Junling Wang for leading me into the PLD thin film preparation and useful discussion in ferroelectric thin films. My gratitude also extends to my colleagues including Dr. Feiming Bai, Naigang Wang, Dr. Hu Cao, Dr. Zengping Xing, Dr. Junyi Zhai, Dr. Xin Zhao for their valuable comments and suggestions through discussion in the areas of their expertise.

I want to show my thanks to Dr. Gorden Yee, Dr. Guangbin Wang, John McIntosh, Dr. Mitsuhiro Murayama, Stephen McCartney for training and assistance in the SQUID, FIB, HRTEM and SEM, which are very important in my research. I would also like to thank David Berry for much technical support.

Gratitude also goes to Dr. Jaydip Das, Zhiguang Wang, Yaodong Yang for discussions in project meetings; to my colleagues and friends including Dr. Wenwei Ge, Chris DeVreugd, Jianjun Yao, Liang Luo, Junqi Gao, Menghui Li, it will be always a good memory to work with these guys.

The most important acknowledgement is saved for my family. I would like to express my gratitude to my parents, Chunguang Yan and Guifang Wang, for their constant faith, encouragement, and support during my doctoral study, to my wife, Xiuyuan Zhang, for her continually support in every detail of my life. She is also the author of several papers without her name printed. I thank my son, who gives me the strength to keep going with my work especially when I feel frustrated and tired. I thank my parents-in-law, Zhongxing Zhang and Zhaoxiang Wang, for taking care of my son to let me focus on my dissertation.

TABLE OF CONTENTS

LIST OF TABLES

LIST OF FIGURES

Chapter 1: Introduction

1.1 Magnetoelectric and multiferroic

Magnetoelectric (ME) materials exhibit an induced polarization under external magnetic field, or an induced magnetization under external electric field, as shown in Figure 1.1. The concept of the ME effect was originally proposed by P. Curie in 1894[1]. In 1959[2], Dzyaloshinskii predicted that the ME effect should be observed in single phase Cr_2O_3. The magnetic field induced polarization (i.e. the direct ME effect) of Cr_2O_3 was first observed by Astrov in 1960[3]. Shortly thereafter, the electric field induced magnetization (i.e. the converse ME effect) in Cr_2O_3 was reported by Rado and Folen in 1961[4]. A timeline of the history of magnetoelectricity is summarized in Figure 1.2 [1-6].

Multiferroic (MF) materials exhibit more than one primary ferroic order parameter in a single material. This term MF was first used by Schmid in 1994 [7]. Ferroic materials exhibit hysteresis loop relationships between their induced internal properties and an externally applied field, as shown in Figure 1.3. The types of ferroic materials include ferromagnetics (FM), ferroelectrics (FE) and ferroelastics which have hysteretic relations between magnetization (M) and magnetic field (H), polarization (P) and electric field (E) and strain (ε) and external stress (σ), respectively. Correspondingly, the materials exhibit a spontaneous polarization, magnetization and/or strain; in addition, to switching ferroic rotation of the spontaneous parameter under its conjugate field. Furthermore, materials having anti-ferromagnetic or anti-ferroelectric orders (where there are two sublattice with opposite orientations of the spontaneous parameter) are also known.

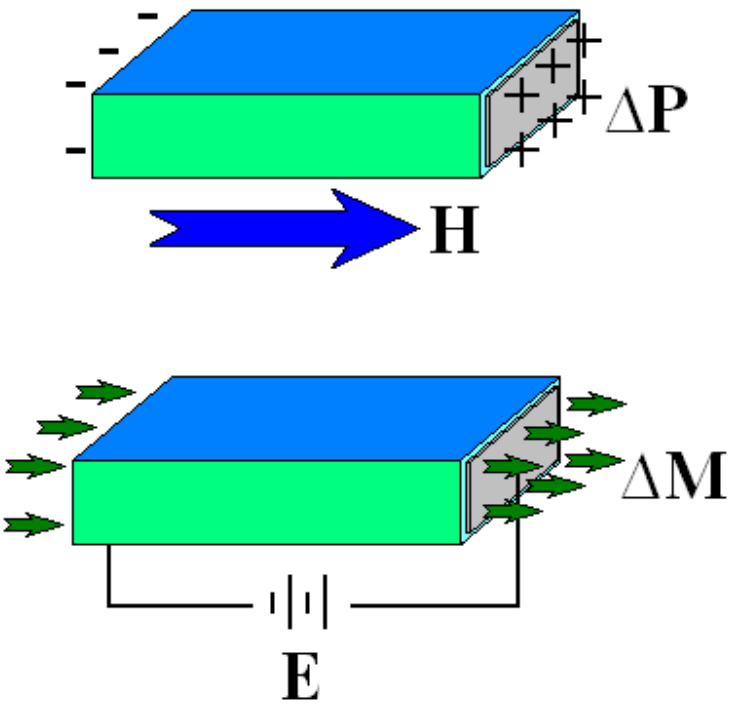

Figure 1.1 Magnetoelectric coupling in magnetoelectric materials, (a) change of polarization is induced by external magnetic field, or (b) change of magnetization is induced by external electric field.

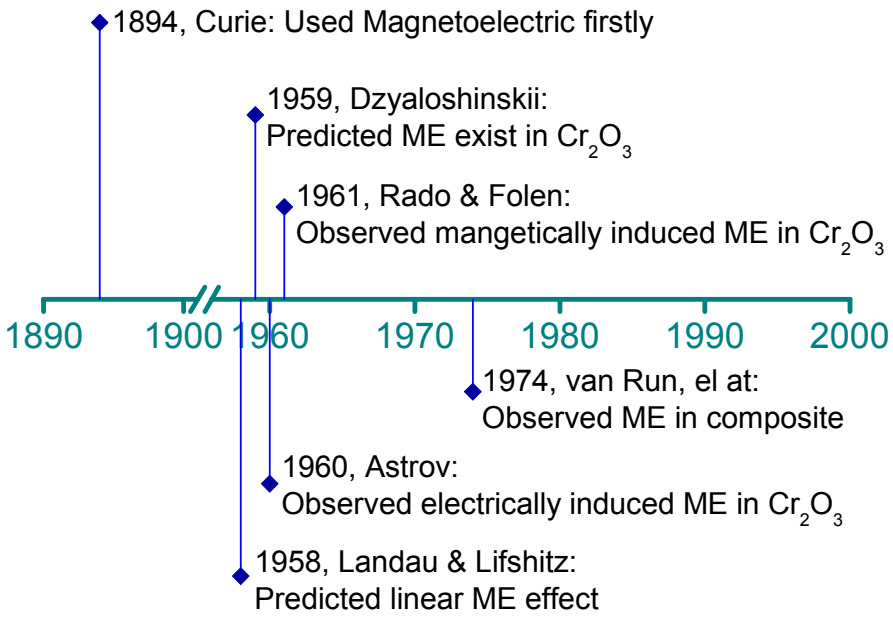

Figure 1.2 Timeline of the development of magnetoelectric materials.

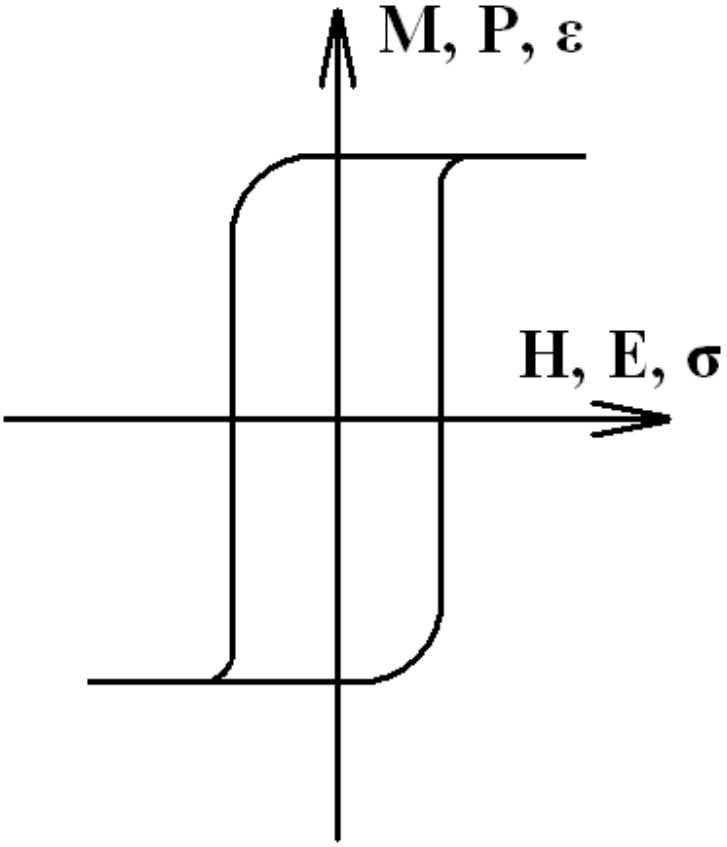

Figure 1.3 Hysteresis loop of M-H, P-E, and ε-σ.

Multiferroics are not limited to single phase materials, but are also known in composites consisting of ferroelectric and ferromagnetic phases. By elastically coupling the strain between the piezoelectricity of the ferroelectric phase and the magnetostriction of the ferromagnetic one, two-phase composites have been designed that have much larger ME coefficients than that of single phase systems.

1.2 Background

Magnetoelectricity was initially reported in single phase Cr_2O_3 crystals and ceramics. Since 1959 [2], many single phase materials have been found to possess ME properties. However, in single phase systems, ME effects have always been found to be weak. Alternatively, it was found that composite multiferroic (FE and FM) systems also have ME properties, which have much larger effects than that of single phases. In particular, layered composite of piezoelectric and magnetostrictive phase have been shown to have giant ME coefficients [8-10].

1.2.1 Single phase ME materials

The first single phase ME material Cr_2O_3, which has a linear ME effect, was first reported in 1960 [3]. Since then, many other single phase ME material families have been found. The ME effect of single phase materials comes from the asymmetry between the magnetic and polar sublattices of the crystal structure. The ME coupling of single phase material is very weak. The ME effect in most single phase ME materials only exists at very low temperatures, below 6K: such as R_2CuO_4 [11] and $Me_3B_7O_{13}X$ [12]; some can only be detected at extremely high magnetic fields of >20 Tesla, such as $BiFeO_3$ [13]; and some can only be detected as a minute change of the dielectric constant at the Neel temperature or correspondingly a small change of

the magnetic permeability at the Curie temperature, such as $RMnO_3$ [14] and $Pb(Fe_{1/2}Nb_{1/2})O_3$ [15]. Frankly speaking, no single phase material has yet been found that has a measurable ME coefficient at room temperature and at low magnetic field. The largest ME coefficient previously reported at either low temperature or high H is on the order of 1mV/cm.Oe. This effect is too small to be of practical use in devices. Prior studies were done primarily for scientific curiosity.

1.2.2 ME composites

Particle composites of ferroelectric and ferromagnetic materials have a product ME tensor effect, mediated via the elastic interactions of both strictive phases, although separately each phase does not have a ME effect. A (0-3) composite is illustrated in Figure 1.4, which was fabricated by the combination of ferroelectric (such as perovskite $BaTiO_3$ or PZT, or PVDF polymer) and ferromagnetic (such as spinel $CoFe_2O_4$ or $NiFe_2O_4$, or Terfonel-D or $Fe_{1-x}Ga_x$ alloys) phase particles [16-19]. The ME coefficient of these particle composites has been reported to be about 10~100mV/cm.Oe, which is much higher than that of single phase ME materials, but yet much lower than that theoretically predicted for composites. One of the difficulties of 0-3 composites is the low resistivity of the ferromagnetic particles, which in effect lowers the resistivity of the entire composite. Accordingly, particle composites have had leakage problems that limit their potential. Consequently, these types of particle composites can not be fully poled, and do not have notable induced polarization changes under applied magnetic fields.

1.2.3 Laminated composites

In order to overcome the difficulties of particle composites of ferroelectric and ferromagnetic phases not achieving their potential as ME materials, laminated multilayer

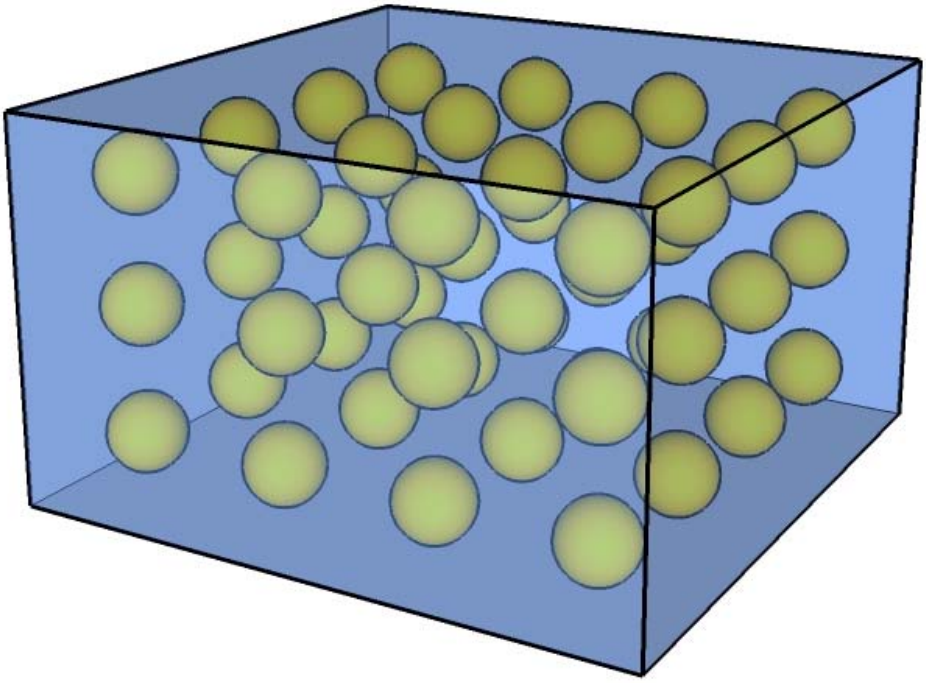

Figure 1.4 An illustration of a (0-3) structure.

composites consisting of piezoelectric and magnetostrictive layers have been developed, as illustrated in Figure 1.5 [10, 20]. Because different layers have different functions (such as piezoelectricity or piezomagnetic), the ferroelectric layers can have higher resistivity and yet be fully polarized. The piezoelectric and magnetostrictive layers are bonded together by co-sintering or by conductive epoxy; both mechanisms provide interfacial layers that are elastically stiff enough to provide sufficient stress transfer between layers. Multilayer structures have much higher ME coefficients on the order of 100~1000mV/cm.Oe, relative to that of 0-3 particle composites. In particular, if we optimize the orientations of the electric and magnetic fields, ME coefficient on the order of >1V/cm.Oe can be achieved for laminated composites, which enable the detection of magnetic field as low as 10^{-11} T. Furthermore, under resonant drive conditions, the ME coefficient is greatly enhanced, reaching values of 20V/cm.Oe [21-22].

1.2.4 Miniaturized ME laminates

The reason I would like to study thin films is that ferroelectric thin layers are known to have enhanced polarization properties [23]. This is due to the stress introduced by the interaction of the elastic constraint of the substrate with the electostriction of the ferroelectric phase. It would be a major achievement to integrate magnetic-polar multi-functionalities into dielectric films. Many new types of magnetoelectric devices would then be conceivable.

Recently, enhanced polarization and magnetization have been reported for epitaxial layers of single phase $BiFeO_3$ deposited by pulsed laser deposition or PLD. For example, the induced polarization of epitaxial layers (60μC/cc) was 10× higher than that of the corresponding bulk (6μC/cc) [24, 25]. Unfortunately, it has been proven difficult to detect a significant ME

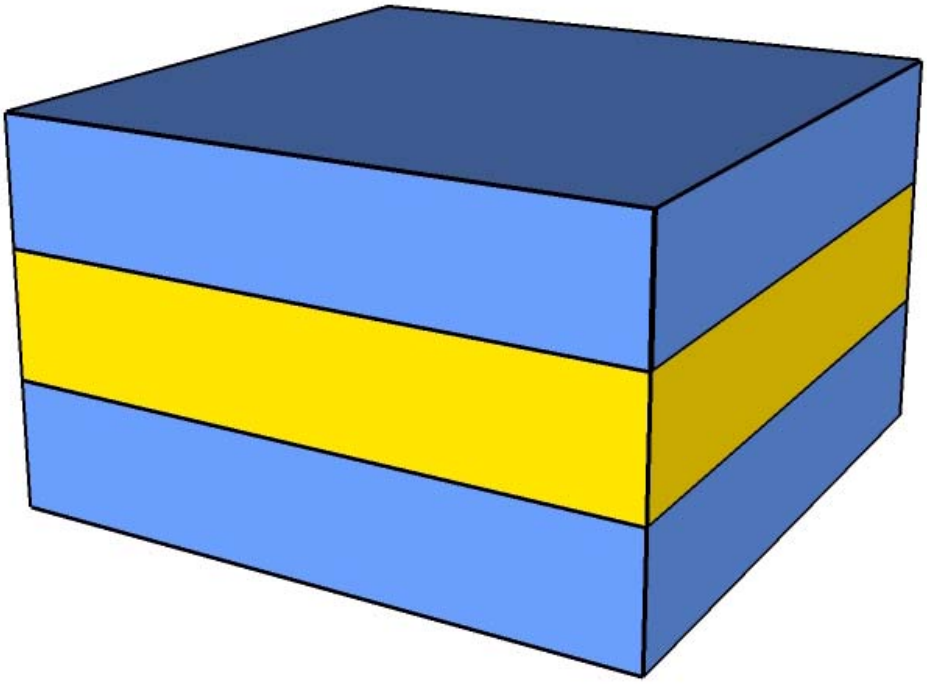

Figure 1.5 An illustration of a laminated multilayer structure.

charge in these layers. I believe that this difficulty is due to the fact that the thin (200nm) $BiFeO_3$ layer can not deform in response to H, as it is rigidly constrained by the $SrTiO_3$ substrate. Furthermore, self-assembled nano-composites of $CoFe_2O_4$-$BaTiO_3$ have been deposited on $SrTiO_3$ (see Figure 1.6) [26]. The ferroelectric and ferromagnetic responses of these nano-composites are nearly the same as those of their corresponding bulk crystals. A small change in the magnetization at the Curie temperature has been detected, which indicates that there is coupling between ferroelectric and ferromagnetic order parameters in the interphase interfacial regions. Although only an indirect coupling was observed in this self-assembled nano-composite, it exhibited better ME coupling compared to other epitaxial thin films. This finding opens the possibility that ME coefficients might be measured in multiferroic composite thin films.

1.3 Definition of the objectives of this thesis:

This thesis will focus on multi-ferroic thin films, in particular ones that are both ferroelectric/anti-ferroelectric (FE/AFE) and ferromagnetic/anti-ferromagnetic (FM/AFM). There are several reasons why these thin films have been important topics of research in the last few years. First, these thin films are multi-functional, offering both electrical and magnetic functions in devices. Second, when FE/AFM properties couple to FM/AFM ones, a new property called magnetoelectricity results. Composite multi-ferroic materials have also been prepared and characterized in prior investigations. In this case, neither phase needs to be magnetoelectric; rather, magnetoelectricity is a product tensor property. The individual phases of the composite are piezoelectric perovskites and magnetostrictive ferrites or alloys. These two types of phases are coupled to each other through their strictions. Thus, a magnetic field applied to the

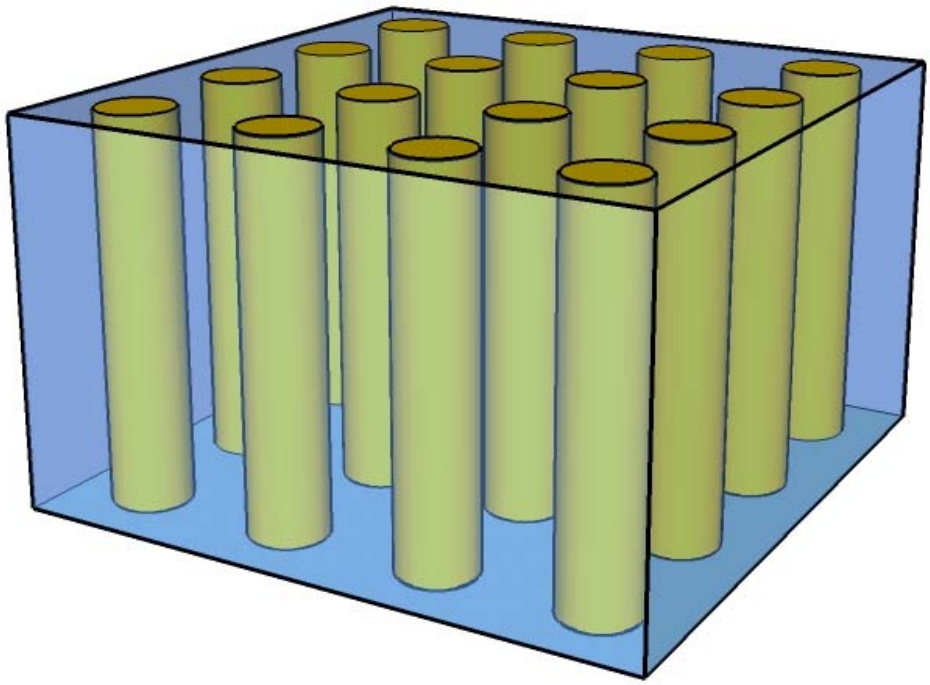

Figure 1.6 An illustration of $CoFe_2O_4$ nano-pillars embedded in a $BaTiO_3$ matrix.

magnetostrictive phase generates a strain that induces a corresponding strain in the piezoelectric one to which it is bonded; in turn, this then results in an induced voltage across the piezoelectric phase [18].

Magnetoelectric composites have been studied in both bulk laminate and thin film forms. Thin film composites in particular interest to my thesis are self-assembling nano-composites epitaxially grown on $SrTiO_3$ substrates. This approach offers the opportunity to miniaturize multi-ferroic two phase composites. Thin films of magnetoeletric (ME) or electromagnetic (EM) materials have many potential applications in devices such as sensors, electrical field assisted magnetic memories, energy transformers, field tunable microwave devices and non-reciprocal couples.

My thesis topic will include studies of single phase and multiphase multi-ferroic thin films. After the first single phase multi-ferroic material Cr_2O_3 was reported in 1960 [3], many other single phase multi-ferroic materials were discovered: such as R_2CuO_4 (R=Pr, Nd, Sm, Eu and Gd) [27], $Me_3B_7O_{13}X$ (Me=Fe, Co and Ni; and X=Cl, Br and I) [12], $RMnO_3$ (R= Ho, Er, Tm, Yb, Lu and Y for hexagonal phase; and R= La, Ce, Pr, Nd, Sm, Eu, Gd, Tb, and Dy for orthorhombic phase) [14, 28-29], etc. With regards to all these families of materials, perovskites containing Fe, Co, Ni, Cr, or Mn ions are the best candidate systems because of their higher polarization and antiferromagnetic sublattice exchange. Multi-ferroic perovskite materials include $BiFeO_3$, $LaFeO_3$, $Pb(Fe_{2/3}W_{1/3})O_3$, $Pb(Co_{2/3}W_{1/3})O_3$, $Pb(Mn_{2/3}W_{1/3})O_3$, $Pb(Fe_{1/2}Ta_{1/2})O_3$. Of these, $BiFeO_3$, and $Pb(Fe_{1/2}Nb_{1/2})O_3$ are two excellent choices because of their higher Curie and Néel temperatures, which are far in excess of room temperature. There have been numerous recent investigations of $BiFeO_3$ and in particular epitaxial thin films [24]. However there have not been any reports of epitaxial $Pb(Fe_{1/2}Nb_{1/2})O_3$ thin films. The first important aspect of my

thesis will be the study of $Pb(Fe_{1/2}Nb_{1/2})O_3$ single phase multi-ferroic materials, which have both ferroelectric and antiferromagnetic sublattice exchange. Another important aspect of PFN is that it is a relaxor ferroelectric material; consequently, it will have some special properties that $BiFeO_3$ does not possess, such as slim P-E loops and a frequency dependence dielectric response. These additional properties, induced by cation disorder, make PFN an interesting alternative choice to $BiFeO_3$ as a single phase ME thin film.

To better understand the structure and properties of two phase epitaxial films, it is first necessary to investigate single phase piezoelectric materials, because they are the basic components of multi-ferroic composite thin films. Accordingly, a second important aspect of my thesis is the deposition and characterization of single phase FE thin films that will subsequently be used in self-assembly of nano-composites. The structure of epitaxial ferroelectric layers may be strongly dependent on elastic constraint and thus might be slightly distorted from each other. Such variability of structure by two-dimensional epitaxial constraint would have important ramifications on the tensor properties of individual phases (piezoelectric or magnetostriction) once integrated together as heterostructures on a substrate. I have chosen piezoelectric $Pb(Zr,Ti)O_3$ (PZT) for which to investigate these important aspects. Ferroelectric PZT is interesting to study for this purpose because (1) it has nearly the highest value of polarization; and (2) monoclinicly distorted phases for bulk materials are known in its MPB region that have superior ferroelectric properties, but have not yet been investigated for thin films.

Finally, the last goal of my thesis will concern two phase multi-ferroic composite thin films. I will use self-assembly methods to build nano-structured composite thin films of different geometries. There are several questions that I will focus on including: (1) what types of new nano structures can be built; (2) what is the self-assemble mechanism of the nano-structure; (3)

how do FE and FM phases of different nano-structures couple to each other; and (4) how does this coupling depend on the structural integrity of the elastic exchange across the interphase interfaces. I have chosen $BiFeO_3$-$CoFe_2O_4$ as the two phase multi-ferroic thin films for study in my thesis, because (i) $BiFeO_3$ and $CoFe_2O_4$ are excellent FE and FM materials with high spontaneous polarizations and magnetizations respectively; (ii) the perovskite and spinel structures are similar to each other, where the lattice constant of CFO matches that of BFO, nearly 2x of that of BFO; and (iii) they share the same B-site ions, making diffusion easier during the self-assembly process.

Specifically, the goals of this thesis are to:

- Study the structural, relaxor ferroelectric and stress induced ferromagnetic properties of single phase epitaxial PFN thin films for various crystallographic orientations;
- Study monoclinic M phase structures and related ferroelectric properties of single phase PZT perovskite thin films;
- Study nano-belt formation and growth mechanisms in BFO-CFO composite multi-ferroic thin films.
- Directly measure the magnetoelectric properties of nano-composite thin films.

1.4 Materials studied in this thesis

1.4.1 Single phase multi-ferroic thin film - ferroelectric and ferromagnetic $Pb(Fe_{1/2}Nb_{1/2})O_3$:

Lead iron niobate, $Pb(Fe_{1/2}Nb_{1/2})O_3$ (PFN), was discovered by Smolenskii *et al.* in the 1950s [30]. The room temperature lattice structure of PFN single crystals is rhombohedral, with lattice parameters of a_r=4.0123Å (or 4.058Å) and α_r=89.89º [15, 30-32]. It is a multi-ferroic

material transforming from a paraelectric (cubic) phase to a ferroelectric (rhombohedral) one at a Curie temperature of 385K [30, 33]; and concurrently, from a paramagnetic state to antiferromagnetic (AFM) spin-ordered one at a Néel temperature of 143K [31], and subsequently undergoing a secondary AFM→AFM transition at 19K [34-35]. It is believed that the PM→AFM transition near 143K is related the 180° Fe-O-Fe antiferromagnetic superexchange interaction; whereas the AFM→AFM transition is related to 180° Fe-O-Nb-O-Fe superlattice exchange interaction [35]. The induced magnetization of PFN single crystals at 80K has been reported to be <100emu/cc under a magnetic field of $H=10^5$Oe [15]. PFN is a mixed B-site cation perovskite and accordingly could be anticipated to have relaxor ferroelectric characteristics similar to $Pb(Zn_{1/3}Nb_{2/3})O_3$ or PZN, such as slim-loop polarization (P-E) characteristics [36] and a polarization dynamics that scale to a Vogel-Fulcher or stretched exponential relations [37].

The dielectric and ferroelectric properties of PFN bulk single crystals and ceramics have been reported. The maximum polarization is only ~10μC/cm^2 [38]; the P-E response is 'non-square' yet hysteretic. These limited dielectric and ferroelectric properties of bulk crystals and ceramics are believed to reflect inferior dielectric insulation. Non-epitaxial thin-layers of PFN have been previously prepared by sol-gel [39-40] and pulsed-laser deposition (PLD) [41-42]. Superior ferroelectric properties were reported in both cases, relative to bulk crystals and ceramics. Sediar et al. [39] found the maximum polarization to be P_m=24μC/cm^2 for sol-gel films, and Gao et al [41] reported a value of P_m=22μC/cm^2 for PLD films deposited on $La_{0.7}Sr_{0.3}MnO_3$/(001)Si. However, epitaxial PFN films have yet to be prepared and studied.

1.4.2 Single phase ferroelectric thin film – $Pb(Zr_{0.52}Ti_{0.48})O_3$:

Lead zirconate titanate, $Pb(Zr_{1-x}Ti_x)O_3$ or PZT, is a ferroelectric perovskite widely used as piezoelectric actuators and sensors due to their superior piezoelectric coefficients. The phase diagram of $Pb(Zr_{1-x}Ti_x)O_3$ can be found in Jaffe et al. (Figure 1.7)[43]. Outstanding piezoelectric properties occur in the vicinity of a morphtropic phase boundary (MPB) between tetragonal (T) and rhombohedral (R) ferroelectric phases near $x \approx 0.50$ at room temperature. Conventionally, these excellent properties were attributed to the co-existence of T and R ferroelectric phases.

The PZT phase diagram of [43] was widely accepted until 1999, when Noheda et al.[44-46] reported a monoclinic phase in $Pb(Zr_{0.52}Ti_{0.48})O_3$ ceramics using high-energy x-ray diffraction. A phase transformational sequence of cubic (C) → tetragonal (T) ferroelectric → monoclinic (M) ferroelectric was found. At the T→M transition, the lattice constant c remains essentially unchanged, while that of a_T splits into a_m and b_m with a monoclinic angle of $\beta - 90° \approx 0.5°$. Mesh scans then revealed signatures of the monoclinic C (M_c) phase belonging to the space group *Pm*. The M_c unit cell is primitive having a unique b_m axis that is oriented along the pseudocubic [010], where the polarization is constrained to the (010) plane. Subsequently, the excellent piezoelectric properties of MPB ferroelectric crystals and ceramics have been attributed to M phases [47-50], where the polarization is allowed to rotate in the monoclinic plane.

Pertsev et al. [51] calculated the epitaxial phase diagram for PZT thin-layers using thermodynamics: as functions of x, temperature, and misfit strain. They predicted an M ferroelectric phase in MPB compositions of PZT films, which should also have superior dielectric and piezoelectric coefficients. It is noteworthy that thin-films of other perovskite ferroelectrics, such as

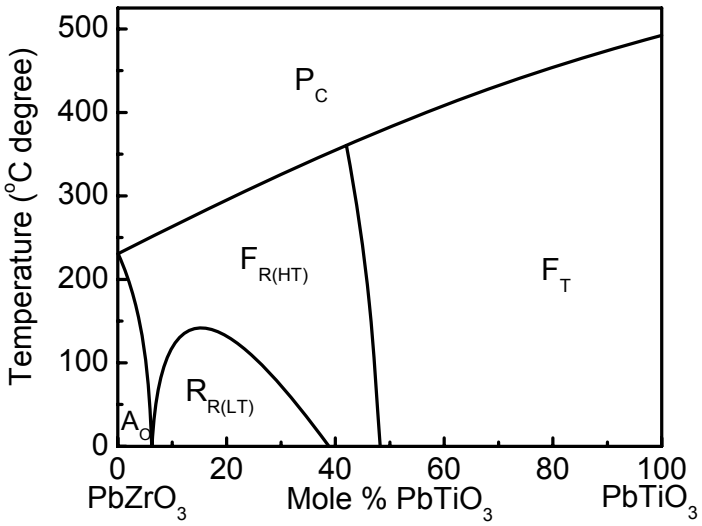

Figure 1.7 A simple illustration of $Pb(Zr_{1-x}Ti_x)O_3$ phase diagram.

$BiFeO_3$, have been shown to have monoclinic phases that also have excellent ferroelectric properties [24, 52-53]. However, experimentally, a monoclinic phase in PZT thin films has never been found.

1.4.3 Single phase ferroelectric thin film – $BiFeO_3$:

The perovskite $BiFeO_3$ (BFO) is a multiferroic material which has both ferroelectric and ferromagnetic orders [54-56]. Its Curie temperature is 830°C and its Neel temperature is 370°C [57-61]. At room temperature, bulk BFO single crystals have a distorted rhombohedral (R) structure with lattice parameters of (a_r, α_r)=(3.96Å, 89.4°). Along the [111], BFO has a 3-fold axis, where the Bi^{3+} and Fe^{3+} cations are displaced from their symmetric positions [54, 62-65]. This asymmetry generates a spontaneous polarization along the [111]. In addition, there is an alignment of spins along [111], whose moments are slightly canted from this direction resulting in a weak ferromagnetic moment.

Epitaxial BFO thin layers have also been reported [24]. The symmetry of the BFO layers has been shown to be notably distorted from that of the R phase in bulk crystals [66]. Investigations by high resolution X-ray diffraction (XRD) [67-68] have shown that films grown on (001), (110), and (111) SrTiO3 (STO) substrates respectively have a monoclinic A (MA) structure with lattice parameters of ($aM/\sqrt{2}$, $bM/\sqrt{2}$, cM, β)=(3.973Å, 3.907Å, 3.997Å, 89.2°), where the polarization is constrained to the (001) plane; monoclinic B with lattice parameter of ($a_M/\sqrt{2}$, c_M, β)=(3.985Å, 3.888Å, 89.35°), where P is constrained to the (110) plane; and rhombohedral (R) with lattice parameters equivalent to that of bulk crystals, where the polarization is constrained to the (111) direction.

Monoclinic domain engineered phases have previously been reported in perovskite (1-x)$Pb(Mg_{1/3}Nb_{2/3})O_3$-x$PbTiO_3$ (PMN-PT) and (1-x)$Pb(Zn_{1/3}Nb_{2/3})$-x$PbTiO_3$ (PZN-PT) single

crystals [48-50, 69-76]. Domain engineering was achieved by cooling under electric fields applied to high symmetry (i.e., (001), (110), or (111)) directions, or orientations different from that of the spontaneous polarization P_s in the zero-field-cooled state [50, 76]. Low symmetry structurally bridging monoclinic phases have been shown to be important in enhancing properties in the vicinity of a morphtropic phase boundary (MPB).

Analogously, in perovskite thin layers, low symmetry structurally bridging phases can be epitaxially engineered by lattice parameter mismatch and substrate orientation [66]. Theoretical investigations have shown that epitaxy can be used as a thermodynamic variable by which to control phase stability in perovskites. Lattice parameters of films can be altered in perovskites in order to relax epitaxial stress [77]. Although the magnitude of the constraint stress can be changed by various methods (such as substrates, buffer layers, or film thickness), a more important factor in the engineering of phase stability is the direction along which this constraint stress is applied. Prior investigations have been limited to the study of higher symmetry (001), (110) and (111) oriented substrates. The influences of lower symmetry oriented substrates have not yet been investigated on the phase stability of perovskite layers.

1.4.4 Multi phase multi-ferric thin film – $BaTiO_3$-$CoFe_2O_4$ / $BiFeO_3$-$CoFe_2O_4$:

Self-assembling nano-structures in multi-ferroic two phase epitaxial thin films of spinel and perovskite have recently been the topic of a number of investigations [26, 78-96]. In these thin films, not only can the compositions (one ferroelectric and one ferromagnetic) be chosen, but also the morphological features of how these two phases are assembled with respect to each other on the nanometer scale can be designed. Recent investigations have reported (1-3) and (3-1) nano-pillars in a second phase matrix [26, 78-85], (0-3) nano-particles dispersed in a matrix [86-

90], and (2-2) multi-layer two phase composite thin films [91-92]. Following both experimental observations [26, 93-95] and theoretical calculations [96], the (1-3) nano-pillar structure is a promising means by which to enhance magnetoelectric exchange between ferroelectric and ferromagnetic phases in composite thin films.

In 2004, Zheng et al. [26] successfully deposited epitaxial two phase films that self-assembled into nano-pillars of $CoFe_2O_4$ (CFO) in a $BaTiO_3$ (BTO). Since then, there have been a number of investigations to understand the mechanism of the nanostructure's self-assembly. Zheng et al. [78] reported that the difference between the surface energies of the perovskite and spinel phases is an important factor in determining which assembles as nano-pillars and which as matrix. For (001) epitaxial layers, they found that the surface energy of the perovskite phase was much larger than that of the spinel, and that the perovskite preferentially wet the substrate rather than spinel. Consequentially, perovskite becomes the matrix phase, whereas spinel becomes nano-pillars embedded in the perovskite. However, for (111) epitaxial layers, the relative values of the surface energies of these two phases are opposite to that of the (100), and accordingly self-assembly results in perovskite nano-pillars embedded in a spinel matrix.

Subsequently, Zheng [79] used a Winterbottom construction to explain the morphology of the nano-structure in $BiFeO_3$-$CoFe_2O_4$ (BFO-CFO) epitaxial thin films. The morphology of the nano-structure perpendicular to the substrate was shown to be Wulff shape cuts: spinel an octahedron bounded by eight {111} facets, perovskite a cube with six {100} facets. By using this method, the presence of spinel pyramids on (100) oriented substrates and perovskite three-edged cone grown on (111) oriented $SrTiO_3$ substrates could be explained. Untill now, perovskite nano-pillars embedded in spinel matrix, or spinel nano-pillars embed in perovskite have both reported; however, other types of nanostructures, such as nano-belts have not been reportedly.

Chapter 2: Instrumentations Used in Work

2.1 Pulsed laser deposition

Pulsed Laser Deposition (PLD) is a kind of physical vapor deposition method which has been widely used in the research of oxide thin film preparation. For these reasons, PLD was chosen as the method by which oxide thin films were deposited in this thesis. The basic set up of a PLD system includes a high energy laser, a deposition chamber and several lenses connected between them. The laser used in our deposition system was a Lambda 305. The gas used to excite the laser was KrF and the wavelength of the laser was 248nm. The pulse width of the laser was around 30ns. The energy and frequency of the laser could be adjusted between 300mJ~600mJ and 1Hz~50Hz, respectively.

The structure of the vacuum chamber of our PLD system is shown in Figure 2.1. The left side was the target carousel. The target rotated during deposition. The right side was the heater, in which the single crystal substrate was stuck on by silver paste. The substrate could be heated to 750°C during deposition. Because thermal couple is sealed internally in the heater, the readout temperature was not the true temperature of the substrate. Before deposition, the chamber was pumped down to a pressure of 10^{-5}Torr by a mechanical pump and a turbo pump. During deposition, the chamber was filled with oxygen, and the pressure was controlled to be between 20mTorr~200mTorr by oxygen input and a vacuum gate valve. A laser beam with a diameter of 1cm was focused to a spot of 1mm on top of the target. When the laser hit the target, a plasma was generated on the top and tended to go in a normal direction towards the target. Subsequently, a thin film was deposited on the substrate from the plume.

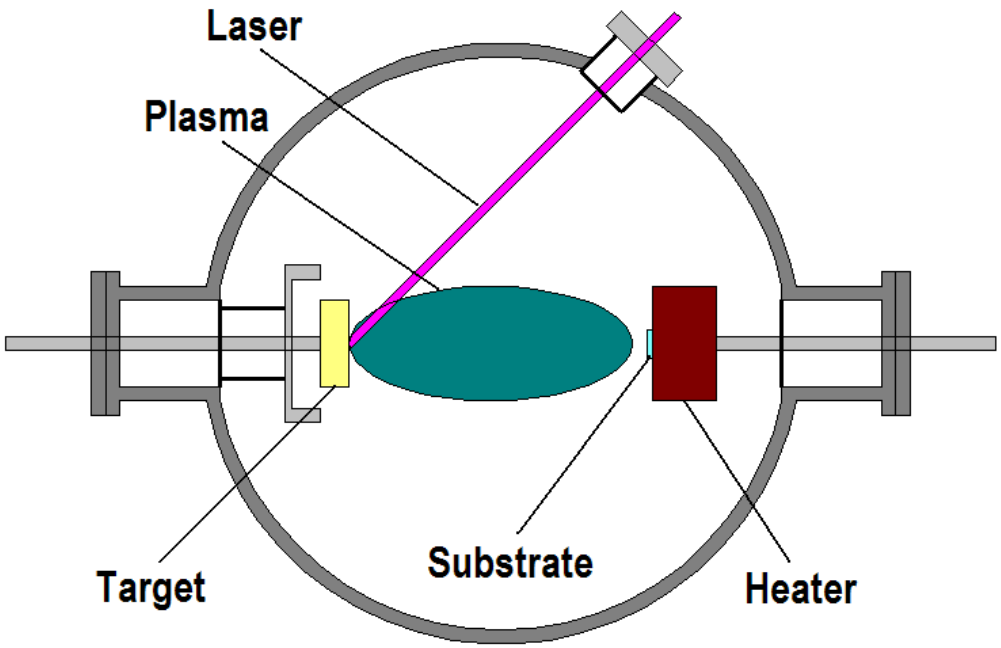

Figure 2.1 Schematic illustration of a pulsed laser deposition system.

The advantage of PLD is that the energy density of the laser on the surface of the target is high: between 1 and 5J/cm^2. All elements in the target are evaporated simultaneously, and subsequently deposited on top of the substrate. Accordingly, PLD is capable of maintain the stoichiometry of the thin film to that of the target, which also keeps the composition of the target unchanged after deposition. PLD is often used to epitaxial grow thin films on top of a single crystal substrate, when the lattice mismatch between film and substrate is lower than 7%. The thickness of the thin film can vary from several nm to several μm, depending on deposition time and other varieties.

The drawback of PLD is that the plasma tends to go in a direction normal to the target. Consequently, the film thickness is often not uniform for large area layers. However, when the size of the substrate is smaller than 5mm, such non-uniformities are usually small and can be neglected.

2.2 X-ray diffractometer

X-ray diffraction (XRD) is a technique often used to study the crystal structure and lattice parameters of materials. The XRD system used in this thesis was a Philips X'pert high-resolution system equipped with a two-bounce hybrid monochromator and an open three-circle Eulerian cradle. The analyzer was a Ge (220) cut crystal with a 2θ-resolution of 0.0068°. The x-ray unit was operated at 45kV and 40mA with a wavelength of 1.5406Å (CuKα).

During measurement in our system, the sample can be tilted (Ψ) by ±90° or rotated (Φ) by 360° to find the corresponding crystal faces. Usually the angle of the sample (ω) and the angle of the detector (2θ) have the relationship of 2×(ω+offset)=2θ, as shown in Figure 2.2. The lattice parameters of the sample can then be calculated as follows:

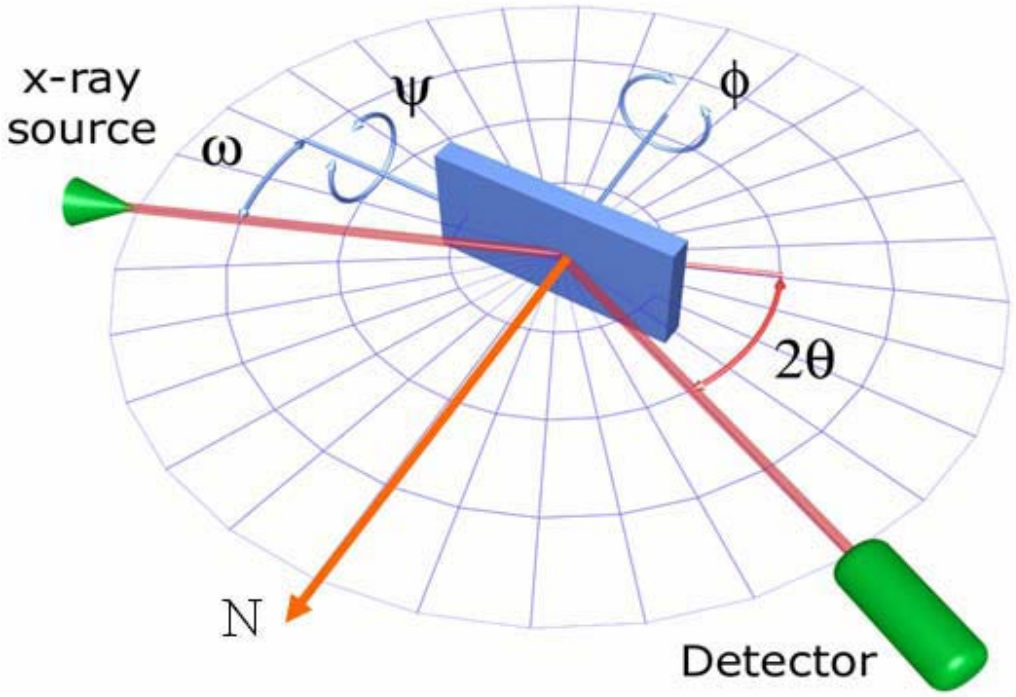

Figure 2.2 Schematics illustration of Philips MPD high resolution x-ray diffractometer.

$$n\lambda = 2dsin\theta \quad (2.1)$$

where n is an integer, λ is the wavelength of the x-rays, d is the lattice spacing, and θ is the diffraction angle.

Line scans were obtained by scanning 2θ-ω with fixed values of Ψ and Φ. By performing line scans, it is possible to determine the epitaxial structure of thin films. Also, line scans can be used to calculate the lattice parameter of the thin film following (2.1). Mesh scans are area scans covering a region of reciprocal space defined by 2θ-ω vs ω. Again such information can be used to determine the crystal structure and/or epitaxy of thin films. From the line or mesh scans, it is also possible to analyze the stress of a thin film and determine distortions of crystal structures.

2.3 AFM, PFM and MFM

Atomic force microscopy (AFM) is an important tool with which to study the top surface of thin films with nano-scale resolution. By changing the tip and scanning mode, various forces can be imaged, such as piezoresponse force microscopy (PFM) and magnetic force microscopy (MFM) which can be used to image ferroelectric and ferromagnetic domains respectively.

The basic structure of our AFM head is shown in Figure 2.3. A cantilever with a sharp tip at the end is used to detect the top surface of the sample. The cantilever is mounted at the end of a piezo-ceramic tube. The position of the tip (x, y) is controlled by this piezo-tube. The piezo-tube has two sets of electrodes which are normal to each other. When electric fields are applied to the two groups of electrodes in the piezo-tube, the end of the tube is able to bend in the x or y direction respectively. After careful calibration, the position of the tip (x, y) is able to be read by the voltage applied to the piezo-tube. During the scan, the tip zigzags on top of the sample surface and the position is recorded in a data file.

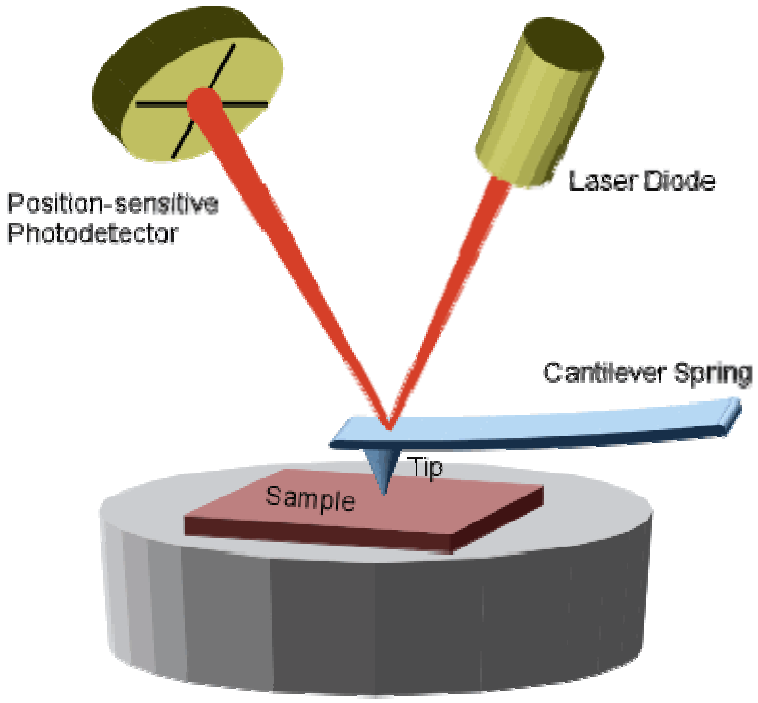

Figure 2.3 Schematics illustration of atomic force microscopy.

A laser beam was reflected by the back side of the cantilever to a position sensitive photo-detector. When the laser dot is in the middle of the photo-detector, the voltage output of the photo-detector is 0V; when the laser dot is on the top of the upper portion of the photo-detector, the voltage output of the photo-detector is positive (+) or negative (-). When the tip is moved on a smooth surface, the reflected laser dot is at the center of the photo-detector; if the tip is on a small bump or pit, the end of the cantilever will bend up or down, consequently reflecting the laser spot up or down in the photo-detector. After calibration, it is possible to measure the height (z) of the defection by a voltage output from the photo-detector. By combining the position (x, y) and the height (z) of the tip, a map of the top surface of the sample can be obtained.

In addition to height, phase information from the sample is important. The tip is driven at the resonance frequency. If the surface of the sample is uniform and flat, the vibration of the tip is constant and stable. If the tip encounters an uphill gradient or an elastically stiffer region, the vibration period of the tip is decreased. If the tip encounters a downhill slope or a softer material, the vibration period of the tip is increased. The shift of the vibration period is given by phase. Because phase signals are sometimes stronger than height signals, phase maps of the top surface of a sample can provide important information.

There are three basic scanning modes for AFM: contact, tapping, and lift. In the contact mode, the tip is always in touch with the surface of the sample. In this mode, tips wear out quickly, and the surface of the sample may also possibly become scratched. However, by always touching the sample surface, the tip can measure the friction between itself and the sample. Also, the tip in this mode can apply an electric field to the sample, which can be used in the PFM measurement. In the tapping mode, the tip is tapped on the sample surface at the resonance

frequency. In this mode, the tip wears out more slowly and the risk of scratching the sample is reduced. This is the most widely used mode for the study of sample topography. In the lift mode, the tip is lifted about 10 to 100nm off the surface and never touches the sample. In this mode, the tips do not wear out; however, the resolution of the map is decreased due to the increase of the lift height of the tips. By using the lift mode, a magnetic cantilever can detect a magnetic signal; accordingly, MFM measurements are based on this mode.

A basic PFM measurement setup is shown in Figure 2.4. The PFM measurement works in the piezo-response mode, which is based on contact. The bottom electrode of the sample is connected to the chuck, and the conductive tip contacts the top surface of the sample. When an AC or DC electric field is applied to the tip (top) or sample (bottom), the piezo materials generate a strain. The tip responds to both height and piezo-response signals, induced by applied AC electric field. However, these two signals are at different frequencies, and the frequency of the piezo-response signal is much lower than that of the height signal. By using two internal lock-in amplifiers, which work at two different frequencies, the height and piezo-response signals can be measured separately. Also, by applying a DC electric field to the tip of sample, the polarization direction of the piezo material can be rotated.

The MFM measurement method is shown in Figure 2.5. It works in an interleave mode, which means the tip scans the surface using a tapping mode first, and then the tip scans the same surface using a lift mode. In the tapping mode, the topography of the sample is recorded. In the lift mode, the topography information is subtracted from the data. Only the response of the magnetic tip to the magnetic signal is recorded in the lift mode. If the magnetic tip is on top of a magnetic material, the vibration frequency of the tip will be changed due to the magnetic

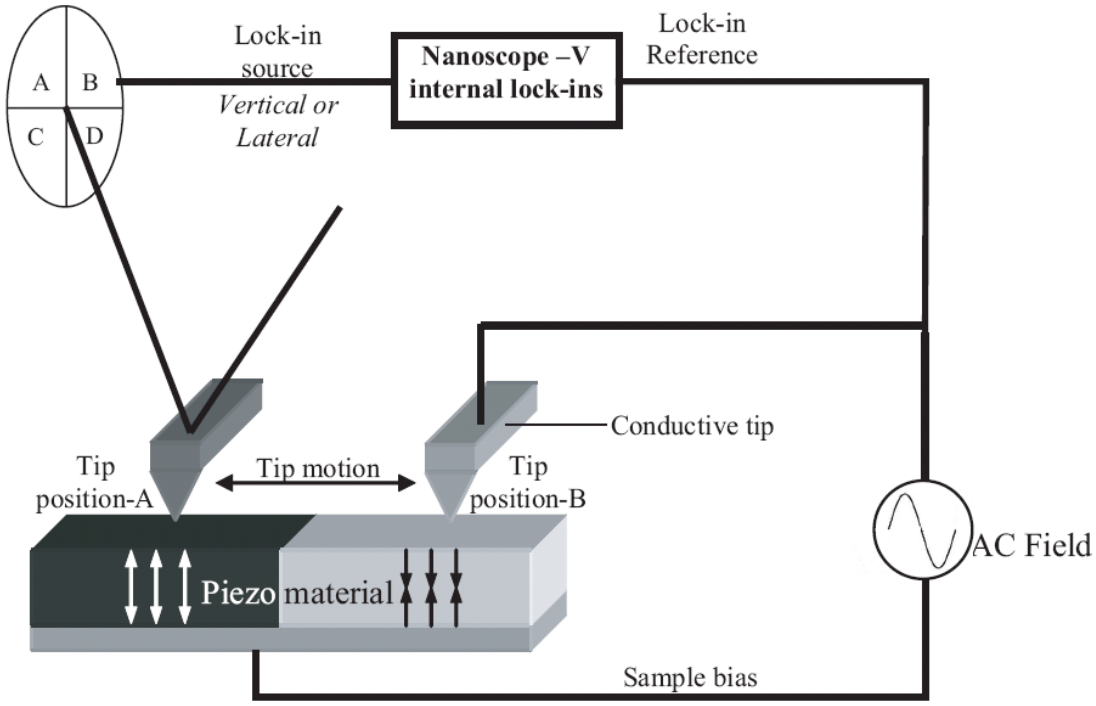

Figure 2.4 Schematic illustration of the piezoresponse force microscopy setup.

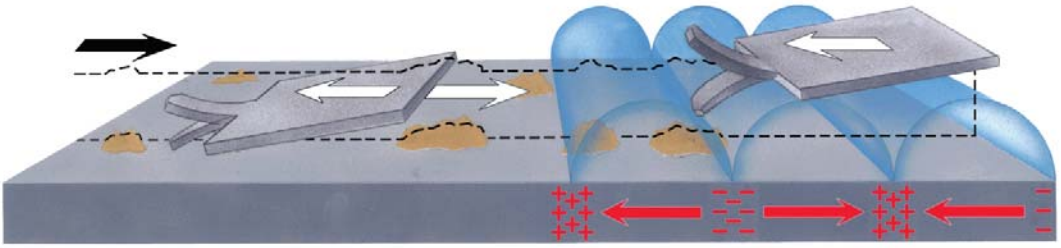

Figure 2.5 Schematic illustration of magnetic force microscopy.

force between the tip and sample. Accordingly, the phase changes of the tip in the lift mode reflect the magnetic signal of the materials. The phase map of the lift mode in interleave is used as the MFM results.

2.4 Electric and magnetic properties measurements

The dielectric constant of the thin films was measured by a HP 4284A precision LCR meter over the frequency range of 20Hz to 1MHz. During measurement, an accurate impedance measurement of the samples under AC electrical signals can be obtained. The impedance is represented as Z, which is composed of real (resistance, or R) and imaginary (reactance, or X) parts, as expressed in the following equation:

$$Z = R + jX \ . \tag{2.2}$$

Most of the thin films studied in this thesis are capacitor materials. Their reactance can be expressed as $X = -j\frac{1}{\omega C}$, where C is the capacitance, ω the angular frequency, and $\omega = 2\pi f$. The impedance of an ideal resistor is $Z_R = R$, and that of an ideal capacitor is $Z_C = \frac{1}{j\omega C}$. The impedance of a capacitor with a resistor is$|Z| = \sqrt{R^2 + X^2}$.

The dielectric constant and loss tangent of the thin film can be calculated from the impedance of the thin film as follows:

$$\varepsilon = \frac{C \cdot d}{\varepsilon_0 \cdot A}, \tag{2.3}$$

$$\tan\theta = \frac{X}{R}; \tag{2.4}$$

where d is the distance between the electrodes, a is the area of overlap of the electrodes, and ε_0 is vacuum permittivity.

The system used to measure the polarization of the film is shown in Figure 2.6. AC voltage supplied by a signal source and an amplifier was applied both to the thin films and to a reference capacitor. The capacitance of the reference capacitor was about 100x larger than that of the thin films. Then, the voltage signal on thin films V_{film} was measured in channel 1 in oscilloscope, where $Z_{ref} << Z_{film}$. Based on the facts that $Q_{film}=Q_{ref}$ and $Q=C \cdot V$, we can conclude that $Q_{film}=C_{ref} \cdot V_{ref}$, where V_{ref} is the signal measured in channel 2 in oscilloscope. For ferroelectric thin films, the relationship between Q_{film} and V_{film} is hysteresis.

A superconducting Quantum Interference Device (SQUID) magnetometer was used to measure the magnetic properties of the thin films. SQUID is a very sensitive probe to magnetic flux, with a resolution at about 10^{-15} Tesla. It uses superconducting loops containing Josephson junctions to detect the magnetization of the sample. SQUID is able to generate magnetic fields between -7 Tesla and 7 Tesla while measuring between 4K and room temperature. Generally, the relationship between the magnetization and the external magnetic field is as follows:

$$M = \chi \cdot H \tag{2.5}$$

where χ is the magnetic susceptibility. Please note that for ferromagnetic materials, the M-H response is also hysteretic.

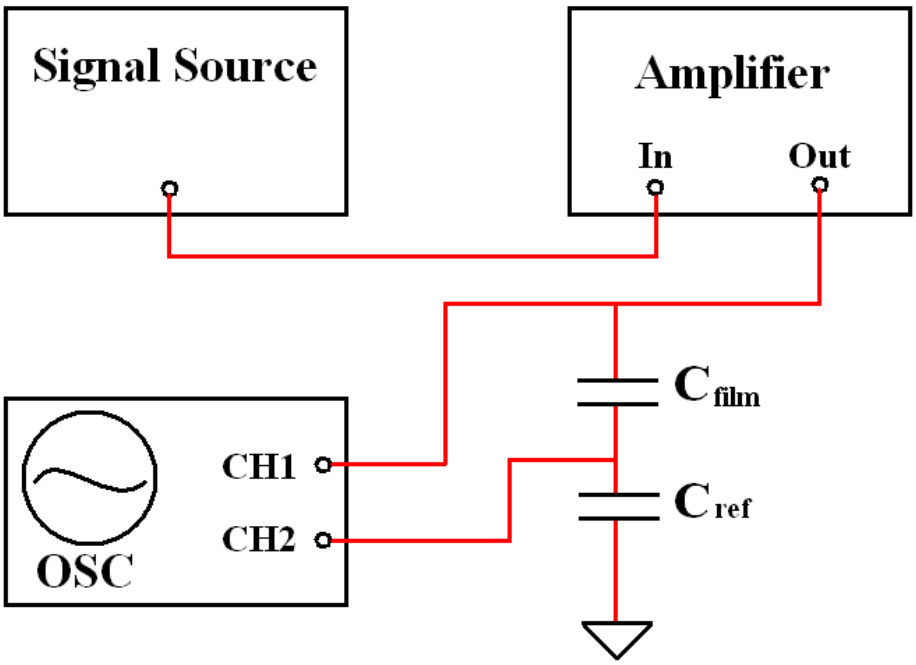

Figure 2.6 Schematic illustration of polarization measurement.

2.5 Focused ion beam

Focused ion beam, or FIB, was used to build nano-structures in composite thin films. The working principle of FIB is similar to scanning electron microscope (or SEM). In SEM, a beam of electrons is focused on the sample by electrostatic lenses to obtain an image of the sample. Whereas, in FIB, a beam of ions is focus on the sample by electrostatic lenses to sculpture the sample. The most widely used ions are gallium (or Ga). Sometimes gold (or Au) and iridium (or Ir) are chosen as the ions. The ions are accelerated at 5~50keV before hitting the sample. The higher the energy, the quicker the sculpturing or cutting speed of the sample; the lower the energy, the finer the pattern that can be cut on the sample.

Because ions are much larger and heavier than electrons, the destruction by electrons of the sample surface in SEM is negligible; however, ions in FIB are used to cut the sample. FIB can cut the sample in any pattern designed by user. The depth of the cutting can be controlled by the working time. However, during cutting, ions impacting the materials destroy the crystallinity on the surface regions of high energy impact, resulting in amorphous regions of around 20nm~30nm in depth.

Chapter 3: Single phase epitaxial thin films – Epitaxial engineering of phase stability

A comparison of the polarization for BTO-CFO [26] nano-composites with that of single phase BTO is shown in Figure 3.1. It can be seen that the polarization of the ferroelectric phase is similar to that of the pure perovskite: the smaller the coercive field for the pure ferroelectric material, the smaller it is in the nano-composite; also, the higher the saturation polarization in the pure FE phase, the higher it is in the nano-composite. From this comparison, we can see that in order to improve the ferroelectric properties of self-assembled nano-composite thin films, it is necessary to exploit the ferroelectric properties of single phase ferroelectric materials. The better the properties of the perovskite phase, the better the properties of the nano-composite.

3.1 Introduction

Compared with bulk materials, thin films have constraint stresses imposed by the substrate which may notably change the structure and properties of the thin films. There are numerous reasons why a constraint stress can be generated between thin films and substrates, such as different thermal expansion coefficients, cooling rates, external electric fields, stresses induced by the growth process, etc. In all of these cases, the stress generated by lattice mismatch is the most important factor for epitaxial thin films [97]. Stress can also be applied by an elastic bending of the substrate during deposition and annealing [98-99].

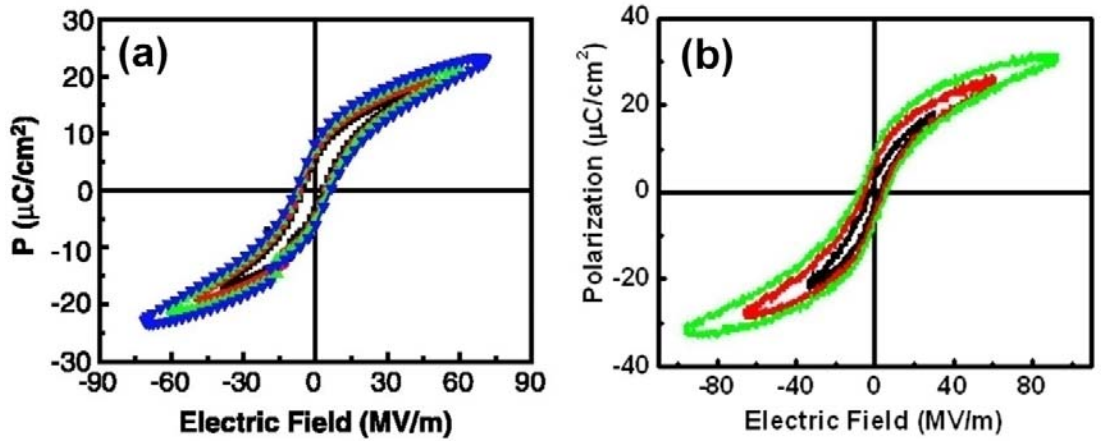

Figure 3.1 P-E hysteresis loops of (a) BTO-CFO self-assembled nano-composite thin film [Zheng et al (ref 26)]; and (d) BTO thin film.

The constraint stress of the thin film may be relaxed by increasing the thickness of the film. The critical thickness can be estimated by the Matthew-Blakeslee (or mechanical equilibrium) model, or by the People-Bean (or energy equilibrium) model [100-102]. Due to the relaxation of the compressive stress with increase of the film thickness, the lattice parameters (c and a) consequently decrease with increasing thickness. The polarization of tetragonal ferroelectrics decreases with decreasing film thickness due to compressive stresses, as observed for BTO, PTO, and PZT [103-109].

For these tetragonal ferroelectrics, such as BTO, PTO and PZT, the constraint stress is also able to alter their domain structures. There are three types of ferroelectric domains for tetragonal films or combinations thereof: a_1, a_2, and c which represent the lattice constant c that is oriented along the x (in-plane), y (in-plane) and z (out-of-plane) directions respectively [110]. Generally, when the stress changes from tensile to compressive, the volume ratio of the c domains increases [111-113]. Specifically, Alpay et al. [111] have calculated domain structures for tetragonal ferroelectrics and determined how the domain distribution changes with stress. Experimental findings for PTO and BTO agreed with their predictions. With increase of the c domain population, the polarization of the thin films was increased: this was simply because the polarization was measured in the out-of-plane direction.

Compressive stresses may also increase both the ferroelectric Curie temperature and the c/a ratio of tetragonal thin films. Choi et al. [114] selected $DdScO_3$ and $DyScO_3$ as substrates, which have lattice mismatches of -1.0% and -1.7% with BTO thin films respectively. They found that the Curie temperature of BTO increased from 130°C to 400°C for the $DdScO_3$ substrate, and to 540°C for the $DyScO_3$ substrate. Correspondingly, the c/a ratio of BTO increased from 1.011

to 1.026 for the $DdScO_3$ substrate, and 1.039 for $DyScO_3$. Furthermore, the polarization of BTO on $DyScO_3$ was 2.7 times higher than that of BTO single crystals.

By changing the orientation of the substrate, the direction of the constraint stress can be varied. Thus, the crystal structure of the perovskite phase may be different on variously oriented substrates/buffer layers, resulting in a change of ferroelectric properties. Accordingly, the topic which we will discuss below is the relationship amongst the substrate orientations, crystal structures, lattice parameters and ferroelectric properties.

3.2 Stress enhanced multi-ferroic properties of $Pb(Fe_{1/2}Nb_{1/2})O_3$ thin films

3.2.1 Deposition conditions and electrical properties of relaxor ferroelectric $Pb(Fe_{1/2}Nb_{1/2})O_3$ thin films prepared by pulsed laser deposition

A. Experimental procedure

In order to ensure the stoichiometric ratio of different ions, targets of PFN were prepared using a one-step solid-state reaction method. Powders of PbO (99.9%), Fe_2O_3 (99.945%), and Nb_2O_5 (99.9%) were batched in stoichiometric ratio with an excess of 5% PbO; ball-milled for 12 hours in IPA solution; calcined at 1123K for 3 hours; and subsequently re-milled, sieved, and powders pressed into a tablet under 30kPsi. The tablets were sintered for 3 hours by controlled atmosphere sintering to reduce Pb-loss using $PbO+PbO_2+ZrO_2$ powder. Epitaxial thin films of PFN were then deposited by PLD using these targets. Deposition was done on (001)-oriented $SrTiO_3$ substrates, and films with thicknesses of $50<t<500$nm were grown. The energy density of the KrF laser (Lambda 305i) was 1.6J/cm^2 at a wavelength of 248nm. The distance between the

target and substrate was 6cm. The growth rate of the PFN thin films was, for example, 10nm/min at a deposition temperature of 903K. A 50nm $SrRuO_3$ layer was used as a bottom electrode, which was deposited by PLD at 923K using a growth rate of 0.7nm/min. A 38μm×38μm top gold electrode was then deposited by sputtering. Films were grown at various deposition temperatures, oxygen partial pressures, laser frequencies, and thickness.

The structural and ferroelectric properties of the thin films were measured. X-ray diffraction (XRD) studies were performed using a Philips X'pert high-resolution system equipped with a two-bounce hybrid monochromator and an open three-circle Eulerian cradle. The analyzer was a Ge (220) cut crystal which had a θ-resolution of 0.0068°. The x-ray unit was operated at 45kV and 40mA with a wavelength of 1.5406Å ($Cu_{K\alpha}$). A Radiant Technology precision workstation was used to measure the resistivity and polarization of the PFN thin films, and a HP4284 LCR meter equipped with a MMR thermal stage was used to measure the dielectric constant as a function of temperature.

B. Fabrication and testing of PFN targets

Targets of PFN were sintered at different temperatures ranging from 1193K to 1313K. XRD line scans of these targets sintered at different temperatures are given in Figure 3.2a. The target sintered at 1193K was almost phase-pure perovskite, having only 1.6% volume fraction of a secondary pyrochlore phase. The phase purity was calculated by $\%\,pyrochlore = \frac{I_{pyro(222)}}{I_{pyro(222)} + I_{perov(110)}} \times 100\%$, where $I_{pryo(222)}$ is the intensity of the (222) pyrochlore peak and $I_{perov(110)}$ that of the (110) perovskite peak. However, with increasing sintering temperature, the %pyrochlore increased markedly and with other undetermined

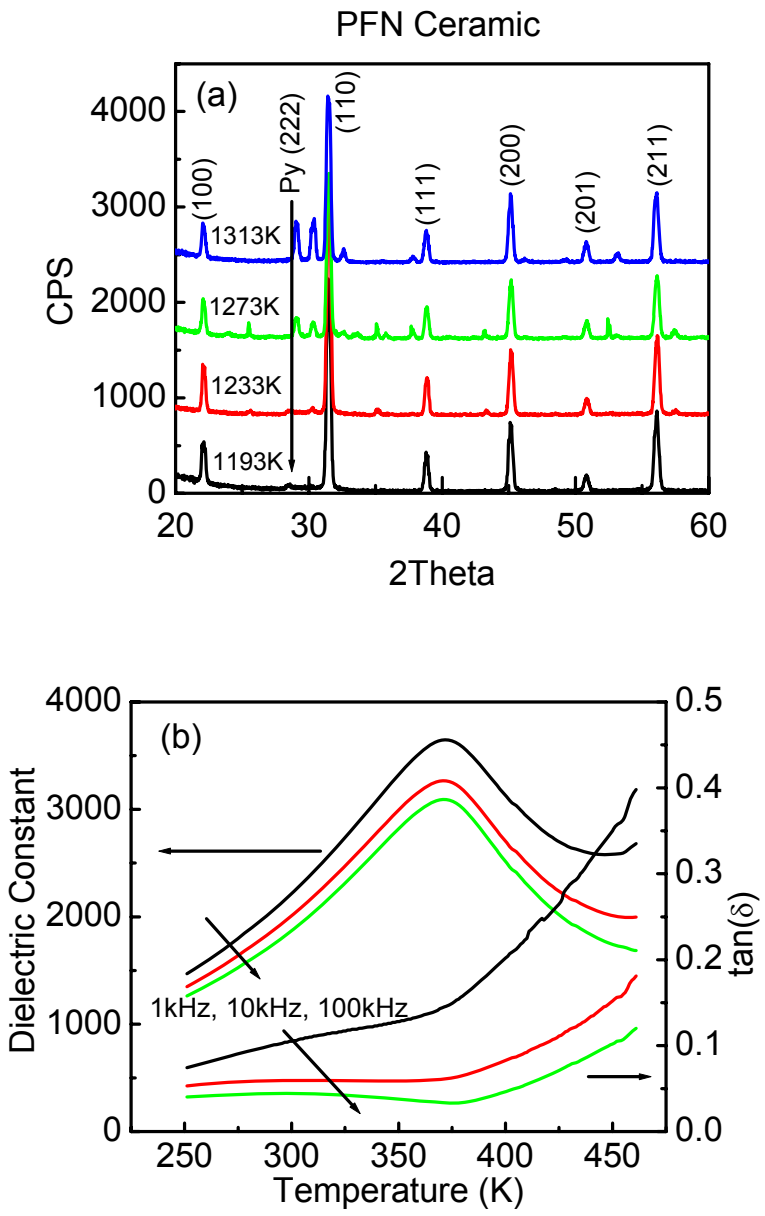

Figure 3.2 XRD and dielectric constant results of PFN ceramics. (a) Line scan over wide angles of PFN ceramics sintered at different temperatures; and (b) dielectric constant and loss as a function of temperature for various frequencies.

impurity peaks appearing. Also, with increasing sintering temperature, the density of the targets decreased, which demonstrates elemental loss on firing (presumably PbO). In order to maintain proper stoichiometry of the PFN target, we chose the one sintered at 1193K to be used for film deposition.

The dielectric constant of this PFN target (sintered at 1193K) is shown in Figure 3.2b. At room temperature, the values of the dielectric constant and loss factor were about K=2000 and tanδ=0.05 at V_{ac}=1V, respectively. The value of the dielectric constant and loss factor were both decreased with increasing measurement frequency, which is unlike that typical of a relaxor ferroelectric where tanδ increases with increasing frequency. The temperature dependent dielectric response revealed that the Curie temperature, determined by the temperature of the dielectric maximum (T_{max}), was T_c≈370K. A frequency dispersion of T_{max} was not distinct in the figure, as conventionally expected of a relaxor ferroelectric.

C. Confirmation of film epitaxy by XRD

The PFN thin films deposited on (001) SRO/STO were all found to be epitaxial phase-pure perovskites, as illustrated in Figure 3.3a. Unlike the PFN ceramic targets, we found no pyrochlore peaks by XRD in the films. The (002) peaks of PFN, SRO and STO were at 44.42°, 45.99°, and 46.49° respectively. With increasing film thickness, the full width half maximum (FWHM) decreased dramatically, as shown in Figure 3.3b; However, for t>200nm, it remained nearly unchanged (FWHM=0.27°) with further increase of thickness. In addition, with increasing film thickness, the intensity of its (002) reflection could be seen to increase quasi-linearly: simply because the thicker the film, the more planes from which to reflect. The structure of the (001) PFN films was recently discussed in another paper [115].

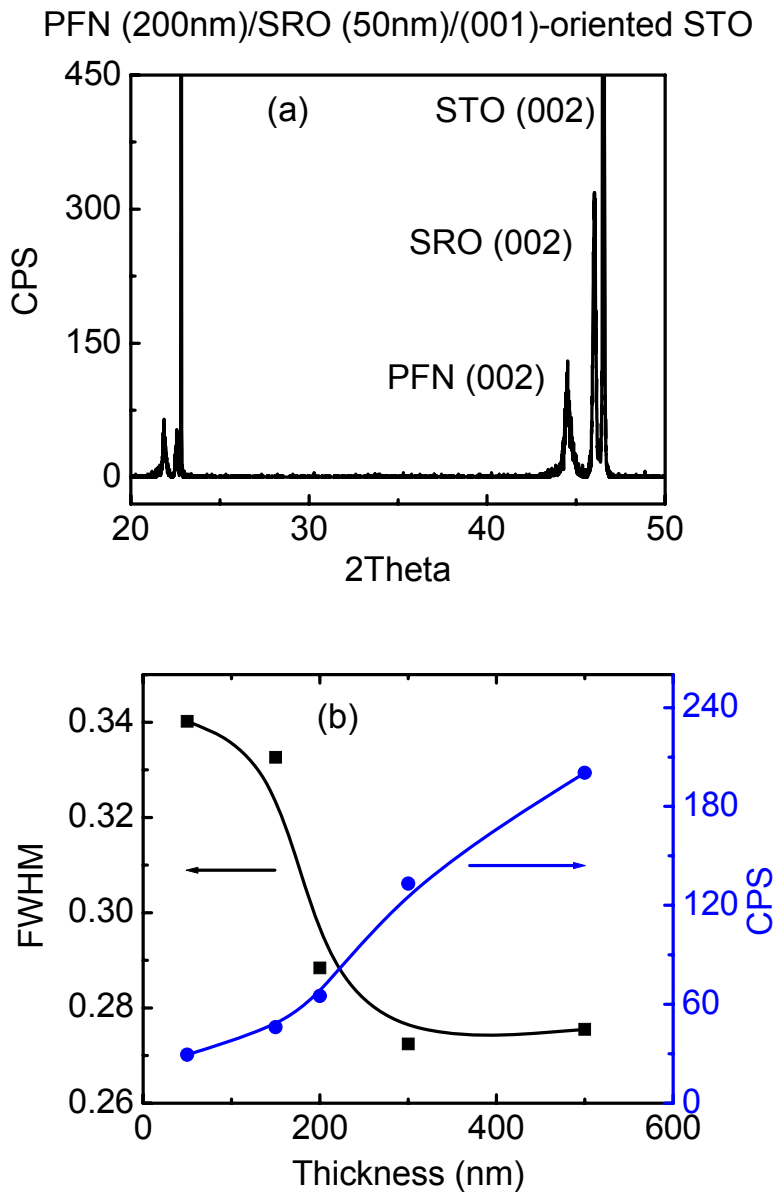

Figure 3.3 XRD results of PFN thin films. (a) Line scan over wide angles, demonstrating phase purity and good epitaxy; and (b) Full Width at Half Maximum (FWHM) and intensity of PFN (002) peaks (2θ) as a function of thickness.

D. Identification of optimum deposition conditions: ρ and P-E

For most perovskites, the deposition temperature window over which phase-pure films form is quite broad. In the case of PFN, phase pure perovskite films were formed from 883K to 943K. However, unfortunately, we found that the corresponding temperature window for achieving highly resistive films was quite narrow, as shown in Figure 3.4. For a deposition temperature of 903K, the resistivity of PFN reached values of up to $\rho > 5\times10^{8}\Omega$-cm; but, it decreased by nearly five orders of magnitude to $\rho = 5\times10^{3}\Omega$-cm, if the deposition temperature was changed by only 20K. Clearly, the temperature window over which insulating PFN films can be deposited is unusually narrow. This is consistent with difficulties in precisely tuning to an optimum stoichiometry.

We then determined the effects of ambient oxygen pressure (P_{O2}) from 15mTorr to 150mTorr and of laser frequency changes (ν) from 5Hz to 40Hz. The polarization curves for four (4) PFN thin layers deposited under different P_{O2} and ν conditions are given in Figure 3.5. From these P-E curves, we can identify that the best deposition condition was for ν=30Hz and P_{O2}=20mTorr. Only under these particular conditions was a slim P-E loop obtained; clearly, the deposition condition windows for insulating PFN layers capable of withstanding high voltages are very narrow. The gap at the bottom of the P-E curve at E=0 reflects the presence of a Schottky barrier ($\Delta\phi$) at the interface between the metal electrodes and PFN layer. If the resistivity of the film is $\rho \geq 10^{9}$, this gap is quite small: as can be seen in part (b) of the figure. Furthermore, the shape of the P-E response was found to be strongly dependent on ρ; if ρ is small, the P-E curve was more rounded and hysteretic, rather than sharp and slim. These results

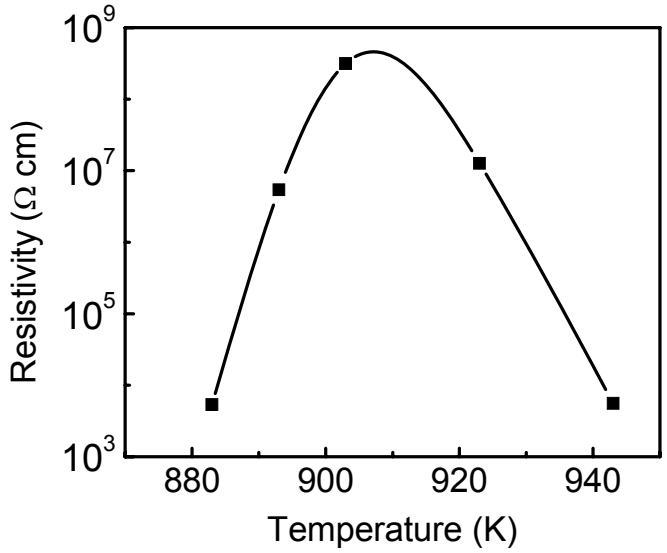

Figure 3.4 Resistivity of PFN thin film as a function of growth temperature.

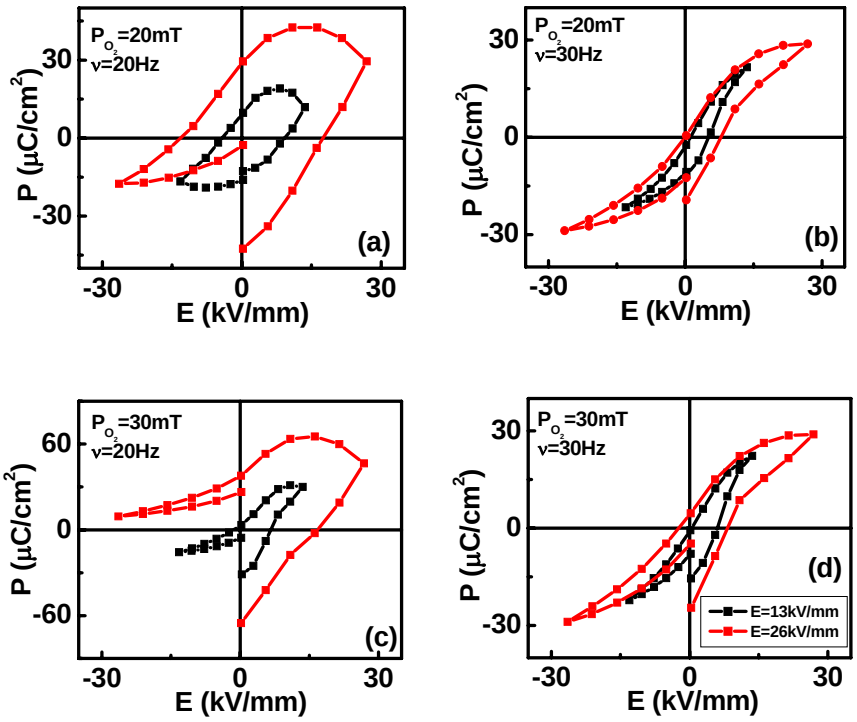

Figure 3.5 P-E curves of PFN thin film as a function of oxygen pressure and laser frequency. (a) Oxygen pressure is 20mTorr and laser frequency is 20 Hz; (b) oxygen pressure is 20mTorr and laser frequency is 30 Hz; (c) oxygen pressure is 30mTorr and laser frequency is 20 Hz; and (d) oxygen pressure is 30mTorr and laser frequency is 30 Hz.

demonstrate the extreme sensitivity of the high voltage characteristics of PFN films on oxygen stoichiometry, in addition to that on temperature. There is very limited flexibility in deposition conditions that allow achievement of high voltage insulation.

We next determined the effect of annealing time and cooling rate (data not shown). It was found that a 10 minute anneal was sufficient to achieve insulating films (for films deposited under otherwise optimum conditions), and that longer annealing time did not improve either ρ or the ferroelectric polarization characteristics. Furthermore, a cooling rate of 5K/min was found sufficiently slow to achieve these desired electrical properties. Finally, we determined that the energy of the laser notably affects film properties. If the energy is too low, the ratio of metal ions in the plasma is not the same as that of the target; this is because PbO easily evaporates from the target, whereas Nb does not. Alternatively, if the energy of the laser is too high, the surface of the film becomes rough and does not crystallize well. Our experience identified that laser energies of 1.6mJ/cm^2 were best suited for PFN deposition.

E. Effect of film thickness on ρ and P

The effect of film thickness was then investigated for 50nm<t<500nm. In Figure 3.6a, the dependence of ρ on t is shown. The resistivity was nearly independent of thickness for t>200nm, with ρ≈10^9Ω-cm. However, it decreased in a near linear manner with decreasing thickness below this critical value, reaching ρ≈10^6 Ω -cm for t=50nm. In the experiment, PFN thin films over the thickness range from 50nm to 500nm were studied.

Accordingly, only thicker PFN films could sustain sufficiently high electric fields that were capable of inducing significant polarization changes. Figure 3.6b shows the corresponding

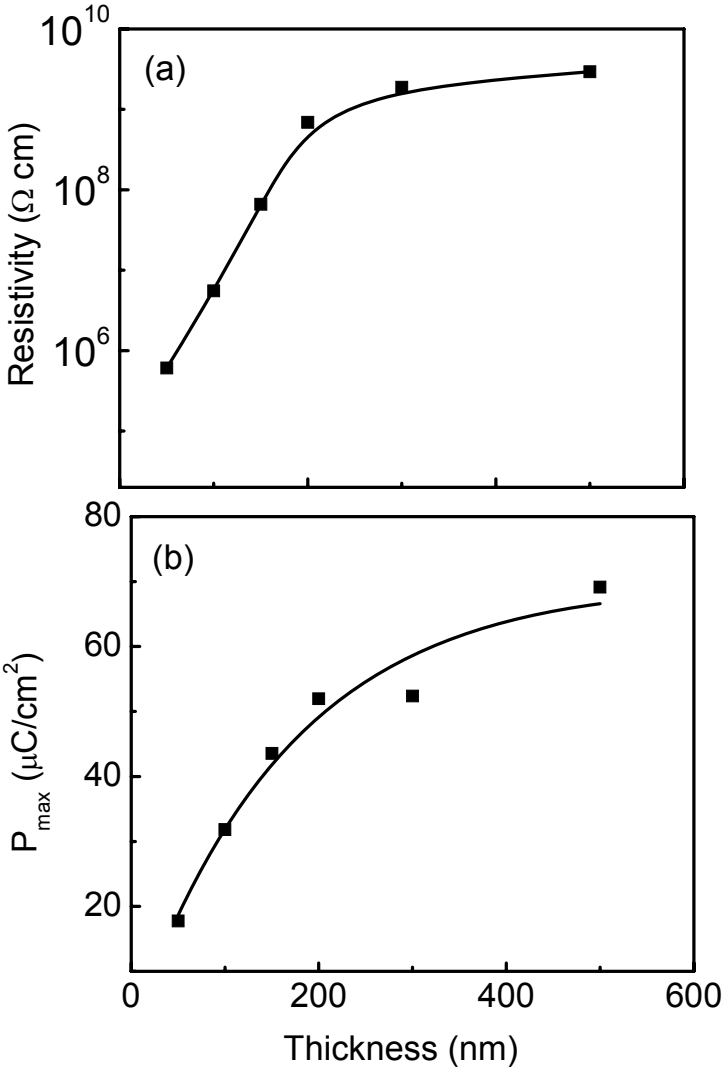

Figure 3.6 Resistivity and maximum polarization of PFN thin films. (a) Resistivity of PFN thin films as a function of thickness; and (b) maximum polarization of PFN thin films as a function of thickness from 50nm to 500nm.

dependence of the maximum induced polarization (P_{max}) on film thickness, which can also be seen to increase with increasing t. Inspection of this figure will reveal for thicker films that $P_{max} \leq 70 \mu C/cm^2$ could be induced; whereas, extrapolation of P_{max} to t=0, yielded extraneous values of $\leq 10 \mu C/cm^2$ consistent with previously reported values for bulk crystals/ceramics. This finding of higher induced polarizations in films is due to the simple fact that very high electric fields could be applied to the films before dielectric breakdown occurred, and did not (as far as we can tell) result from an intrinsic polarization change with t. This is further illustrated in Figure 3.7, which shows that P_{max} increases near linearly with increasing electric field for E>50kV/mm: until, that is, dielectric breakdown occurs. Basically, the polarization does not saturate. Field levels as high as E=190kV/mm could be sustained on films of thickness t≈500nm. It is also interesting to note in-spite of this large P_{max} that the remanent polarization was only $P_r=17 \mu C/cm^2$, with a small coercive field of E_c=9kV/mm.

Clearly, the ferroelectric polarization characteristics of PFN layers are unique offering (i) low remnant polarizations (P_r); (ii) low coercive fields (E_c); (iii) large induced polarizations, in particular relative to P_r; and (iv) slim P-E loops with low hysteretic losses, typical of a relaxor ferroelectric. These findings are in stark comparisons to the lossy P-E loops of bulk PFN ceramics/crystals which have low induced polarizations. Interestingly, the thinner films had resistivities and P-E responses similar to that of bulk crystals/ceramics, than thicker films: $\rho \approx 10^5 \Omega$-cm and $P_{max} \approx 10 \mu C/cm^2$. This fact underscores the unusual nature of the narrow deposition windows required to make sufficiently insulating PFN films, suggesting an important role in achieving a specific cation stoichiometry that limits spatial dimensions over which valence band hoping can occur.

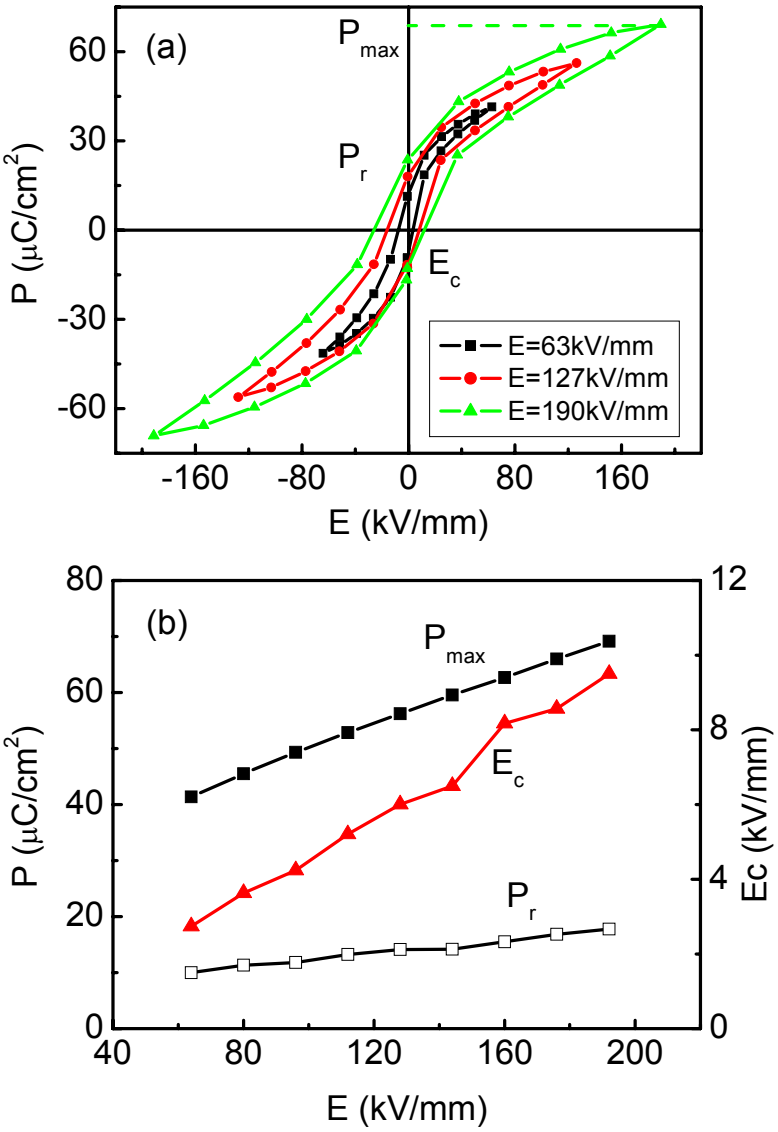

Figure 3.7 Polarization of PFN thin films. (a) P-E curves of PFN thin film for different maximum electric field; and (b) P_{max}, E_c and P_r of PFN thin films as a function of electric field.

F. Phase transformation characteristics: temperature dependence of K.

Figure 3.8 shows the temperature dependent complex dielectric constant for various measurement frequencies at V_{ac}=0.1V. The data reveal a frequency dispersion of the dielectric constant; where K decreases with increasing frequency, with T_{max} shifting to higher temperatures. Such dielectric dispersion is typical of a relaxor ferroelectric. The Curie temperature range was in the vicinity of 375K to 400K, consistent with that of bulk ceramics (see Fig.1b). These findings demonstrate that epitaxial constraint does not alter the phase transformational characteristics.

It is also relevant to note that the dielectric loss factor (tanδ) increased with increasing frequency. This is unlike that for bulk PFN ceramics (see Fig.3.2b), which decreased with increasing frequency, due to relaxing out of the space charge polarization mechanism. Rather, again, this component of the dielectric response is similar to that found in relaxor ferroelectrics. At higher temperatures, greater than the Curie range, clear evidence of space charge polarization contributions to the loss was evident. The onset of conduction contributions at T>400K correlates to corresponding increases in the real component of the response towards a secondary maximum. These findings furthermore underscore the fact that we have suppressed conduction in our PFN films by careful tuning of the deposition window.

G. Section Summary

To achieve resistivities of $>10^9\Omega$-cm, a minimum critical criterion for dielectric insulators, the deposition conditions of PFN need to be restricted to a very narrow deposition window: 903K deposition temperature, 20 mTorr oxygen pressure and 30Hz laser frequency

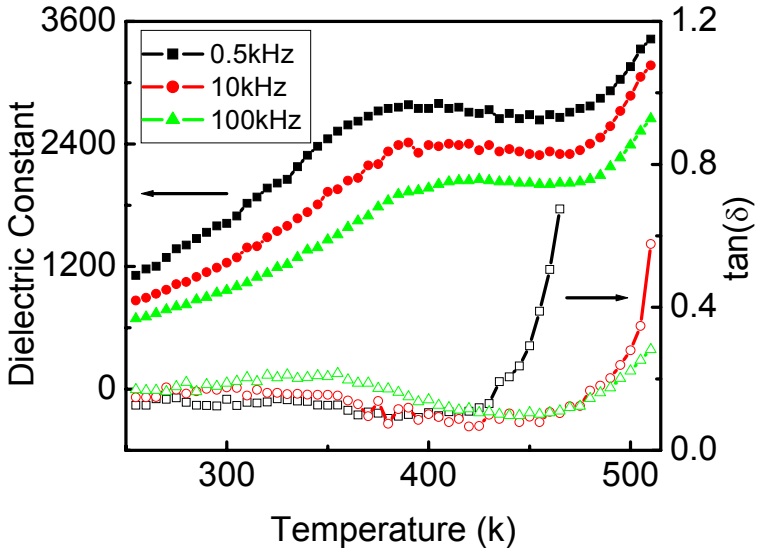

Figure 3.8 Dielectric constant and loss of PFN thin film as a function of temperature for various frequencies.

(using the chamber we built at Virginia Tech). Changes of only 10K in temperature, 10mTorr in oxygen pressure or 10Hz in laser frequency result in a dramatic decrease in resistivity. Because of the higher resistivity in films prepared within this narrow deposition window, we can (i) sustain higher applied electric fields of up to E<190kV/mm; (ii) achieve induced polarizations of up to 70μC/cm^2, which are 3x (7x) higher than prior reported values for PFN films (crystals); and (iii) offer dielectric constants of up to K=1200 at room temperature.

3.2.2 Structure of (001), (110), and (111) oriented $Pb(Fe_{1/2}Nb_{1/2})O_3$ epitaxial thin films on $SrRuO_3$ buffered $SrTiO_3$ substrates

A. Crystal structure and lattice parameters of various oriented PFN film at room temperature

Figures 3.9a - 3.9c show mesh scans for (001), (110), (111) oriented PFN/SRO/STO heterostructures. We can see that the PFN films are phase-pure perovskite that are epitaxial with STO. The residual stress of the (111) oriented film is less than that of the (110) one, the stress of which is less than that of the (001) oriented film. Line scans for the (002), (110) and (111) peaks are shown in Figure 3.9d, e and f respectively: each figure contains data for (001), (110) and (111) oriented PFN thin films. Analysis of these X-ray data allowed for the determination of the structure and lattice parameters of the various oriented films

The structure of the (001) oriented PFN thin film is tetragonal (see Figure 3.10a), which is the same as that of the intermediate ferroelectric phase of bulk PFN crystals/ceramics in the temperature range of 353 and 393K. The lattice parameter c_t was 4.068Å for a 100nm-thick PFN layer as determined from the (002) peak; and a_t was determined to be 4.010Å by analysis of the

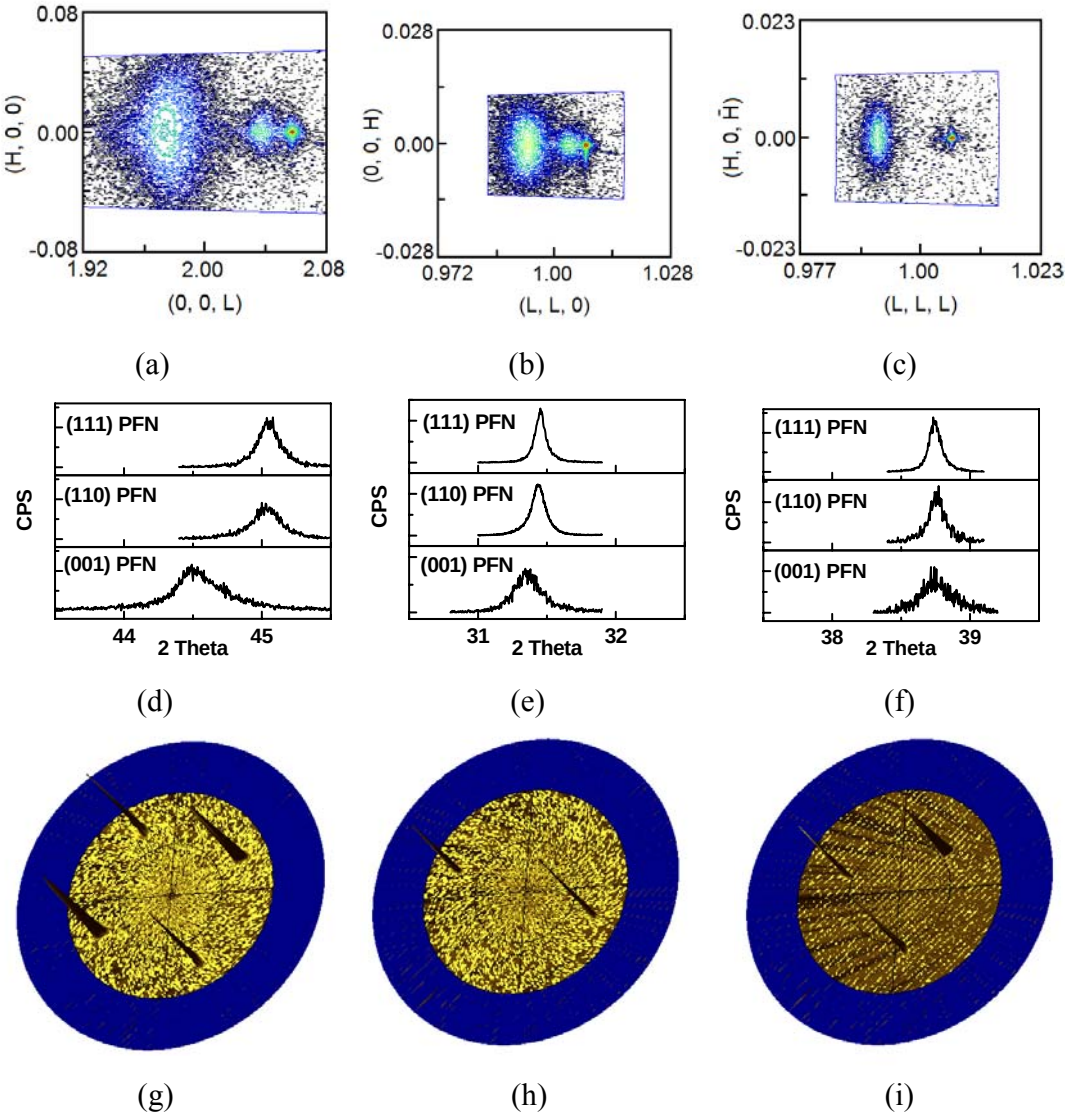

Figure 3.9 XRD results: mesh scans, line scans and pole-figure scans of PFN thin films. (a) Mesh scan of (001) oriented film; (b) mesh scan of (110) oriented film; (c) mesh scan of (111) oriented film, demonstrating phase purity and good epitaxy; (d) line scan of (002) peaks; (e) line scan of (110) peaks; (f) line scan of (111) peaks; (g) pole-figure scan of (001) oriented PFN film; (h) pole-figure scan of (110) oriented PFN film; and (i) pole-figure scan of (111) oriented PFN film, demonstrating the symmetry of the PFN films.

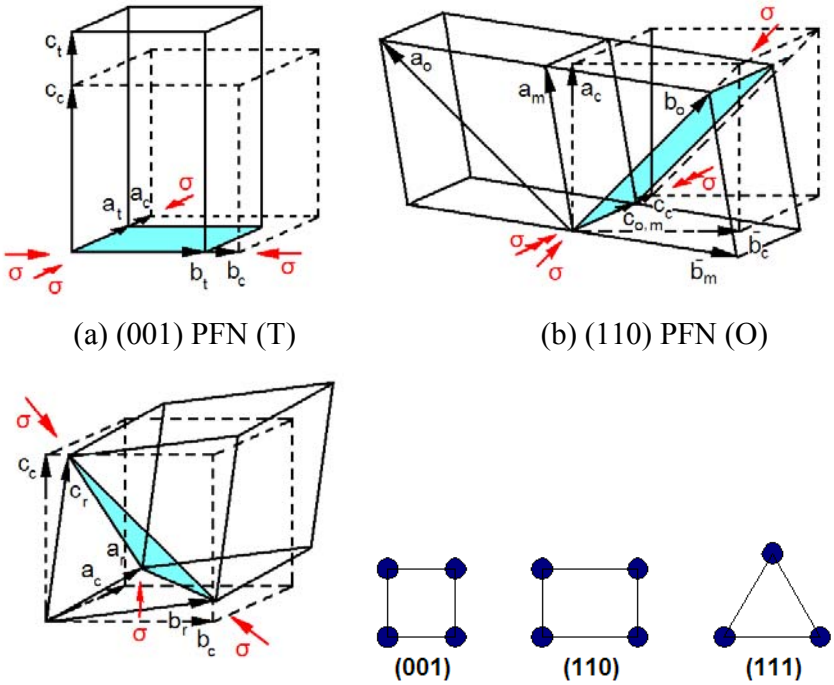

(a) (001) PFN (T) (b) (110) PFN (O)

(c) (111) PFN (R) (d) Stacking methods of substrates

Figure 3.10 Structure and stress of various oriented PFN films. (a) Tetragonal structure of (001) oriented PFN film, and stress along <100> and <010> directions; (b) Orthorhombic (or Monoclinic) structure of (110) oriented PFN film, and stress along <1 $\bar{1}$ 0> and <010> directions; (c) Rhombohedral structure of (111) oriented PFN film, and stress in (111) plane; and (d) Stacking method on the surfaces of the variously oriented substrates.

(002) and (101) peaks. The value of $d_{(111)}$ was then used to verify the value of the lattice parameters c_t and a_t, whose result was a match. The four values of $d_{\{101\}}$ were nearly equivalent, where the error difference was smaller than the resolution of the XRD system. Furthermore, for a tetragonal structure, the <001> (i.e. c-axis) must be a four-fold rotation axis. Figure 3.9g shows a pole-figure scan of the {101} peaks about the same <001> axis for a (001) oriented PFN film. Accordingly, there are four equivalent {110} peaks, with nearly the same intensity, which are rotated from each other by an angle of Ø=90°. These results clearly confirm that the c-axis of the PFN film is fixed by the (001) axis of the substrate, and that there are four equivalent {101} planes consistent with a tetragonal structure.

The structure of the (110) oriented PFN thin films was a double-cell orthorhombic, or equivalently a limiting monoclinic C (M_c) single-cell representation, as shown in Figure 3.10b. The O phase has not been previously reported in PFN crystal or ceramics. For the single-cell representation, we determined the M_c lattice parameters for a 100nm-thick PFN film to be $a_m=b_m=$ 4.029Å and γ=89.93° by analysis of (200) and (110) peaks, and c_m=4.017Å by analysis of (110) and (111) peaks. Whereas, in double-cell representation, the lattice constants of the O phase were determined to be (a_o, b_o, c_o)=(5.702Å, 5.694Å, 4.017Å). These representations are equivalent, and in this thesis we chose to refer to the higher symmetry O structure. Figure 3.9h shows a pole-figure scan of the {200} peaks taken about the <110> axis of a (110) oriented PFN thin film: two {200} peaks with equal intensity, which are rotated by Ø=180º, can be seen consistent with the O structure. For PFN single crystals, Bonny et al. has also reported a monoclinic phase with a double-cell at 297K [116]. The difference between the O phase for (110) oriented PFN thin films and the M phase for single crystal is the angle β: which is 90.1° for the crystal (i.e., the M was a slightly distorted O structure).

The structure of the (111) oriented PFN thin film was rhombohedral, as illustrated in Figure 3.10c, which was the same as that of PFN crystals/ceramic at room temperature. From analysis of (200) and (110) peaks, we determined that $a_r=b_r=c_r=4.027$Å and $\alpha=89.96°$ for a 100nm-thick PFN layer. These same values were also confirmed by analysis of (200) and (111) peaks. Pole-figure scans of the {110} peaks around about the <111> axis for a (111) oriented film revealed a 3-fold axis of rotation as shown in Figure 3.9i. The facts that $d_{(200)}=d_{(020)}=d_{(002)}$ and that there was 3-fold {110} pole scan prove that (111) PFN films are rhombohedral.

B. Structure of PFN thin films: role of epitaxial stress and lattice mismatch

The reason why the T phase with $c_t/a_t=1.015$ is favored for (001) PFN layers is shown in Figure 3.10a. An axial compressive stress acts along the <100> and <010> direction on the (001) face between the PFN film and the (001) SRO/STO substrate. The structure is similar to the intermediate phase of PFN single crystals in the temperature range of 353K and 393K, but has a change in c_t/a_t due to epitaxial constraint. If the film was stress free in all directions and if there was no striction associated with any phase transformations, then the lattice parameters would be $a_c=b_c=c_c\approx4.028$Å at room temperature. However, the lattice parameter of SRO is $a_c=3.923$Å, which is smaller than that of PFN. Thus, the a_t and b_t lattice parameters of PFN thin films are compressed equally to 4.010Å, and c_t expanded to 4.068Å. The tetragonal cell volume is nearly equivalent to that of the presumed C, as $a_t^2c_t=a_c^3=65.4$Å^3.

The reason why the O phase is favored for (110) films is that an anisotropic stress acts along the <001> and $<1\bar{1}0>$ directions on the (110) face between the PFN film and SRO/STO substrate, as illustrated in Figure 3.10b. Since in the (110) plane, the compressive stress along $<001>_c$ is larger than that along $<1\bar{1}0>_c$ in the (110) plane, b_o is compressed from 5.698Å to

5.694Å by the stress acting along $<1\bar{1}0>_c$, c_o is compressed from 4.028Å to 4.017Å by the $<001>_c$ stress, and a_o expands from 5.698Å to 5.702Å.

The (111) film is rhombohedral, similar to crystals/ceramics. An isotropic compressive stress is applied by the (111) SRO/STO substrate on the PFN film, as shown in Figure 3.10c. Accordingly, (111) PFN thin films can not change their crystal structure, and the R phase is maintained. Interestingly, the rhombohedral lattice parameters of the film are larger (a_r=4.027Å) than those previously reported for PFN crystals (a_r=4.012Å); however, the cell volume of the film is nearly equal to that of the presumed C structure ($a_r^3 \sin\alpha_r = a_c^3 = 65.4Å^3$).

The reason for the constraint stresses being different for the variously oriented films is different stacking patterns on the substrate surfaces, as illustrated in Figure 3.10d. The stacking patterns on the (001), (110) and (111) SRO/STO substrate surfaces are square, rectangular and triangle respectively. Although the lattice constant of PFN is slightly larger (2%~4%) than that of SRO, PFN grew epitaxially on SRO/STO substrates. Thus, a constraint stress is generated, and the stresses are different for the variously oriented substrates.

C. Phase transformational sequences with temperature

The dependence of the lattice parameters of a 150nm-thick (001) oriented PFN thin film on temperature is shown in Figure 3.11a. In this figure, we can see a change in the slope of the thermal expansion near 400K, which is close to the T_c previously reported for crystals/ceramics. The lattice parameters in both the high and low temperature phases were tetragonal. Thus, we designate the transformational sequence as T→T', where presumably T is paraelectric and T' is ferroelectric. A tetragonal distortion of c_t/a_t=4.014 persists to 600k, whose linear extrapolation to

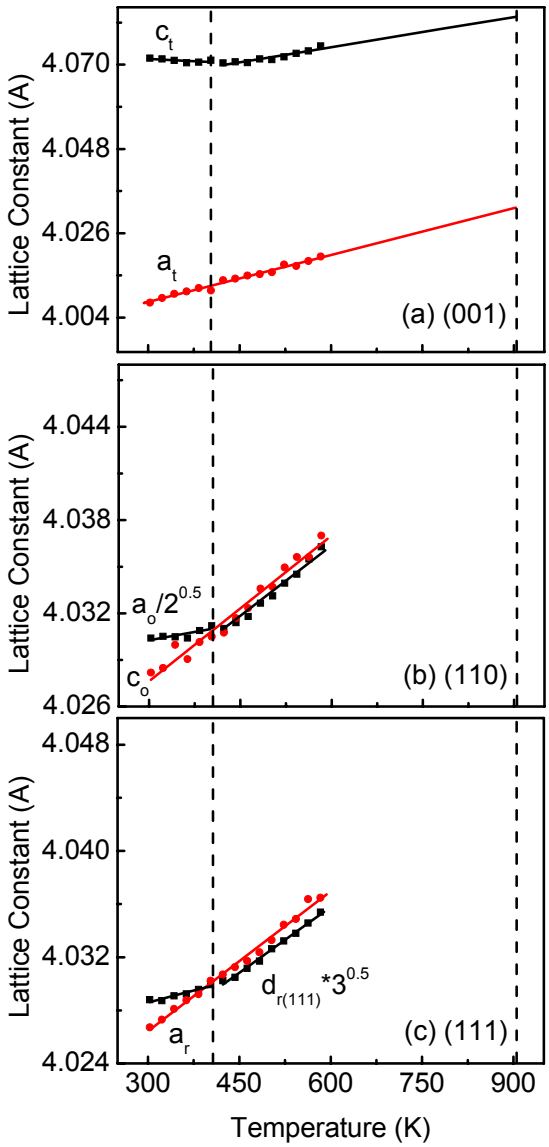

Figure 3.11 Lattice parameters of various orientated PFN films as a function of temperature. (a) a_t and c_t lattice parameters of (001) PFN film as a function of temperature, demonstrating T→T' phase transition; (b) $a_o/\sqrt{2}$ and c_o lattice parameters of (110) PFN film as a function of temperature, demonstrating C→O phase transition; and (c) $d_{r(111)}/\sqrt{3}$ and a_r lattice parameters of (111) PFN film as a function of temperature, demonstrating C→R phase transition.

the deposition temperature of 900K yields c_t/a_t=1.012. This demonstrates that a tetragonal distortion is induced by epitaxial stress from the substrate during the film formation, rather than by a consequence of a ferroelectric phase transformation.

However, for the (110) and (111) oriented PFN thin films, the structural distortions from the cubic prototype are direct consequence of a ferroelectric transformation. The dependence of the lattice parameters for 150nm-thick (110) and (111) PFN thin films on temperature are shown in Figures 11b and 11c. In these figures, we can again see a change in slope of the thermal expansion at a Curie temperature of T_c≈400K, which corresponds to that of crystals/ceramics [30, 33]. In both cases, the high temperature phase is cubic. However, the structures of the low-temperature ferroelectric phases were different: (110) was O, and (111) was R. The values of the lattice parameters in both cases were quite similar over the entire temperature range.

D. Thermal expansion of PFN thin films

The volumetric/linear thermal expansion coefficients or TEC (β/α) of STO and PFN that were previously reported in the literature are summarized in Table 3.1. The volumetric TEC of STO is constant (3.23×10^{-5} K^{-1}) over a wide temperature range (300K~2000K) [117-119]. For PFN, the volumetric TEC changes considerably both below and above the Curie temperature. The value of the volumetric coefficient β1 is 0.36×10^{-5} K^{-1} between room temperature and T_c; whereas for temperatures above T_c, β2 increases to 3.3×10^{-5} K^{-1} [120-122] becoming nearly equal to the value of STO.

To study the thermal expansion of PFN thin films and STO substrate, the in-plane and out-plane lattice constants of PFN films and the lattice constant of STO were measured from

Table 3.1 Thermal Expansion Coefficient (TEC) of STO substrate and PFN thin films

Volumetric TEC	β (10^{-5} K^{-1})	ΔT (K)			Reference
STO	2.82	110-300			ref. 117
	2.59	113-301			ref. 118
	3.23	300-2000			ref. 119
	3.18	303-583			This study
Volumetric TEC	β1 (10^{-5} K^{-1})	ΔT (K)	β2 (10^{-5} K^{-1})	ΔT (K)	
Bulk PFN	0.318	RT			ref. 120
	0.288	300-385	3.828	445-800	ref. 121
	0.36	300-393	3.3	>393	ref. 122
(001) PFN film	1.96	303-383	2.88	463-583	This study
(111) PFN film	2.37	303-383	3.19	463-583	This study
linear TEC	α (10^{-5} K^{-1})	ΔT (K)			
a_t of (001) PFN film	1.01	303-583			This study
c_o of (110) PFN film	0.981	303-583			This study
$d_{r(10\bar{1})}$ of (111) PFN film	1.02	303-583			This study
STO substrate	1.06	303-583			This study

303K to 583K. As shown in Figure 3.12a, the lattice constant a_t of (001), c_o of (110) and $d_{r(10\bar{1})}$ of (111) PFN thin films increased near linearly with increasing temperature. Over the temperature range investigated, the mismatch between the in-plane lattice constants of PFN thin films and that of the STO substrate was essentially constant. Accordingly, this shows that the strain between the PFN film and substrate are also unchanged on heating in the range of 303K to 583K. The values of ΔL/L between the in-plane lattice constant of PFN films and those of the STO substrate are shown in Figure 3.12b as a function of temperature. As can be seen in this figure, the linear TEC of the in-plane lattice constants for PFN films and that of the STO substrate are nearly the same in the temperature range between 303K and 583K. Values of the linear TEC for the in-plane lattice constant of PFN (1×10^{-5} K^{-1}) are then summarized in Table 3.1, where they can be seen to be similar to those for STO (1.06×10^{-5} K^{-1}). Because of the elastic constraint imposed by the SRO/STO substrate, the linear TEC of the in-plane lattice constant of PFN films both below and above Curie temperature is constant: this is notably different from that of bulk PFN crystals and ceramics.

The thermal expansion volume for each PFN film was then calculated as a function of temperature, using the lattice constants. The values of ΔV/V for the (001) and (111) PFN films and the STO substrate are shown in Figure 3.12c as a function of temperature. For the PFN films at temperatures above T_c, the volumetric TEC was 3×10^{-5} K^{-1} which was about the same as that of STO; whereas below T_c, it had a lower value of 2×10^{-5} K^{-1} which is still notably larger than that of bulk PFN. The reason for the reduction in the volumetric TEC of PFN films is probably the change in the out-plane lattice constant below T_c. Because of the epitaxial constraint imposed by the substrate, the volumetric thermal expansion of PFN can not be as small as that of bulk PFN.

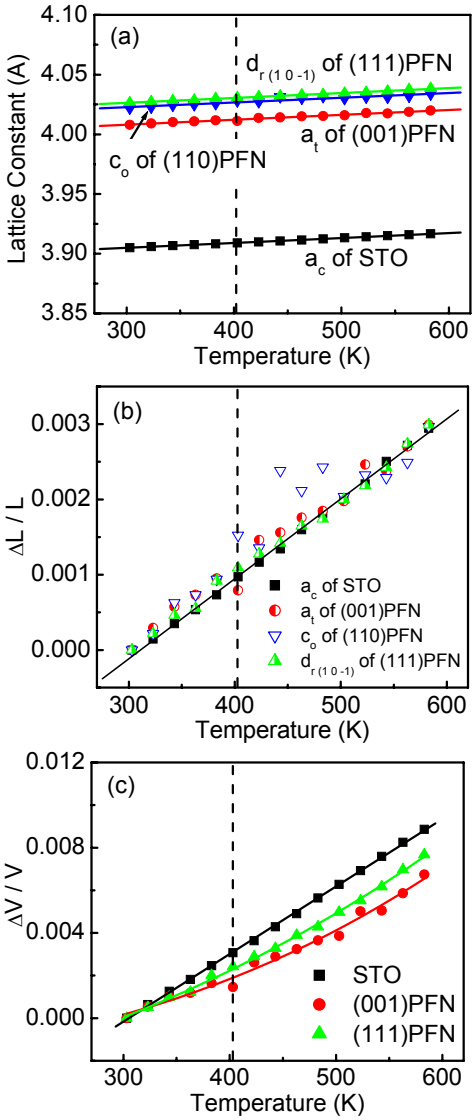

Figure 3.12 Thermal expansions of various oriented PFN thin films and STO substrate as a function of temperature. (a) in-plane lattice constants of PFN thin films and lattice constant of STO substrate as a function of temperature; (b) ΔL/L of in-plane lattice constant of PFN thin films and STO substrate as a function of temperature; and (c) ΔV/V of PFN thin films and STO substrate as function of temperature.

E. Thickness dependence of lattice parameters

The dependence of the lattice parameter for (001) PFN thin films on film thickness is shown in Figure 3.13a. These films were all tetragonal, and the lattice parameters were nearly independent of film thickness. These results demonstrate that the epitaxial stress in (001) films is not relaxed with increasing film thickness (at least for t≤500nm).

However, for the (110) and (111) films, the lattice parameters were notably dependent on film thickness. For the (110) film, Figure 3.13b shows that $a_o/\sqrt{2}$ and $b_o/\sqrt{2}$ both decreased with increasing film thickness for t≤150nm, whereas c_o increased. Near t=150nm, the structure appeared pseudo-cubic with $a_o/\sqrt{2} \approx b_o/\sqrt{2} \approx c_o$. The reason for the thinner films having $a_o/\sqrt{2}$ and $b_o/\sqrt{2}$ larger than C_o is that the compressive stress along <001> is larger than that along $<1\bar{1}0>$ in the (110) plane. The results show for (110) PFN that increasing film thickness relaxed the epitaxial stress, accordingly the orthorhombic distortion of the structure was reduced. Similarly, the small rhombohedral distortion of the (111) PFN thin layers was reduced with increasing film thickness, as shown in Figure 3.13c. In fact, the structure of the thicker (111) films was seemingly pseudo-cubic.

F. Section Summary

Our structural investigations demonstrate that the phase transformational sequence of PFN thin films grown on $SrRuO_3$-coated $SrTiO_3$ substrates depends on orientation: (i) T→T' for (001) layers, (ii) C→O for (110) layers, and (iii) C→R for (111) ones. The O and T' phases do not exist in bulk PFN crystals/ceramics at room temperature. The change in transformational sequence with orientations is attributed to epitaxial stress.

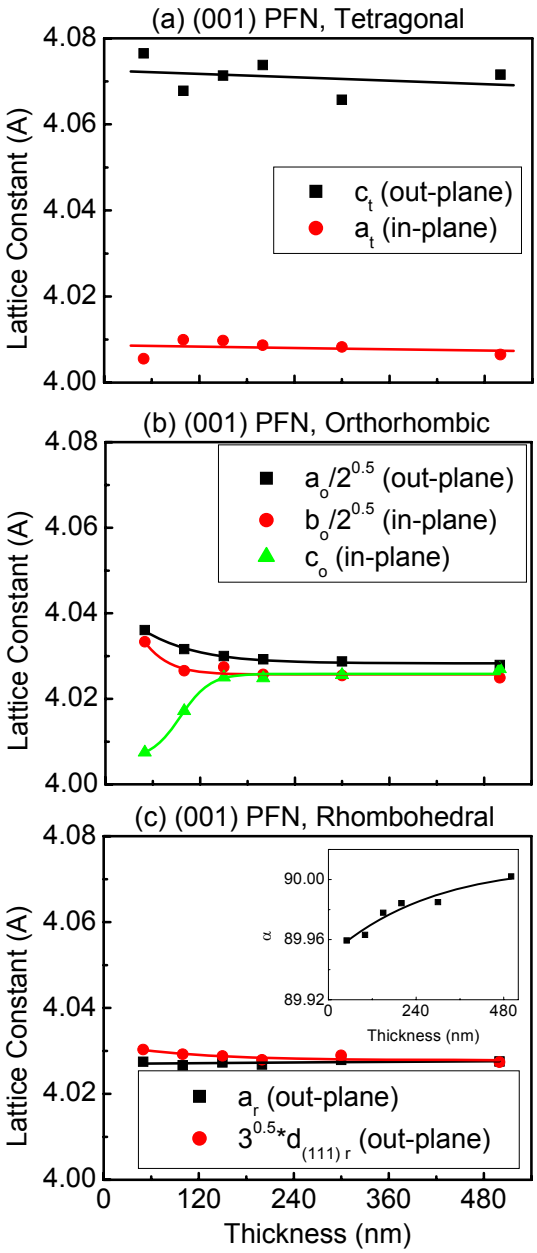

Figure 3.13 Lattice parameters of various orientated PFN films as a function of film thickness. Lattice parameters of (a) (001), (b) (110), and (c) (111) PFN film as a function of film thickness, where the insets of (c) shows α of (111) PFN film.

3.2.3 Enhancement of multi-ferroic properties of $Pb(Fe_{1/2}Nb_{1/2})O_3$ thin films on $SrRuO_3$ buffered $SrTiO_3$ substrates

We deposited and characterized three sets of samples which were grown on (001), (110), and (111) STO: these were designation as S1, S2 and S3. S1 were 200nm PFN films deposited on STO substrates; S2 were 200nm PFN films deposited on top of a 50nm SRO buffer layer grown on STO substrates; and S3 were 400nm PFN films deposited on top of a 50nm SRO buffer grown on STO substrates. The thicknesses of the thin films were controlled by the deposition time, and were measured by scanning electron microscopy.

The structure and surface morphology of the PFN thin films were measured by XRD and atomic force microscopy, respectively. XRD line scans of PFN thin-layers grown on (001), (110) and (111) STO substrates buffered with a SRO thin-layer are shown in Figure 3.14a. From this figure, we established that all of our thin-layers were phase-pure perovskite and also epitaxial. Mesh scans (not shown) demonstrated good epitaxy on the substrate. The atomic force image shown in Figure 3.14b reveals a surface roughness of ~10nm and an average crystallite size of ~150nm.

We need to determine the in-plane constraint stress of PFN thin films for the variously oriented substrates. The generalized Hooke's law is as follows:

$$\varepsilon_x = \frac{1}{E}\left[\sigma_x - v\left(\sigma_y + \sigma_z\right)\right],\ \varepsilon_y = \frac{1}{E}\left[\sigma_y - v(\sigma_x + \sigma_z)\right],\ \varepsilon_z = \frac{1}{E}\left[\sigma_z - v\left(\sigma_x + \sigma_y\right)\right];\quad (1)$$

where ε_i is the strain tensor, σ_i is the stress tensor, E is Young's modulus, and v is Poisson's ratio. In the thin film, $\sigma_z = 0$, $\varepsilon_i = \frac{a_i - a_0}{a_0}$, where a_i is the equivalent lattice constant of thin film in i (x,

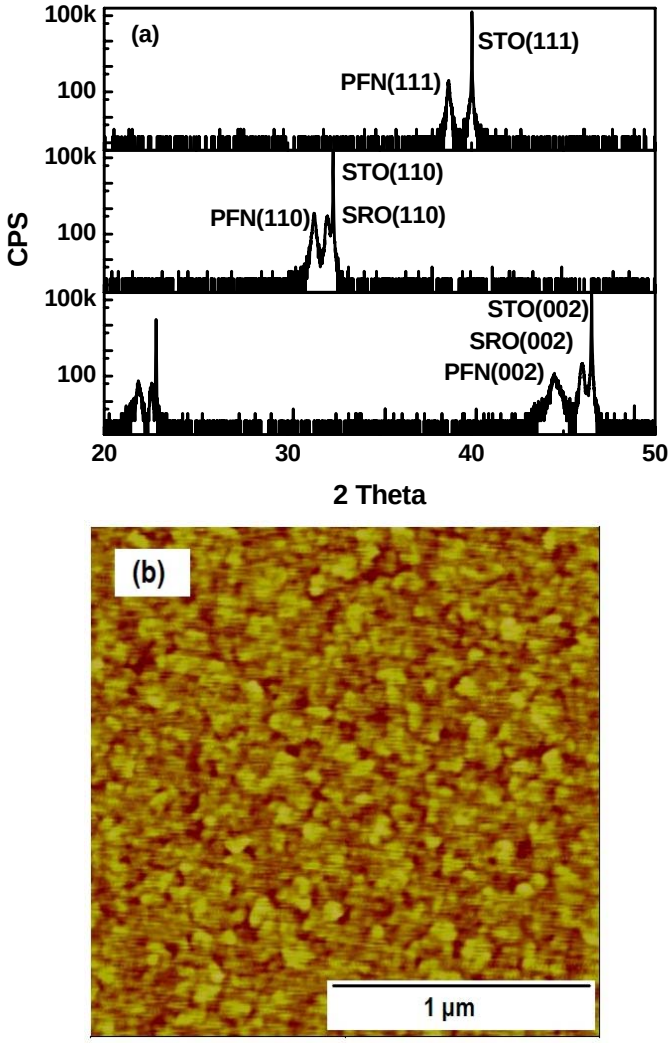

Figure 3.14 XRD and AFM result of PFN thin film. (a) Line scan over wide angles, demonstrating phase purity and good epitaxy; and (b) AFM image demonstrating the morphology of a typical PFN film.

y or z) directions. In our calculation, PFN is assumed to be pseudo cubic at room temperature, with a lattice constant of $a_0 = \sqrt[3]{V}$. Accordingly, the in-plane stress imposed on the PFN thin film by the substrate is simplified to:

$$\sigma_{in-plane} = \frac{\sigma_x + \sigma_y}{2} = E\left(\frac{a_x + a_y - a_z - a_0}{2a_0}\right) = E\varepsilon_E; \quad (2)$$

where $\varepsilon_E = \left(\frac{a_x + a_y - a_z - a_0}{2a_0}\right)$ is proportional to $\sigma_{in-plane}$, and is defined as the equivalent in-plane strain. This estimate of $\sigma_{in-plane}$ is more accurate for calculations than the widely used lattice mismatch, $(\frac{a_{film} - a_{substrate}}{a_{substrate}})$, which accounts for in-plane stress between substrate and epitaxial layer. The value of ε_E is -1.0×10^{-2}, -6.3×10^{-4} and -3.8×10^{-4} for 200nm (001), (110) and (111) oriented PFN thin films respectively. The negative values mean that the constraint stress is compressive. Please note that the in-plane constraint stress on (001) is more than 10x larger than that on (110) and (111).

The piezo-response hysteresis-loops for differently oriented PFN thin films (S2) are shown in Figure 3.15. In these measurements, the AC voltage was 2V at 6kHz (which was the resonant frequency of the PFN thin film). The coercive field was 7V. The value of the piezoelectric coefficient d_{33} for (001) oriented PFN thin film was much higher than the other orientations, reaching a maximum value of 40pm/V for V>15V; whereas, d_{33} for (110) and (111) PFN thin films was 28pm/V. Comparisons of these findings to our estimates for $\sigma_{in-plane}$ reveal that larger constraint stress results in more strongly piezoelectric layers.

Next, the temperature dependence of the magnetization of S1 is shown for variously oriented 200nm PFN films, as given in Figure 3.16. The films were zero-field-cooled (ZFC) to

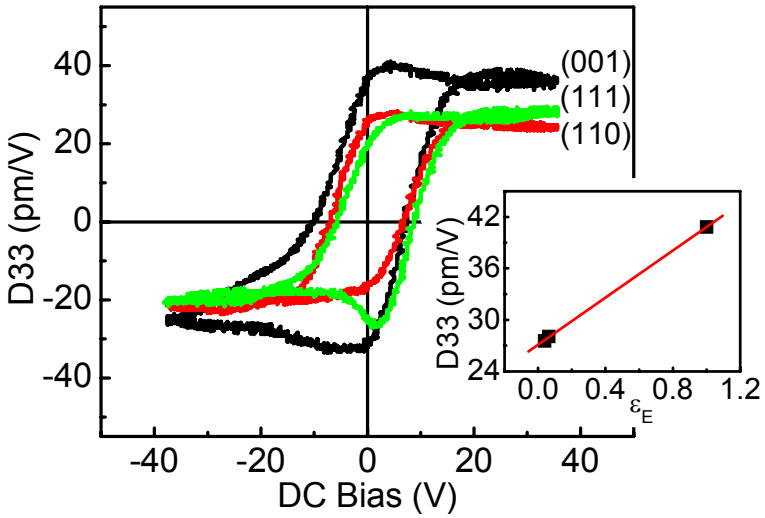

Figure 3.15 Piezo-response hysteresis loops for (001), (110) and (111) oriented PFN thin films. Insert shows the piezo coefficients as a function of constraint stress. The data illustrate that the d33 of (001) PFN thin film is much higher than the other two orientations.

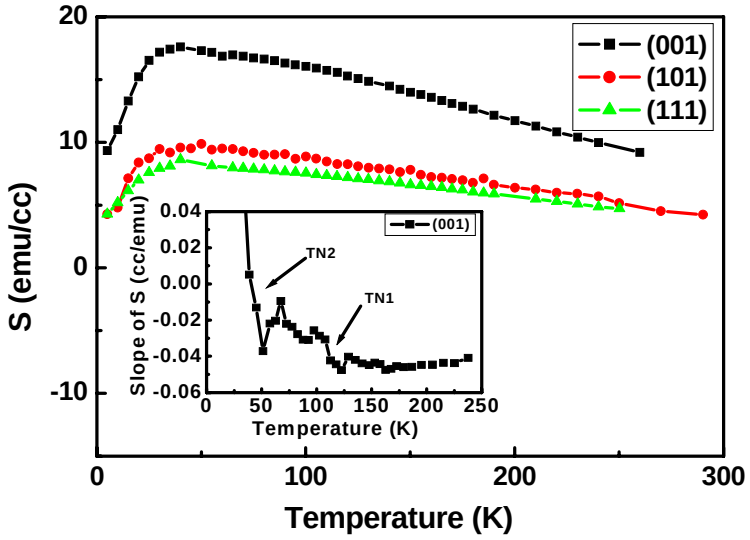

Figure 3.16 Permeability of (001), (110) and (111) oriented PFN films. The data illustrate that the permeability of (001) PFN is much higher than the other orientations. The inset shows the temperature dependence of the magnetic permeability determined from the slope.

5K, and the magnetization measured on heating under a magnetic field of $2x10^3$Oe. The temperature dependence of the slope of the magnetization (i.e. the magnetic susceptibility) is then shown as an inset in this figure. These data reveal a sequence of two magnetic phase transitions with Neel temperatures of T_{N1}≈50K and T_{N2}≈125K, and are consistent with prior investigations of PFN single crystals [15]. The results given in Figure 3.16 indicate that the phase transformational sequences of PFN thin-layers were not altered by epitaxial mismatch. However, the magnitude of the susceptibility for (001), (110) and (111) PFN thin films were 16, 9 and 8 emu/cc at 70K respectively. We can see that the susceptibility of (001) PFN was much larger than that of (110) and (111), which was induced by higher constraint stress on (001) STO substrates.

Finally, we measured the in-plane M-H response for the various films. Figure 3.17a shows data for S1: PFN (200nm)/ STO at 70K. The induced magnetization was 190μEmu for (001) PFN at a field of H=2kOe, and 110μEmu for (110) and (111) PFN. These data show that the induced magnetization is notably dependent on $\sigma_{in-plane}$: the higher the stress, the larger the magnetization. This finding is consistent with the stabilization of an AFM spin-order with a weak ferromagnetism induced by distortion of the crystal. The $\sigma_{in-plane}$ imposed by the substrate tilts the Fe-O-Fe or Fe-O-Nb-O-Fe bond angle away from 180° (which favors AFM order). The larger this tilt, the more pronounced the weak ferromagnetism becomes: which is proportional to $\cos^2\theta$ [123-126].

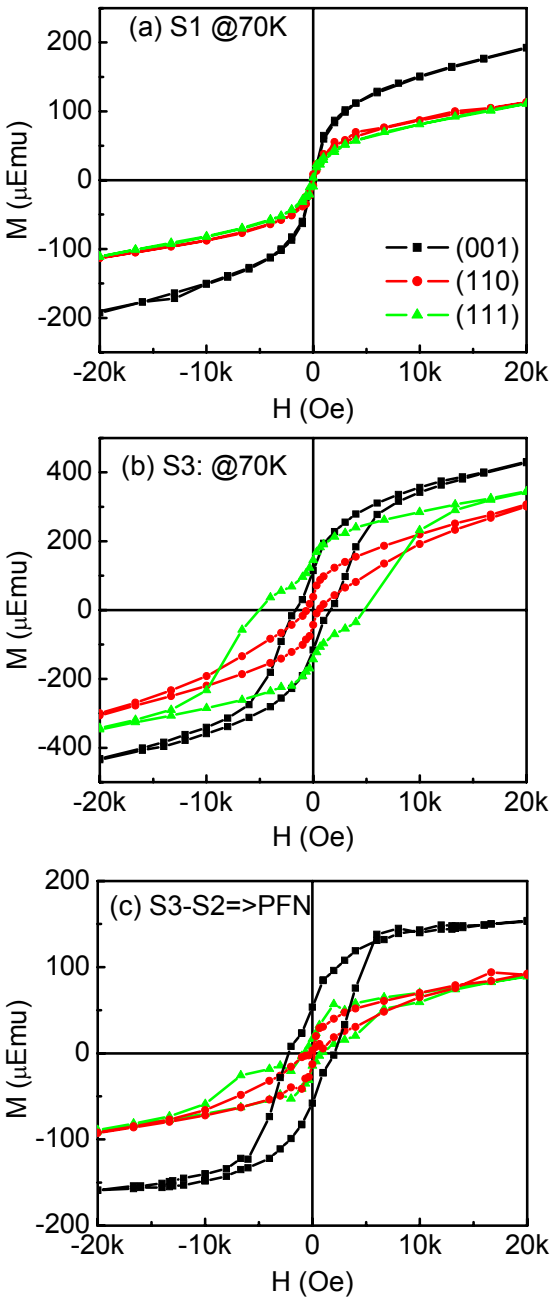

Figure 3.17 The M-H loops using a SQUID for (a) S1 (200nm PFN), (b) S3 (400nm PFN/50nm SRO) and (c) S3-S2. The data show the magnetic properties of (001), (110) and (111) oriented PFN, PFN/SRO and PFN (on top of SRO) thin films respectively.

compared with the PFN ones: i.e., they have relatively square M-H loops and high values of H_C. Accordingly, on reversal of the spin direction under field, the spin of PFN reversed at lower magnetic fields: only when $H>H_C$ did the spin direction of the SRO layer reverse. It was observed that there were two steps in the M-H curves for S3, corresponding to spin rotation in both SRO and PFN magnetic layers. By subtracting the value of the magnetization of S2 from that of S3, we attempted to estimate the value of the magnetization of the 200nm PFN layer in S3. The results are shown in Figure 3.17c. For the variously oriented films, the saturation magnetization was estimated to be 160 and 100 μEmu for (001) and (110)/(111) oriented PFN thin films respectively, which was similar to that for S1 (PFN(200nm)/STO). From these data, it can be clearly seen that the (001) layer in all cases has a larger magnetic moment with a weak ferromagnetic order. The (110) and (111) layers have much smaller in-plane constraint stress, and correspondingly the structural distortions induced in the layers are much smaller than those for (001) ones. In this case apparently, a homogeneous antiferromagnetic spin order is preferred over that with a weak ferromagnetic one. Furthermore, the value of the coercive field for S2 was H_C=2kOe, which was much larger than that for S1. This notable increase in H_C can be attributed to a spin clamping of the PFN layer by exchange coupling with the SRO buffer layer.

In summary, the effect of in-plane constraint stress has been studied for PFN epitaxial thin films grown on various oriented STO substrates. It was found that $\sigma_{in-plane}$ enhanced the piezoelectric constant, magnetic permeability and magnetization. These enhancements were strongest for (001) layers: i.e., (001)>(110)≈(111). In general, the larger $\sigma_{in-plane}$, the higher the multi-ferroic properties. We attribute these enhancements in piezoelectricity and weak ferromagnetism to distortions of the crystal structures of PFN induced by epitaxial constraint.

3.3 Low symmetry phase in $Pb(Zr_{0.52}Ti_{0.48})O_3$ epitaxial thin films with enhanced ferroelectric properties

First, a 50nm layer of $SrRuO_3$ was grown by pulsed laser deposition (PLD) on top of (001), (101) and (111) $SrTiO_3$ substrates that had been ultrasonically cleaned. These layers were grown as bottom electrodes. Then, $Pb(Zr_{0.52}Ti_{0.48})O_3$ thin films were hetero-epitaxially grown by PLD on top of $SrRuO_3/SrTiO_3$ with thicknesses between 50nm and 200nm. Films were deposited using a KrF laser (wavelength of 248nm) by a Lambda 305i, focused to a spot size of 10mm and incident on the surface of a target: using energy densities of $1.1J/cm^2$ and $1.2J/cm^2$ for $SrRuO_3$ and PZT, respectively. The distance between the substrate and target was 6cm; the base vacuum of the chamber was $<10^{-5}$Torr. During film deposition, the oxygen pressure was 150mTorr for $SrRuO_3$ and 60mTorr for PZT. The growth rates of $SrRuO_3$ and PZT were 1nm/min and 3nm/min, respectively. After deposition, a number of gold electrode pads were deposited (through a mesh) on top of the PZT film by sputtering.

The crystal structure of the films was measured using a Philips X'pert high resolution x-ray diffractometer equipped with a two bounce hybrid monochromator, an open three-circle Eulerian cradle, and a domed hot stage. The analyzer was a Ge (220) cut crystal which had a θ-resolution of 0.0068°. The x-ray unit was operated at 45kV and 40mA with wavelength of 1.5406Å ($Cu_{K\alpha}$). The reciprocal lattice unit corresponds to $a^*=2\pi/a=1.872Å^{-1}$: the mesh scans presented in this letter are all plotted in this reciprocal unit. The resistivity and ferroelectric polarization of the films was then measured using a Radiant Technology workstation and Signatone probe station.

Figure 3.18a shows XRD line scans taken over a wide 2θ range for (001), (101) and (111) oriented PZT films grown on $SrRuO_3/SrTiO_3$. The films were all epitaxial single-crystals, well crystallized as evidenced by the sharpness of the peaks ($FWHM_{(002)} \approx FWHM_{(111)} \approx 0.06\sim0.08^o$; $FWHM_{(101)} \approx 0.12°$), and each 200nm thick. Analysis then revealed that the lattice structure of (001) PZT film was tetragonal, as previously reported [127, 128]. The lattice parameter c_t was determined to be 4.132Å from the (002) scan, and a_t to be 4.044Å from the (002) and (101) ones. We next determined that the structure of (111) PZT films was rhombohedral, again as previously reported [127, 128]. The lattice parameters were determined to be a_r=4.017Å and $90°-\alpha_r=0.42^o$ by analysis of (002) and (111) peaks.

Consistent with prior studies, no evidence of a monoclinic splitting was found in either (001) or (111) PZT films. However, we found the (101) oriented PZT film to be monoclinic. Figure 3.18 also shows line scan of {200} peaks of a 200nm thick (101) film which were fit by: Part (b) a single Gaussian, and Part (c) two Gaussians. Analysis revealed notably better fittings of the peak to two Gaussians, reflecting the fact that the (101) peak was wider than the others. The corresponding lattice parameters are (c, a)=(4.098Å, 4.059Å). Figure 3.18(d) is a (102) mesh scan, which is equivalent to (100)+(002). This figure illustrates an elongation along the (H0L) direction: which consists of two $d_{(002)}$ values that are also tilted along the transverse direction with respect to each other. Although the film is thin and accordingly the two peaks are not clearly spit, two Gaussians were needed to fit the peak. A third lattice parameter b was then determined from the $(1\,\bar{1}\,\bar{1})$ and (101) peaks to be 4.049Å; in addition, an angle between the a and c axes of β_m=90.44° was calculated from $d_{(001)}$, $d_{(100)}$, $d_{(101)}$ inter-atomic spacings. This structure is monoclinic with (a_m,b_m,c_m; β_m)= (4.059Å, 4.049Å, 4.098Å; 90.44°). The fact that β_m>90°

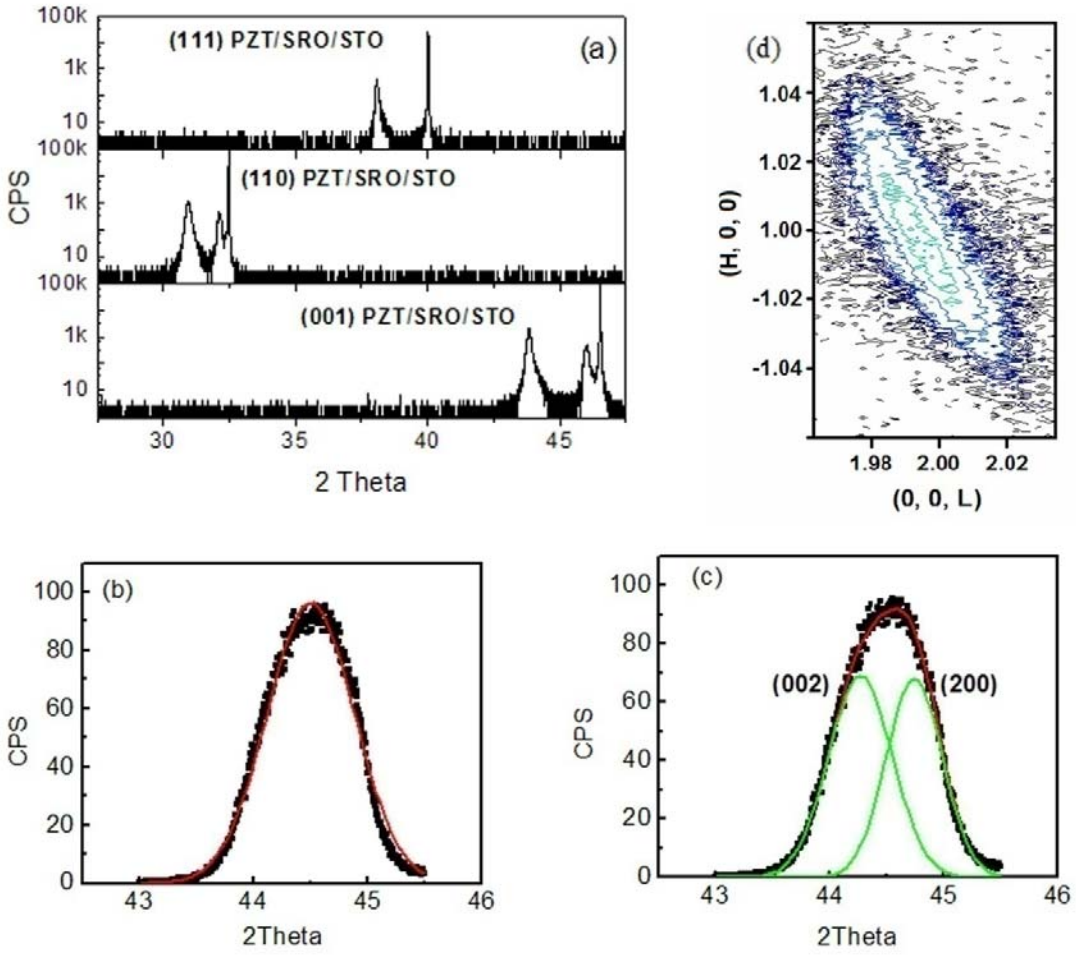

Figure 3.18 (a) X-ray line scans over a wide 2theta range for (001), (101) and (111) oriented PZT films grown on $SrRuO_3/SrTiO_3$, demonstrating that the films are single crystalline and epitaxial; and (b) line scans taken about the (002) and (200) peak of a (101) oriented PZT thin film, fit to a single Gaussian; (c) line scans taken about the (002) and (200) peak of a (101) oriented PZT thin film, fit to two Gaussians; and (d) (102) mesh scan.

shows that this monoclinic phase is of the c-type. In this case, the polarization is constrained to the (010) plane. Furthermore, since the $(1\bar{1}\bar{1})$ peak could not be fit by two or three Gaussians and that $d_{(11\bar{1})} = d_{(1\bar{1}\bar{1})}$, we can eliminate the possibility that the (101) PZT film is M_a or M_b.

The lattice mismatch (ε) between substrate and film was then calculated as $\varepsilon = \frac{a_{film} - a_{substrate}}{a_{substrate}} \times 100\%$. Along the <010>, b_m=4.0485Å, a_{SRO}=3.950Å, thus ε=2.49%; whereas along <101>, $d_{(101)}$=2.873Å, $d_{(101)SRO}$=2.793Å, and thus $\varepsilon_{(101)}$=2.85%. This demonstrates that the constraint imposed on (101) films by the substrate are larger along <101>, than <010>. In Figure 3.19, we show mesh scans taken perpendicular to the plane of (101)-oriented PZT thin films, by scanning along different directions: part (a) scattering plane is $(10\bar{1})$; and part (b) scattering plan is (010). The results clearly show that the transverse line-width measured in the (010) is much larger when the mesh scan is measured in the (010). This confirms that the film is mainly stressed (compressive) in the <101> direction, which is required to stave the M_c phase. Figure 3.19c then illustrates the effect of said constraint of PZT films grown on (101) $SrRuO_3/SrTiO_3$ substrates. The difference between the b lattice parameters of the M and T phases is (a_t-b_m)=0.005Å, whereas that of the c is (c_t-c_m)=0.035Å. Thus, for (101) films relative to (001), the compressive stress along <101> forces c_m to be shorter than c_t, enlarging β to >90^o instead and then make c_m rotate along <010> direction as shown in Figure 3.19c; furthermore, since the compressive stresses are nearly equal along <010>, $b_m \approx a_t$.

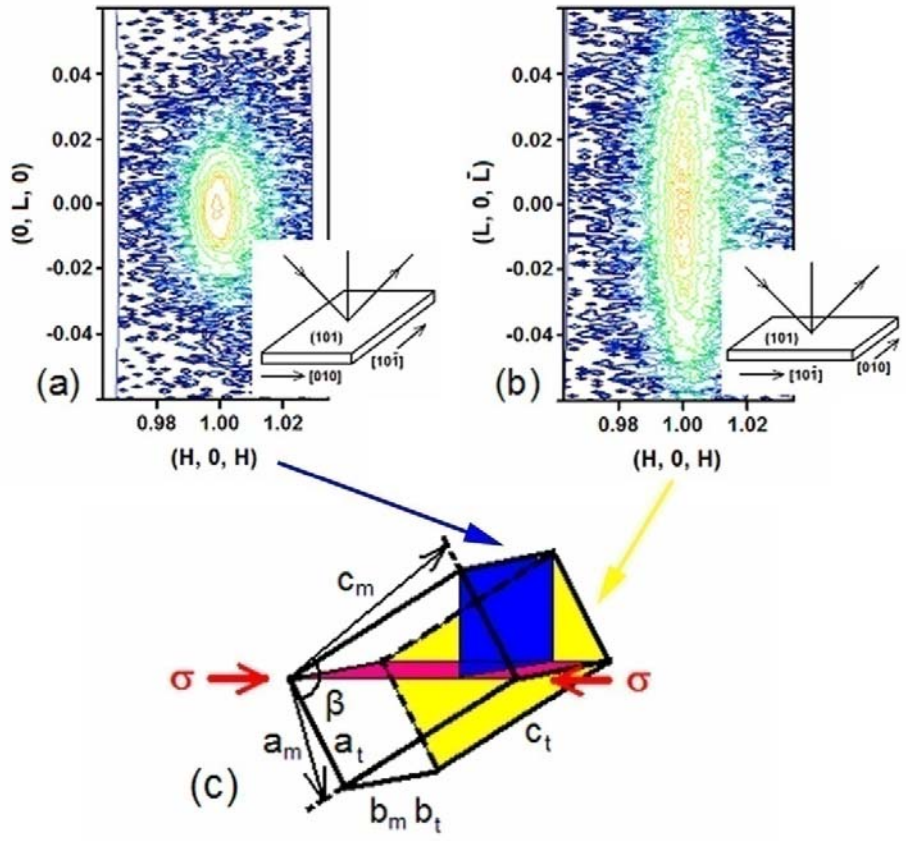

Figure 3.19 Mesh scans taken about the (101) peak of a (101) oriented PZT thin film: (a) scattering plan is (10$\bar{1}$); and part (b) scattering plan is (010); and (c) illustration of geometry of zones with respect to monoclinic distortion and orientation of in-plane compressive stress. The plane of the film is shown in pink; the (10$\bar{1}$) plane in blue; the (010) plane in yellow.

The conceptual reason for the formation of the M_c phase in (101)-oriented PZT thin films is similar to that for field-cooled (FC) $Pb(Mg_{1/3}Nb_{2/3})O_3$-xat%$PbTiO_3$ (PMN-x%PT) single crystals, where the structure can be changed from cubic to M_b or M_c in the FC condition by application of electric field (E) along [110] [76] or [001] [129] respectively. In general, the effect of epitaxy is similar to that of E//[001] – it fixes the direction of the c-axis to be close to that of an ordering force. In this M_c phase, the polarization lies in the (001) plane and rotate towards [100] with (a) increasing E for PMN-x%PT, and (b) presumably with increasing epitaxial stress for (101) PZT layers.

We next measured the ferroelectric properties of our PZT films. First, we confirmed that all of the films were highly insulating, having resistivities of $\rho \geq 10^{-10} \sim 10^{-11} \Omega \cdot cm$, which is sufficient to perform high field polarization studies. In Figure 3.30(a), we show the polarization electric field (i.e., P-E) response of (001), (101), and (111) oriented films. These data were taken using a measurement frequency of 10kHz on 200nm thick films. The data show that the saturation polarization P_s is highest for the (101) oriented film: $P_s(001)=0.9 C/m^2$, $P_s(111)=1.1 C/m^2$, and $P_s(101)=1.3 C/m^2$. These results confirm that (i) the monoclinic C phase of MPB PZT epitaxial films has the highest polarization; and (ii) for (110) epitaxial film, the polarization lies in the (0H0) plane between [110] and [001] directions. We then show in Fig. 3.20(b) that the value of P_s for the variously oriented films is nearly independent of film thickness for $50<t<200$nm; correspondingly, Figure 3.21 reveals that the lattice parameters are also independent of thickness over the same range.

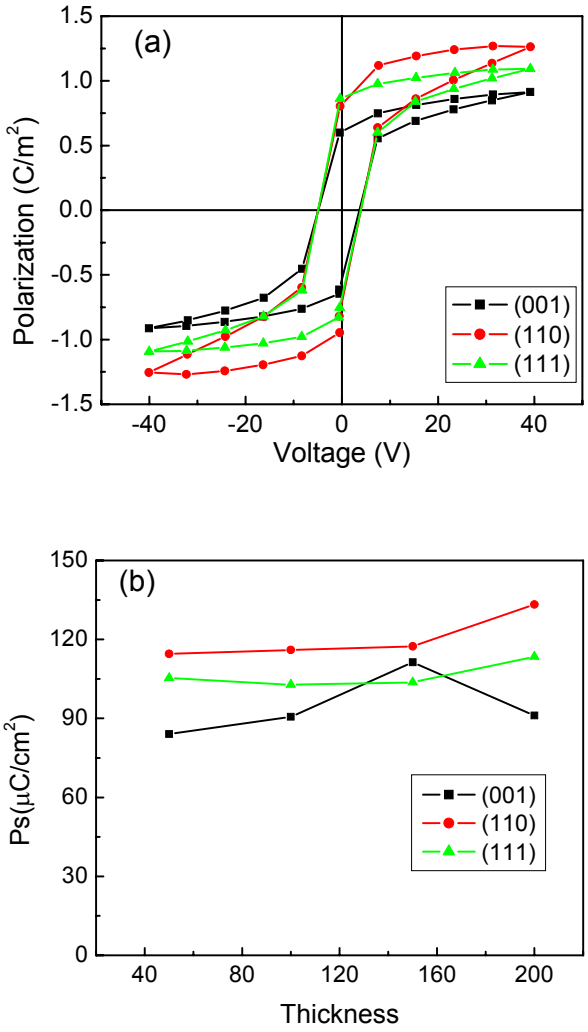

Figure 3.20 Polarization of variously oriented PZT thin films: (a) dependence of polarization on electric field (P-E); (b) dependence of saturation polarization of film thickness.

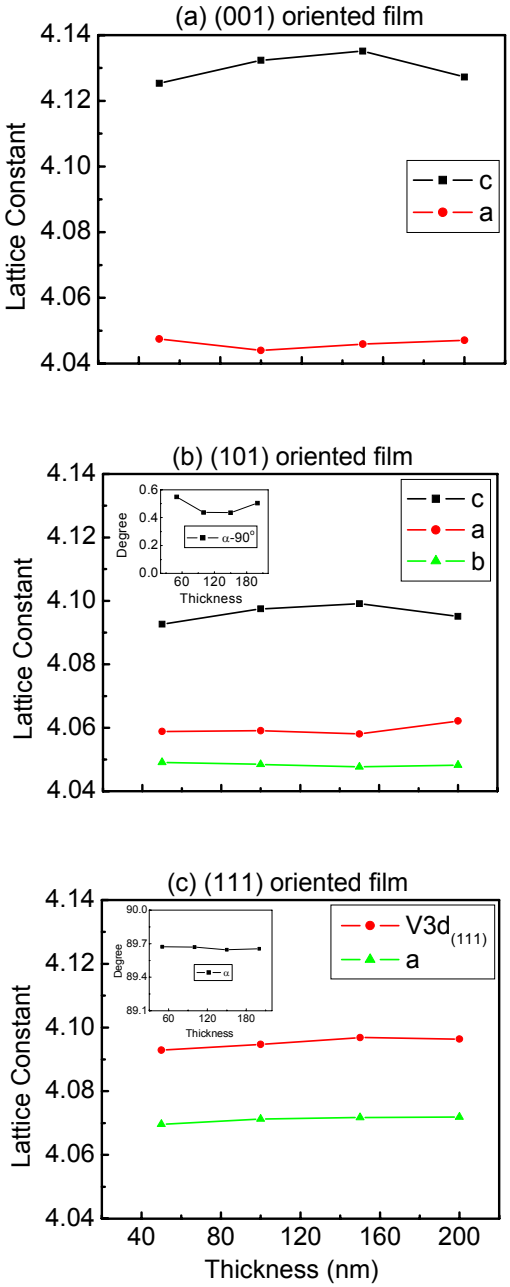

Figure 3.21 Dependence of lattice parameters on film thickness for (a) (001), (b) (101), and (c) (111) oriented PZT thin films.

In summary, we show that structure of $Pb(Zr_{0.52}Ti_{0.48})O_3$ is dependent upon the orientation of the $SrRuO_3/SrTiO_3$ substrate on which it is deposited: T for (001), R for (111), and M_c for (101). This is the report of a monoclinic phase in PZT epitaxial thin layers: it is stabilized by a compressive stress directed along <101>. We then demonstrate that the polarization is the highest when M_c is the stable phase.

3.4 Triclinic phase in tilted (001) oriented $BiFeO_3$ epitaxial thin films

Epitaxial layers of BFO were grown by pulsed laser deposition (PLD) on (100), (130), (120), (110) and (111) $SrTiO_3$ substrates that had been ultrasonically cleaned. The layers were kept to a thickness of ~40nm to prevent relaxation of the constraint stress. Films were deposited using a KrF laser (wavelength of 248nm) by a Lambda 305i: using energy densities of $1.2J/cm^2$. The distance between the substrate and target was 6cm; and the base vacuum of the chamber was $<10^{-5}$Torr. During film deposition, the oxygen pressure was 100mTorr. The crystal structure of the films was measured using a Philips X'pert high resolution x-ray diffractometer equipped with a two bounce hybrid monochromator, and an open three-circle Eulerian cradle. The analyzer was a Ge (220) cut crystal which had a θ-resolution of 0.0068°.

The lattice constants of the variously oriented $BiFeO_3$ in single unit cell representations are summarized in Table 3.2. The (111) oriented BFO thin films were rhombohedral (R) with lattice constant of a_r=3.959Å and α_r=89.48°, which was the same as bulk materials as previously reported [62-65]. For (001) and (110) BFO, $a_m=b_m\neq c_m$, and $\alpha=\gamma=90°\neq\beta$. In this case, the diagonal in the a and b plane are normal to each other in the unit cell. For (110) BFO, c<a, whereas for

Table 3.2 Lattice constant of $BiFeO_3$ thin films in single unit cell

	Phase	Angle from (100)	a (Å)	b (Å)	c (Å)	α (°)	β (°)	γ (°)
(110)	M_B in double unit cell	Tilted 45°	3.974(8)	3.974(8)	3.925(3)	89.46	89.46	89.37
(120)	Triclinic	Tilted 26°	3.955(5)	4.011(4)	3.912(5)	89.52	89.51	89.34
(130)	Triclinic	Tilted 18°	3.926(5)	4.041(9)	3.909(3)	89.52	89.51	89.30
(100)	M_A in double unit cell	Tilted 0°	3.903(4)	3.903(4)	4.075(6)	89.53	89.53	89.53
(111)	Rhombohedral	-	3.959(2)	3.959(2)	3.959(2)	89.48	89.48	89.48

(001) c>a. As a consequence, the stable structures are M_B and M_A respectively, with lattice constant of ($a_M/\sqrt{2}$ =3.996(7)Å, $b_M/\sqrt{2}$ =3.952(8)Å, c_M=3.925(3)Å, β=89.24°) and ($a_M/\sqrt{2}$ =3.919(5)Å, $b_M/\sqrt{2}$ =3.887(2)Å, c_M=4.075(6)Å, β=89.34°) in a double unit cell representation.

However, a triclinic phase was found for (130) and (120) oriented BFO thin films, which were 26° and 18° titled from the (100). Because BFO is not Tetragonal (T), Orthorhombic (O) or Rhombohedral (R), we must use a parallelogram model to perform calculations to determine the lattice constants and crystal structure. First, we calculated the grey plane in Figure 3.22a, which is normal to the substrate, as circled by the blue dashed plane in the figure. From the distances b", m' and n' that we measured directly, we can calculate a', b', t and all angles in this plane (see Figure 3.22b). Next, we calculated the grey plane in Figures 3.22c and 3.22d. From p and q that were directly measured, and n which was calculated above, we can determine c and r. Accordingly, all the lattice constants and angles have been so determined. All the original XRD peaks used in the calculation are shown in Figure 3.22e to 3.22f. We then used these lattice constants to build a model, from which we can predict the lattice constants independently of the first step above. By comparing all the predicted values to those that were directly measured, we found a convergence of values. For example, the predicted values of the inter-planar spacings $d_{(111)}$ and $d_{(010)}$ were 6.832(4)Å and 3.955(1)Å for the (120) films, whereas the measured values were 6.831(5)Å and 3.954(3)Å: a difference of only 0.01% and 0.02% for $d_{(111)}$ and $d_{(010)}$ between prediction and measurement. The triclinic lattice parameters of (120) and (130) BFO films were (a_t, b_t, c_t; α_t, β_t, γ_t)=(3.955(5)Å, 4.011(4)Å, 3.912(5)Å, 89.52°, 89.51°, 89.34°) and (a_t, b_t, c_t; α_t, β_t, γ_t)=(3.926(5)Å, 4.041(9)Å, 3.909(3)Å, 89.52°, 89.51°, 89.30°) respectively. The

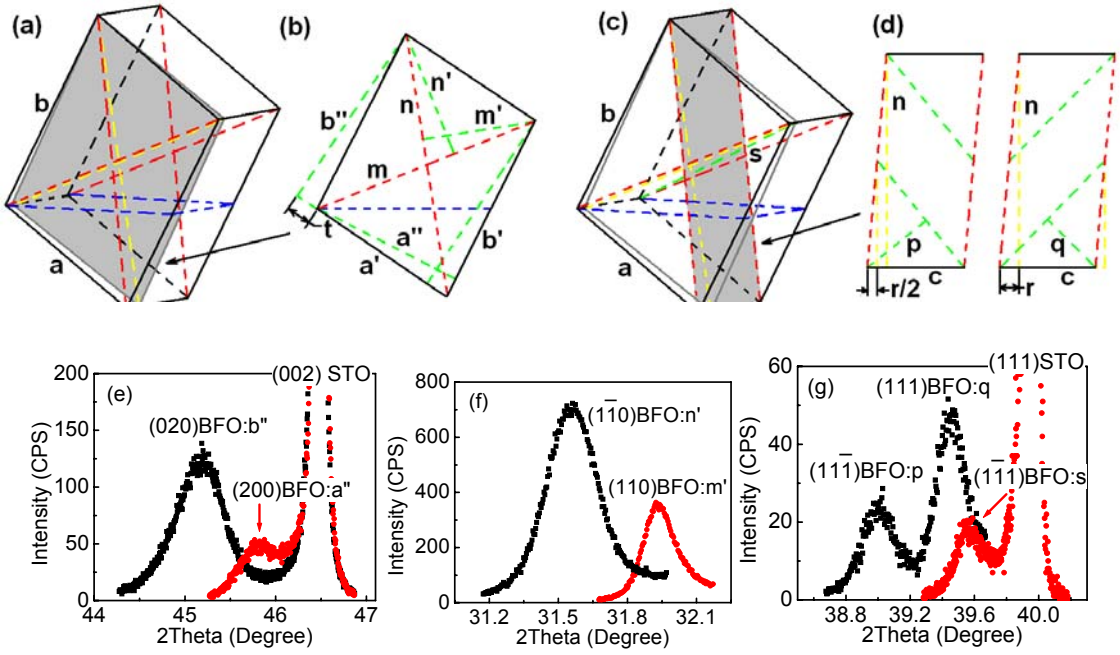

Figure 3.22 (a)~(d) Illustration of the planes in the unit cell which were used to calculate the triclinic lattice constants and tilt angles for $BiFeO_3$. (e)~(f) X-ray results of BFO peaks which are used in the calculation.

(130) and (120) BFO films can only be described as a single cell triclinic structure, which can not fit to any higher symmetry multi-cell structural representation.

The (100), (130), (120) and (110) oriented BFO films were deposited on STO single crystal substrates, which were 0°, 18°, 26° and 45° titled from the (100) plane. Figure 3.23 shows the lattice parameters of these various oriented BFO layers as a function of the tilt angle from the (100) towards the (110). The blue dashed line represents the lattice constant of the STO substrate, which was a_c=3.90Å. The lattice parameters from left to right are for (100), (130), (120) and (110) oriented BFO films. The angles between the lattice and substrate are marked in bold on top of the points. As the angle between the lattice and substrate was increased from 0° (in-plane) to 45° (out-of-plane), the lattice parameters of BFO increased gradually from 3.90Å to 3.97Å; whereas the c lattice parameter decreased from 4.08Å to 3.97Å. The relationship between the tilt and the BFO lattice parameters are nearly linear, indicating that elastic constraint is an important factor. With increasing tilt, the in-plane lattice parameters gradually increased as the compressive stress was increased, whereas the out-of-plane parameter gradually decreased.

In addition, we found when the substrate was changed from (100) to (110), that the in-plane lattice constants were also slightly increased with respect to those out-of-plane: from 3.90Å to 3.92Å. The cause for this is the anisotropic nature of the constraint stress along the in-plane directions. For (100) BFO films, the compressive stress from the substrate was isotropic. However, for (130), (120) and (110) BFO films, the in-plane compressive stress becomes increasingly anisotropic with increasing tilt angle away from the (001). In the case of (110), the compressive stress along the <0 0 1> is lower than that along <1 $\bar{1}$ 0>: this makes the lattice parameter for (110) layers larger than that of (001).

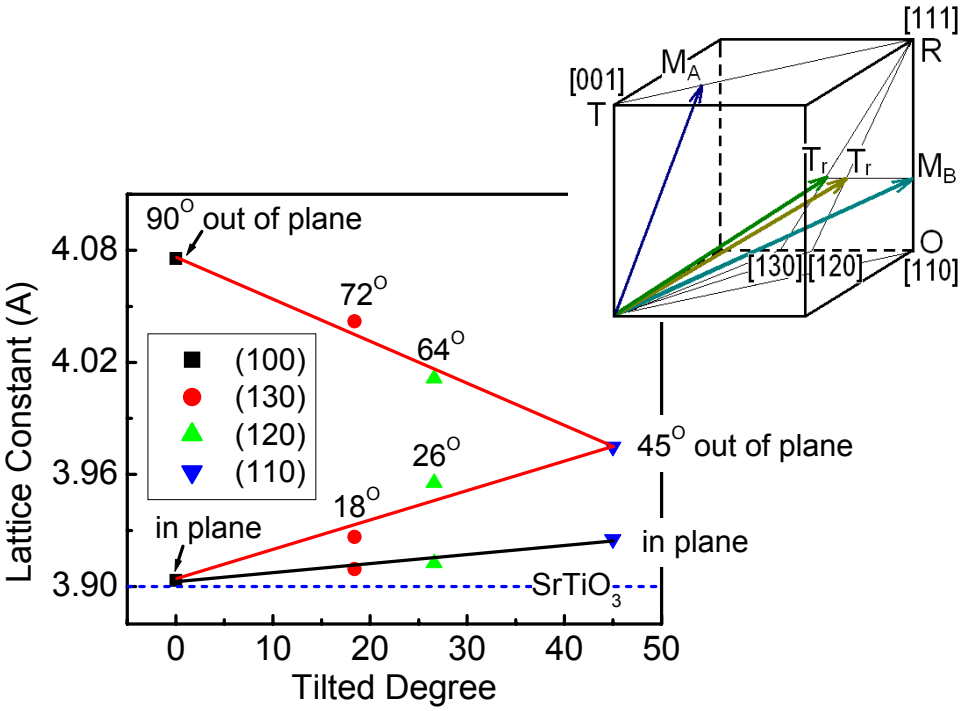

Figure 3.23 Lattice constants of (100), (130), (120) and (110) oriented $BiFeO_3$ thin films as a function of tilt angle, demonstrating the relationship between the lattice constants of $BiFeO_3$ and the angle between the film and substrate. Insert shows that M_A, triclinic, triclinic and M_B are the results of the combination of the constraint stress from the (100), (130), (120) and (110) substrates and the stable R phase of BFO respectively.

The insert of Figure 3.23 can be used to explain the formation of structurally bridging triclinic and monoclinic phases in BFO films. Bulk BFO has a rhombohedral structure which is distorted from cubic along the [111]. Epitaxial stress applied by the substrate along [100], [110], [120] and [130] tends to compress the epitaxial thin films to T, O, M_A and M_C structures, respectively. The combination of the constraint stress from the substrate and the stable R phase of BFO results in net symmetries of M_A, M_B, triclinic and triclinic, respectively. Using the understanding of our approach, we can predict/design crystal structures for other oriented epitaxial films. For example, if a R phase is deposited on (110), (113), (112), (223), (111) and (221) oriented substrates, a stable M_B structure can be expected, where the lattice parameter c_m will increase gradually on going from (110), (113), (112) to (223) orientations. However, (111) films will remain R with c=a=b; and (221) layers will be M_A with $c_m > a_m = b_m$.

In summary, we report a method by which to epitaxial engineer low symmetry phases in ferroelectric perovskites: the selection of tilted (001) single crystal substrates. Using this approach, we have developed triclinic BFO layers grown on (130) and (120) STO substrates, that structurally bridge M_A and M_B monoclinic phases, where the lattice parameters can be varied from 3.90Å to 4.08Å.

3.5 Summary

By selecting the orientation of substrates, it is possible to change the crystal structures and lattice constants of ferroelectric thin films of PZT, PFN and BFO. This is due to strong in-plane compressive constraint stresses between the epitaxial thin film and the single crystal substrate. The constraint stress can (i) alter the phase stability even when the composition is crossed over the original MPB of bulk PZT; (ii) enhance the phase stability to temperatures

notably lower than the corresponding bulk PFN; and (iii) stabilize low symmetry monoclinic and triclinic structures which are non-existent in bulk BFO. Our findings show that off-axis substrates can be used to engineer bridging phases of the lowest possible symmetry. Such low symmetry phases may be important to enhancing piezoelectric properties. In particular, for magnetoelectric composites, the ability to tune the symmetry of the matrix of the piezoelectric coefficients offers an important approach to control product tensor properties.

Chapter 4: Two phase epitaxial thin films – Epitaxial engineering of morphological stability

Magnetoelectricity is a physical property that results from an exchange between polar and spin subsystem: i.e., a change in polarization (P) with application of magnetic field (H), or a change in magnetization (M) with applied electric field (E) [1, 2]. Magnetoelectric (ME) properties have been reported in ferroelectric-ferromagnetic two-phase composite systems, consisting of piezoelectric and magnetostrictive phases [8-10, 16, 130-131]. These two phases are elastically coupled to each other at the interfaces through their strictions. Scientific interest in the physical properties of these composites, in addition to great potential for applications (as actuators, switches, magnetic field sensors or new types of electronic memory devices), has resulted in magetoelectric materials receiving significant research interests during recent years, especially as thin films [26].

4.1 Introduction

Magnetoelectric (ME) materials exhibit an induced polarization under external magnetic field H, or an induced magnetization under external electric field E. The concept of magnetoelectricity was original proposed by Curie in 1894[1]. It was first experimentally found in the single phase material Cr_2O_3: where the H-induced polarization and E-induced magnetization were separately reported by Astrov in 1960[2-3] and Rado et al. in 1961[4]. Compared with single phase multiferroic material, composite multiferroic materials have higher ME effects [8-10, 130-131]. Through a strictive interaction between the piezoelectricity of the

ferroelectric phase and the magnetostriction of the ferromagnetic phase, said composites are capable of producing relative large ME coefficients.

The most widely studied phase connectivities for two-phase ME composite films are (i) a (2-2) layer-by-layer structure [86-87, 91-92, 132-135], and (ii) a (0-3) structure of 2nd phase particles embedded in a primary matrix phase [88-90, 136-137]. In addition, (1-3) self-assembled ME composite thin films - ferroelectric (or ferromagnetic) nano-pillar embedded in ferromagnetic (or ferroelectric) matrix - was first reported in 2004 [26]. Self-assembled epitaxial $BiFeO_3$-$CoFe_2O_4$ (BFO-CFO) nano-composite thin films deposited on differently oriented substrates are known to have different types of nano-structures [79]: on (001) $SrTiO_3$ (STO) substrates, BFO pyramidal nano-pillars are embedded in a CFO matrix; on (111) STO, CFO triangular nano-pillars are embedded in a BFO matrix; and on (110) CFO, a nano-ridge is embedded in BFO matrix. Which phase spreads as the matrix versus which one is spatially continued to become nano-pillars depends on wetting conditions between film and substrate: for example, CFO wets well on (111) STO, but not on (001) [78]. Although it is predicted that (1-3) self-assembled multiferroic composite thin films should have better ME coupling because of reduced constraint between nano-pillars and substrate [96], it is difficult to deposit such nano-structures with satisfactory ferroelectric properties. Accordingly, reports of multi-ferroic properties of self-assembled nano-composite have been quite limited, in particular compared with layer-by-layer and particle-matrix composite structures.

Here, we report the nano-structural, ferroelectric (FE), ferromagnetic (FM) and ME properties of self-assembled epitaxial BFO-CFO nano-composite thin film deposited on variously orientated substrates. CFO nano-belts are found in both BFO-CFO and BTO-CFO system. It is found that the ferroelectric and ferromagnetic properties of the nano-composite are

strongly related to the orientations of the BFO phase and the nano-structure of the CFO phase, respectively; whereas the ME properties depend not only on the FE and FM properties of each individual phase, but also on how the nano-structures couples them together.

4.2 Nano-structures of self-assembled nano-composite thin films

4.2.1 Background

Zheng et al. [26] were the first to report self-assembled ferroelectric-ferromagnetic (1-3) nano-composite thin films: where CFO formed as nano-pillars embedded in a BTO matrix. After that, in order to understand the growth mechanism and improve the multi-ferroelectric properties, numerous investigations of similar systems were reported: such as those with different perovskite (BTO, BFO, $PbTiO_3$ (PTO) and PZT) and spinel (CFO and NFO) phases, different spinel/perovskite or S/P atomic ratios (1/2, 1/1 and 2/1), different substrates with different lattice parameters ($LaAlO_3$: 3.79Å, $SrTiO_3$: 3.90Å, $MgAl_2O_4$: 8.08Å and MgO: 4.21Å), different substrate orientations ((001), (110) and (111)), and different film thicknesses [78-85, 138-142].

For all material couples, of all S/P ratios and substrates, it was found that epitaxial films had a (1-3) phase connectivity at the nm-level when deposited on the (001) orientation: spinel formed nano-pillars that were vertical to the substrate and that were embedded in a perovskite matrix; and in a (3-1) connectivity when deposited on the (111) orientation, where spinel was the matrix phase that was embedded with perovskite nano-pillars. However, for the (110) orientation, the nano-structures were more complicated: spinel changed from a nano-pillar to a nano-maze structure [138]. Zheng et al. [78] found that the reason was that perovskite wets better than spinel

on (001) substrates, and that spinel wets better than perovskite on (111) substrates. However, wetting could not explain why spinel prefered to form as nano-pillars on (001) spinel $MgAl_2O_4$ substrates, or on CFO buffer-layers. Also it could not explain the complicated nano-structure found when deposited on (110) substrates. Slutsker et al. [83, 85, 138, 143-144] gave an explanation based on elastic interactions: by considering each phase as an elastic domain that is under a constraint stress imposed by the substrate. Following this elastic model, not only could the (1-3) and (3-1) nano-structures on (001) and (111) substrates be explained, but also more complicated phase connectivities on (110) substrates could be too.

In the BFO-CFO system, Zheng et al. [79] used Wulff-net shapes to explain why the CFO phase formed with pyramidal structures that were embedded in a flat BFO matrix, both deposited on (001) oriented substrates. Correspondingly, BFO formed as triangular pyramids embedded in a flat CFO matrix on (111) substrates. In this case, CFO is an octahedron with eight {111} faces, and BFO is a cube with six {001} ones: this is because the (111) face of CFO and (001) face of BFO have the lowest surface energies.

In addition to phase connectivities and crystal structures, another important factor may also influence the nano-structure of the composite thin film: that is CFO tends to elongate along the [110] direction due to a ledge growth mechanism [145]. Our research group has found CFO nano-belts in both the BTO-CFO and BFO-CFO systems [146-147].

4.2.2 Nano-belts in $BiFeO_3$-$CoFe_2O_4$ composite thin films

We show in Figure 4.1 scanning force microscopy images of a $BiFeO_3$-$CoFe_2O_4$ (BFO-CFO) composite epitaxial thin film grown on a (110) $SrTiO_3$ substrate. Part (a) of this figure

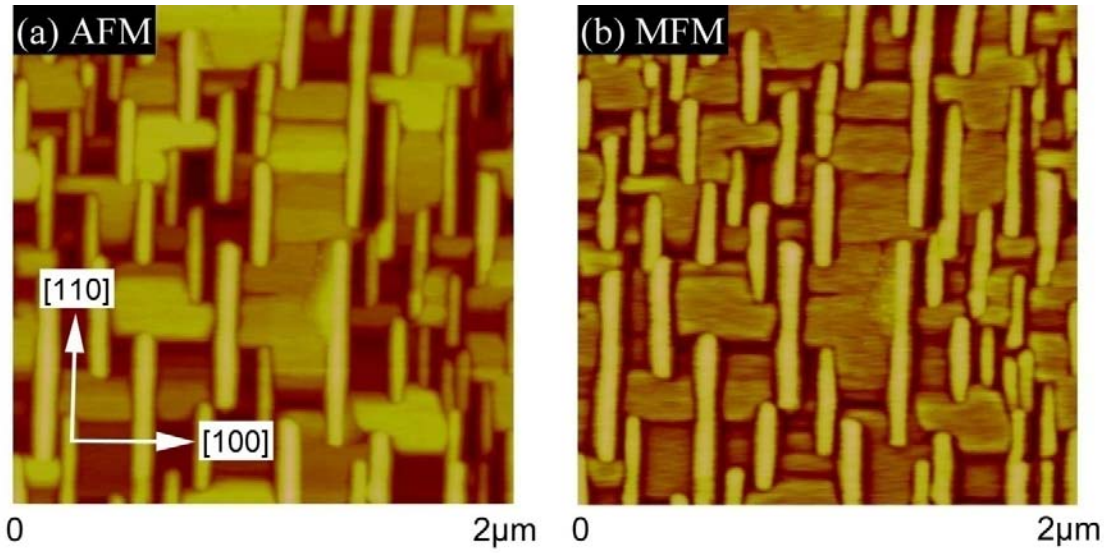

Figure 4.1 (a) AFM and (b) MFM results of (110) $BiFeO_3$-$CoFe_2O_4$ nano-composite, demonstrating an elongation of the $CoFe_2O_4$ phase regions along the <110> direction.

provides an atomic force microscopy (AFM) image that demonstrates the presence of what we designate as a 'nano-belt structure'. The topography is CFO nano-belts that are embedded in a BFO matrix. The CFO nano-belts are elongated along the [110] direction (which is epitaxial to that of BFO), and are notably shorter along the [100] direction. The top edge of the nano-belts is a [110] edge along their entire length, where the sides of this edge are {111} faces. In Part (b) of this figure, we show a magnetic force microscopy (MFM) images of the same BFO-CFO epitaxial film grown on (110) $SrTiO_3$, which were taken on the same region of the films as that of the AFM image. This MFM image clearly illustrates a magnetization contrast of the same size and shape as that found in the AFM one. It demonstrates that the magnetic CFO phase is the 2nd phase having the nano-belt morphology that is elongated along <110>. In order to understand the large asymmetry between width along [100] and length along [110] of the nano-belts, we studied the kinetics of nucleation and crystallization of the nano-composite films in details.

To understand the kinetics of crystallization in detail, $BiFeO_3$-$CoFe_2O_4$ composite thin films were deposited on $SrTiO_3$ substrates over a temperature range from 790K to 1020K. The diffusion coefficient D is simply given as $D = D_0 \cdot e^{\frac{-E_A}{R \cdot T}}$: where D_0 is the attempt coefficient of diffusion, E_A the activation barrier to diffusion, R the Boltzmann's constant, and T the absolute temperature. In order to more clearly observe the process of nucleation and crystallization, it is necessary to decrease the kinetics of the diffusion process, simply by decreasing T. However, the deposition temperature should not be reduced too much, otherwise the diffusion kinetics will lie outside that required for formation and growth of the nano-structure. For our BFO-CFO thin films, the temperature range of 790K to 1020K was found to be within this allowable window: we established this by x-ray diffraction (XRD), which revealed a single (n n 0) peak for $BiFeO_3$, $CoFe_2O_4$, and $SrTiO_3$ at each temperature that we studied in this range. The XRD results of

BFO-CFO nano-composite thin films deposited at different temperatures from 790K to 1020K are shown in Figure 4.2. We can see that at 790K, the BFO and CFO peaks are very weak: this temperature is near a threshold for crystallization. The BFO and CFO peaks at 810K are still not very intense, although crystallization of both phases is evident. However, above 870K, strong BFO and CFO peaks were clearly evident, as can be seen in the figure.

In Figure 4.3, we show the evolution of the nano-structure of $BiFeO_3$-$CoFe_2O_4$ composite thin films deposited on (110) $SrTiO_3$ for various deposition temperatures. The images in these figures were taken using the AFM mode of a scanning force microscope. Part (a) of Figure 4.3 shows an image taken from the film deposited at 790K. In this figure, we found that the thin film was full of perovskite rods aligned along the [100] direction, consistent with a Winterbottom construction as reported previously by Zheng et al [79]. These results demonstrate at lower deposition temperatures (and subsequently smaller diffusion coefficients D) that the perovskite phase is the first to nucleate and grow on (110) oriented $SrTiO_3$ substrates.

When the deposition temperature was increased to 810K, tiny spinel spots were observed to form on the edges of the perovskite rods, as shown in Figure 4.3b. With increasing deposition temperature to 870K (see Fig. 4.3c), the spinel regions grew larger and longer. With further increment to 930K, the spinel phase continued to grow and elongated along the [110] direction forming rod-shaped structures, whereas the perovskite rods became increasingly diffused together. Finally, on increasing the deposition temperature to 1010K (Fig. 4.3e), the perovskite phase regions became nearly indistinguishable, forming a near continuous matrix. In addition, the spinel rods became much longer and formed what we designate as the ‘nano-belt structure’. This CFO nano-belt structure was embedded in the BFO matrix.

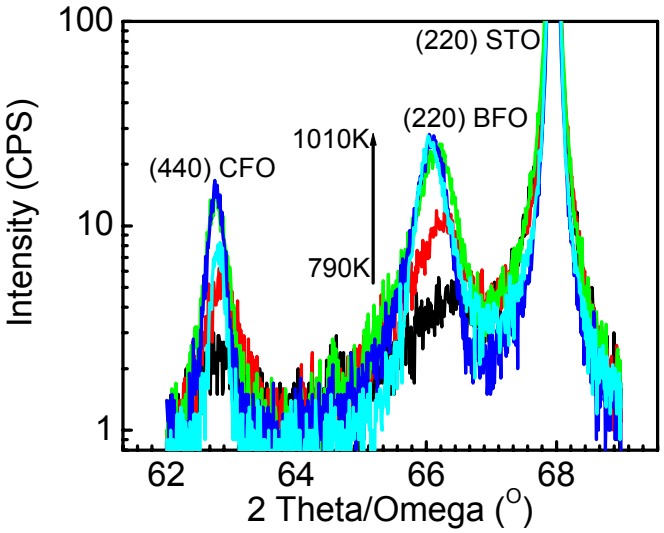

Figure 4.2 XRD results of $BiFeO_3$-$CoFe_2O_4$ nano-composite thin films deposited at 790K, 810K, 870K, 930K and 1010K. The results demonstrate the epitaxial structure in the temperature window.

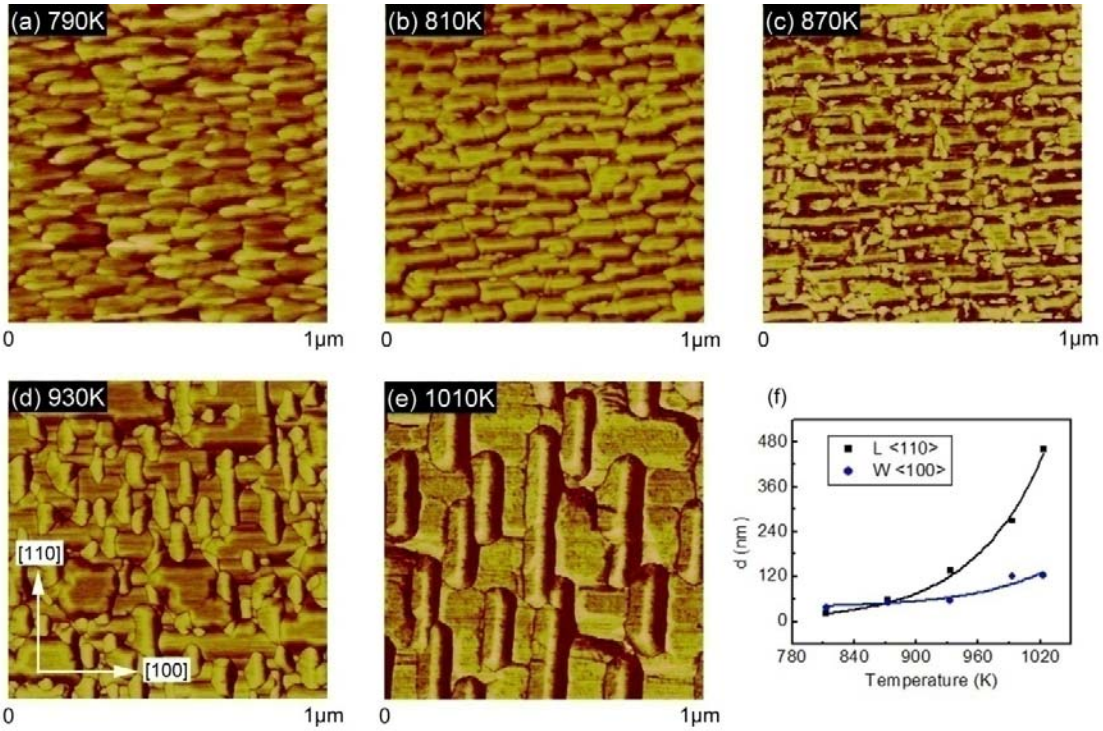

Figure 4.3 AFM results of $BiFeO_3$-$CoFe_2O_4$ nano-composite thin films deposited at (a) 790K, (b) 810K, (c) 870K, (d) 930K and (e) 1010K respectively. The results demonstrate the evolution of the nano-structures with temperature. Part (f) illustrates the average size of the $CoFe_2O_4$ nano-belts as function of deposition temperature.

These images show that the mechanism of formation of the nanostructure occurs (i) first by formation of the perovskite phase, and (ii) then by subsequent segregation of spinel from the pervovskite on thermal treatment. With increasing temperature (and accordingly diffusion rate), the spinel phase regions grow larger and elongate along the easy [110] direction of the perovskite phase. All of these results point to one underlying consideration: why the spinel phase prefers to grow along the [110] direction in the perovskite matrix.

In Figure 4.3f, we show the average length (L) and width (W) of the spinel phase regions in the BFO-CFO thin layer as a function of deposition temperature. These averages were taken by analysis of 10 spinel regions. Small spinel regions or 'spots' of sizes L=W=10-20nm were first found on the edges of perovskite phase rods at 810K. With increase of temperature to 870K, the average size of the spinel phase regions increased only slightly to L=W=20-30nm. However, on heating to 930K, the length of the spinel phase along the [110] direction increased much more prominently than that of the width along the [100] direction: L=130nm and W=30-40nm. This anisotropy of the spinel phase regions reflects the predominance of a nano-belt morphology. With increasing temperature to 1020K, the average length of the CFO nano-belts increased to L≈0.5μm, with a width of W≈0.1μm. In fact, we observed (not shown) some nano-belts as long as 1~2μm. These data clearly demonstrate that CFO nano-structure growth is anisotropic and prefers to elongate along the [110] direction relative to the [100].

Next, we investigated the effect of substrate orientation on the nanostructure of $BiFeO_3$-$CoFe_2O_4$ composite thin films. We deposited films on (100), (130), (120), and (110) $SrTiO_3$ substrates: which were 0º, 18º, 26º and 45º tilted away from the (100) orientation, respectively. Figures 4.4a-d show AFM images of films grown on these various substrate orientations, again

respectively. In each figure (right hand side), we also illustrate a line scan taken across the image: the inset shows the area from which the line scan was extracted.

Figure 4.4a shows an AFM image taken from a BFO-CFO film grown on a (100) substrate. In this case, CFO nano-rods were observed, whose morphology and size are analogous to that originally reported by Zheng et al. [26] for CFO nano-rods in a BTO matrix. By analysis of the line scans taken across the image, we determined that the nanostructure was actually CFO nano-pyramids embedded in a BFO matrix: we determined four {111} faces that were 90º rotated from each other and four [110] edges on every CFO region we analyzed. The Winterbottom construction for this CFO nano-pyramid is illustrated in the inset above the AFM image.

Figures 4.4b and c show AFM images taken from BFO-CFO films grown on (130) and (120) substrates respectively. Similar to the films grown on (100), the images from these other two orientations also revealed CFO nano-pyramids embedded in a BFO matrix. However, these pyramids were tilted by 18º and 26º for films grown on (130) and (120) $SrTiO_3$ substrates, respectively. Analysis of the corresponding line scans in these figures revealed that the angle α between {111} faces was 103º and 106º respectively for (130) and (120) oriented films. Winterbottom constructions are illustrated in the inset above the AFM images in both figures.

Finally, Figure 4.4d shows an AFM image taken from a BFO-CFO film grown on a (110) substrate, which is similar to the image shown in Figure 4.3e. Analysis of the line scan taken from this image illustrates that α=110º. In this case, nano-belts have a ridge along the [110]. It is interesting that spinel nano-structures with [110] ridges tend to become quite long in length. In

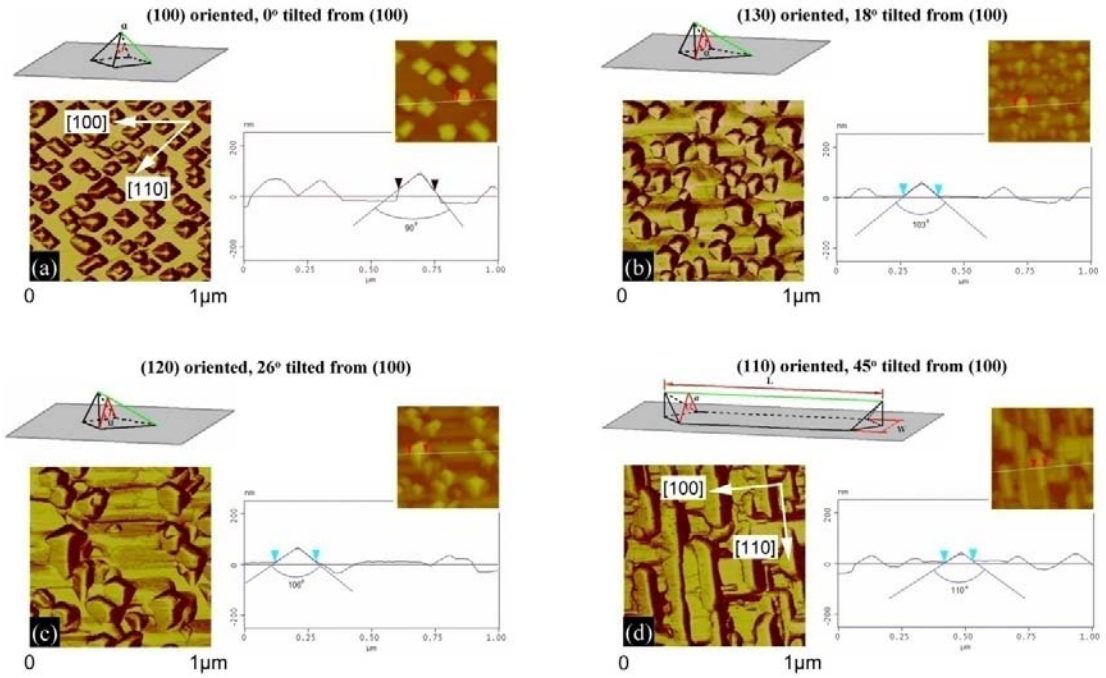

Figure 4.4 AFM results of $BiFeO_3$-$CoFe_2O_4$ nano-composite thin films deposited on (a) (100), (b) (130), (c) (120) and (d) (110) oriented $SrTiO_3$ substrates. The images illustrate the elongation of <110> ridges of $CoFe_2O_4$ nano-belts. Winterbottom constructions are in the inset above the AFM images; and analyses of cross sections are given to the right of the AFM images.

the case of films grown on substrate that are 0º, 18º, to 26º titled from the (100) orientations, [110] spinel ridges tend to form but are always truncated by translating into perovskite phase regions. However, for the (110) orientation, the [110] spinel ridges are free to extend indefinitely. This results in what we designate as the spinel nano-belt morphology.

A natural question to ask is what causes the shape anisotropy of the CFO regions? The CFO spinel phase was cubic with lattice constant of a_c=8.380±0.002Å for all of our oriented nano-composite thin films, and the STO substrate was also cubic with lattice constant of a_c=3.905Å. It should be noted that the mismatch between the CFO film and STO substrate is quite large: $\frac{0.5a_{CFO} - a_{STO}}{a_{STO}} x100\% = 7.3\%$, which is nearly out of the range for epitaxial strain that can be accommodated in hetero-structures. Since both phases are cubic, the reason for elongation (L/W=5 at 1010K) of the CFO morphology along the [110] can not be an in-plane anisotropy of the elastic constraint between substrate and film. Furthermore, the diffusion coefficient is a second rank polar tensor, which for a cubic crystal system reduces to a scalar (i.e., isotropic): thus, there should be no preferred growth direction of spinel CFO regions in the BFO matrix. Finally, although Winterbottom constructions can successfully explain the {111} facets and [110] edges in the CFO nano-structure, surface energy and wetting considerations can not explain the [110] elongation of the CFO morphology. So, one is left wondering what is the cause of the large aspect ratio for the CFO regions.

A possible reason for the anisotropic growth of the CFO phase along [110] may be a ledge growth mechanism. As pointed out by Porter and Easterling, ledges can heterogeneously nucleate at the point of contact with another phase [148]. In this case, atoms will be able to move more easily across the ledges, than along the immobile facets of single crystals during interface

migration. The existence of growth ledges has been manifested by many studies of solid/solid and solid/vapor interfaces. Yanina [145] reported that spinel single crystals tend to grow or etch anisotropically along the [110]. For thin films or surfaces of single crystals, ledge growth is an important mechanism that has lower activation energy and that tends to result in smoother surfaces than random island growth. Yanina [145] also found that due to the special distribution of cations in spinel, which are along the [110] direction, that ledge growth of spinel tended to occur preferentially along the [110]. Our findings of anisotropic growth of spinel CFO regions along [110] in BTO-CFO nano-composites are consistent with these prior ones, indicating the importance of an anisotropic ledge growth mechanism in perovskite-spinel nano-composite thin films.

In summary, we have found anisotropic growth of spinel phase along [110] of the spinel phase in two-phase perovskite-spinel ($BiFeO_3$-$CoFe_2O_4$) nano-composite epitaxial thin films deposited on (110) $SrTiO_3$ by pulsed laser deposition, which we attribute to an anisotropic ledge growth mechanism. Investigations of the mechanism of nanostructure formation from 790K to 1010K revealed that (i) the first step was growth of perovskite on (110) $SrTiO_3$; (ii) the second step was segregation of the spinel out of the perovskite; and (iii) the third step was evolution of spinel nano-belts that were oriented along the [110]. We also studied the spinel nano-structures for various substrate orientations: (100), (130), (120) and (110). Using Winterbottom constructions, we show the importance of the [110] direction in spinel phase formation, in addition to temperature, on the length of the spinel nano-belts.

4.2.3 Nano-belts in $BaTiO_3$-$CoFe_2O_4$ composite thin films

A. Nano-structure of the (001) oriented BTO-CFO composite thin films.

An AFM image of the nano-structure of a (001) oriented BTO-CFO film directly deposited on STO substrate and annealed at 1330K is shown in Figure 4.5. The CFO phase was distributed as nano-belts within a BTO matrix. Previously, for (001) oriented BTO-CFO, Zheng et al [26] reported that the CFO phase grew as nano-pillars along the out-of-plane direction which were embedded in a BTO matrix. However, in our investigation, we found that CFO grew as nano-belts elongated along the in-plane [110] direction. The average length (L) of the CFO nano-belts was around 700nm and the average width (W) was about 80nm, with L/W=9. Each CFO nano-belt was anisotropic along the [110] and $[1\bar{1}0]$ directions, where the length was elongated along either [110] or $[1\bar{1}0]$. We found no preference for elongation along [110] over $[1\bar{1}0]$ directions: they both occurred with near equal probability.

B. Evolution of BTO-CFO nano-structures with annealing temperature:

In Figure 4.6, we show the evolution of the nano-structure of BTO-CFO composite thin films deposited on (001) $SrTiO_3$ for various annealing temperatures. The images in these figures were taken using the AFM mode of a scanning force microscope. Part (a) shows an image taken from the sample annealed at 1170K. In this figure, we can see that the film is full of CFO nano-pillars, where some have aggregated into a few larger crystallites. The top view of the CFO nano-rods has a pyramidal-like morphology, consistent with Winterbottom constructions as previously reported [79].

When the annealing temperature was increased to 1210K, the area of the larger crystallites was increased at the expense of the number of nano-rods, where spinel nano-rods were found to persist on the edges of the large crystallites, as shown in Figure 4.6b. With

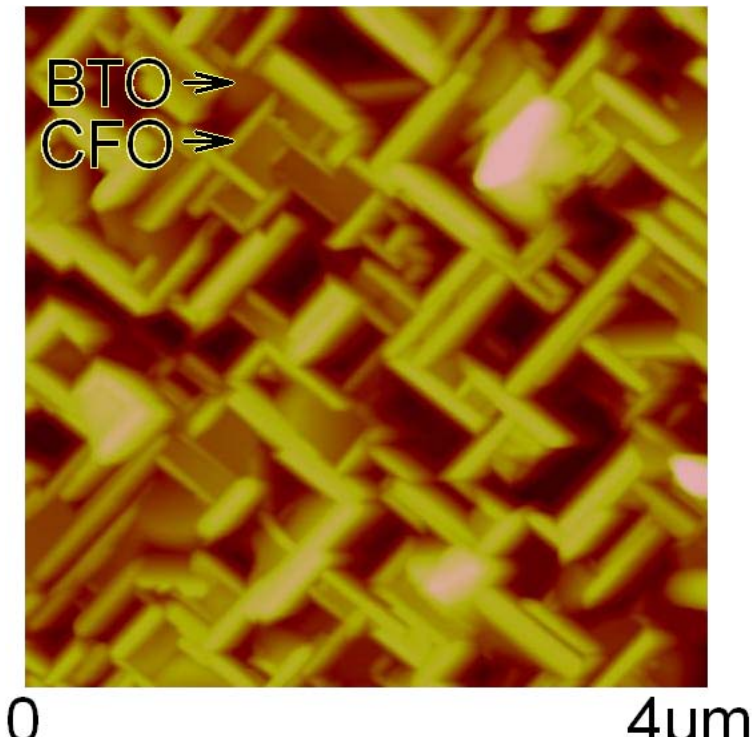

Figure 4.5 AFM images of $BaTiO_3$-$CoFe_2O_4$ nano-composite deposited on a (001) $SrTiO_3$ substrate. The image reveals an elongation of the $CoFe_2O_4$ phase regions along the <110> or <1$\bar{1}$0> directions.

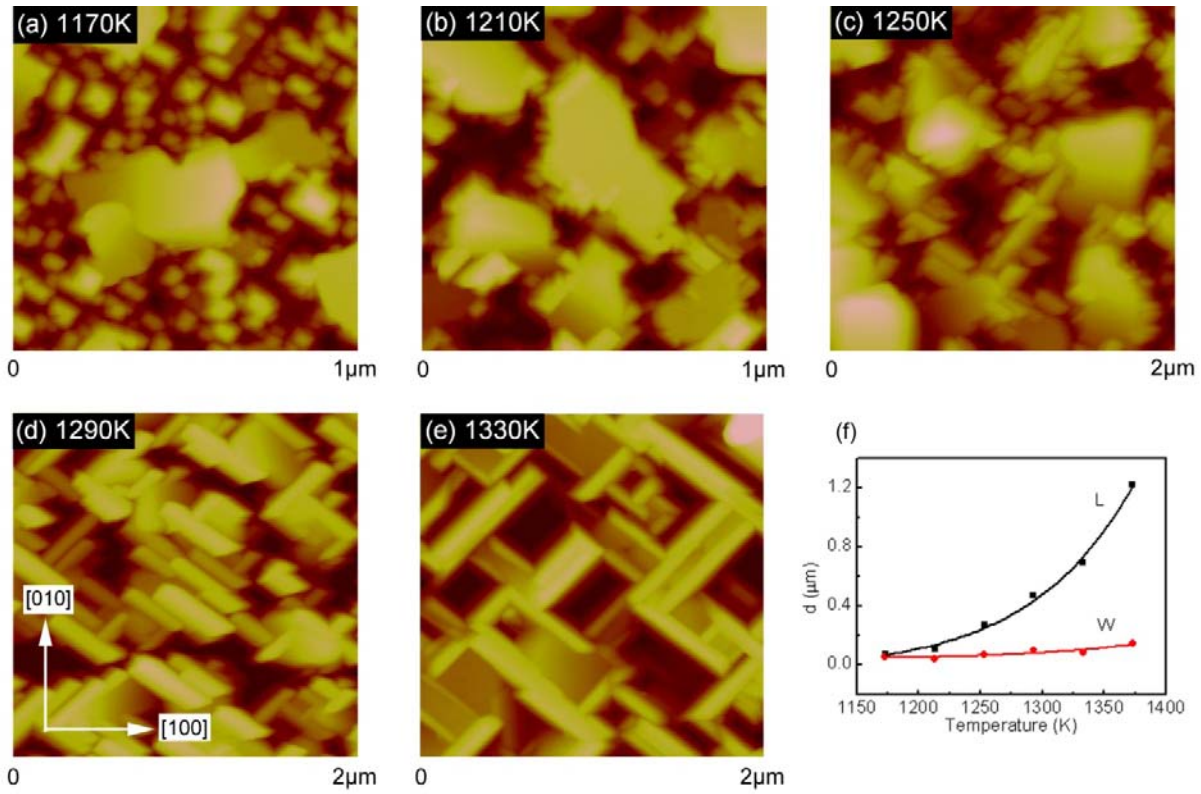

Figure 4.6 AFM images of $BaTiO_3$-$CoFe_2O_4$ nano-composite thin films deposited on (001) $SrTiO_3$ substrates and annealed at various temperatures of: (a) 1170K, (b) 1210K, (c) 1250K, (d) 1290K and (e) 1330K. The images demonstrate the evolution of the nano-structure with temperature. Part (f) shows the average size of the $CoFe_2O_4$ nano-belts as a function of annealing temperature.

increasing annealing temperature to 1250K (Fig. 4.6c), the spinel regions further coarsened. After annealing at 1290K, the morphology of the spinel phase began to self-assemble into belt-shaped nano-structures elongated along the [110]: in this case, the pyramidal crystallites disappeared. Finally, at 1330K (Fig. 4.6e), the CFO nano-belts coarsened in the BTO matrix.

In Figure 4.6f, we show the average length (L) and width (W) of the spinel phase regions in the BTO-CFO thin layers as a function of annealing temperature. These averages were taken by analysis of 10 spinel regions. Small spinel regions of sizes L≈W=100nm were first found on the edges of the matrix at 1210K. With increase of temperature to 1250K, the average size of the spinel phase regions increased only slightly to L=300nm and W=100nm. However, on heating to 1290K, the length of the spinel phase along the [110] direction increased much more prominently than that of the width along the $[1\bar{1}0]$: L=700nm and W=120nm. This anisotropy of the spinel phase regions reflected the predominance of a nano-belt morphology. With increasing temperature to 1370K, the average length of the CFO nano-belts increased to L≈1.2μm, with a width of W≈0.15μm.

In the case of 2D diffusion, the diffusion coefficient can be expressed as: $d^2 = 4Dt$; where d is the lateral size of the CFO nano-structure, D the diffusion coefficient, and t the time. The diffusion coefficient D is thermally activated given as: $D = D_0 e^{-\frac{E_a}{kT}}$; where D_0 is the maximum diffusion coefficient, E_a the activation energy, k the Boltzmann constant (8.617×10^{-5}eV), and T the temperature. It then follows that:

$$Ln(d) = \frac{1}{2}Ln(4D_0t) - \frac{E_a}{2kT} = A - B\frac{1}{T}$$

where $A = \frac{1}{2}Ln(4D_0t)$, and $B = E_a/2kT$. Accordingly, the maximum diffusion coefficient of CFO can be estimated as $D_0 = \frac{1}{4t}e^{2A}$, and the activation energy for diffusion of CFO as $E_a = 2kB$. Clearly, it can seen that the higher the value of A, the higher that of D_0; and also the higher the value of B, the higher that of E_a.

The relationship between Ln(d) and 1/T for the CFO nano-belts is shown in Figure 4.7, which was derived from Figure 4.6f. Since A along the length direction (A_L=24) is larger than that along the width (A_W=11), it follows that the maximum diffusion coefficient along the length direction is much higher than that along the width. It can be estimated that the diffusion activation energy of CFO nano-belts along the width direction is ~1.6eV, while that along the length is ~4.1eV. Previously, the CFO nano-pillars in BTO-CFO have been reported to have E_a=1.56eV [79]. Seemingly, diffusion along the width of the nano-belts follows a similar diffusion mechanism as that for the nano-pillars; whereas, that along the length direction has another diffusion mechanism, which can occur more rapidly at elevated temperature.

Structural studies by XRD are shown in Figure 4.8 for various temperatures. In this figure, we can see that the peak positions of BTO and CFO after annealing at 1330K are close to that of bulk materials and their normal position. This demonstrates at these high temperatures that CFO and BTO are not in solid solution with each other, but rather occur as pure end members. At 1070K, both the CFO and BTO peaks shifted with respect to each other: BTO to lower angles and CFO to higher ones: in addition, the peaks were notably broadened. The reason for these shifts may be that the poorly crystallized spinel and perovskite phases are inter-diffused with each other: i.e., neither phase is compositionally homogeneous. With increase of annealing

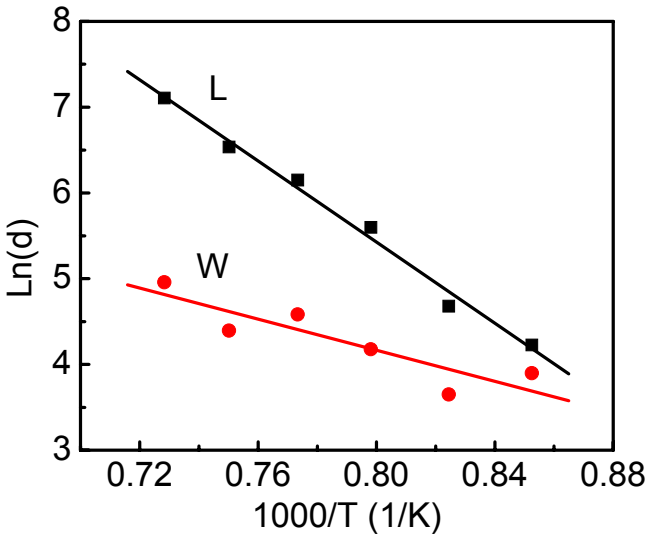

Figure 4.7 Temperature dependence of the lateral size of $BaTiO_3$-$CoFe_2O_4$ nanostructures deposited on (001) $SrTiO_3$ substrates.

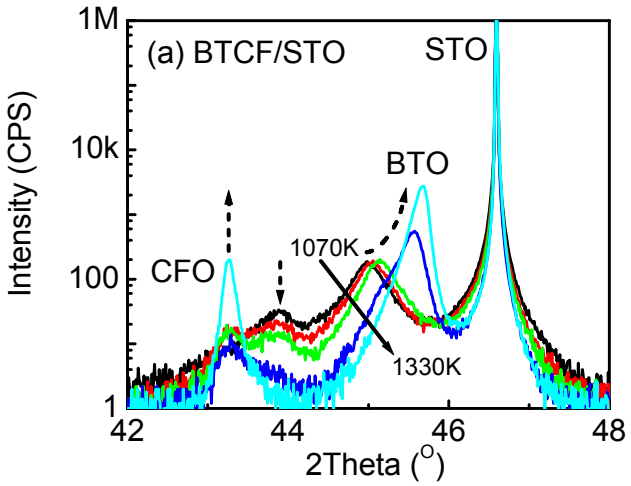

Figure 4.8 X-ray diffraction results of $BaTiO_3$-$CoFe_2O_4$ nano-composite thin films deposited on (001) SrTiO3 substrate after annealed at various temperature from 1070K to 1330K. The results show the effect of temperature on the evolution of the two phases.

temperature, the BTO peaks shifted gradually to their normal positions. Whereas, for CFO, a new peak at a different position gradually appeared, whose intensity increased with increasing annealing temperature. Finally, at 1330K, the lower temperature CFO peak disappeared and a new one (i.e. with lattice parameters equal to bulk CFO) remained. From these data in combination with the AFM images, we can draw the conclusion that a more homogeneous CFO phase with larger lattice parameters decomposes and coarsens from the composite thin films, and accordingly BTO also becomes more compositionally uniform.

C. Comparison of BTO-CFO nano-structures: rapidly annealed vs slowly annealed

We next investigated two-phase epitaxial layers grown under the same conditions but annealed at different rates, subsequently. In Figure 4.9a, we show a BTO-CFO layer annealed at 1270 K, directly after deposition at 1070K. The CFO crystallized as pyramids with (111) facets and [110] edges in the out-of-plane direction. This nano-structure is similar to that of the nano-rods, previously reported by Zheng et al [79], which were deposited at even lower temperatures without annealing. Our nano-structures prepared here by quick annealing at higher temperatures are notably more assicalar than these previously reported nano-pillars. Furthermore, these pyramidal nano-structures are in stark contrast to those formed by a more gradual anneal (dwell one hour after a 40K ascending step): which resulted in the nano-belt structure of Figure 4.9b. In the case of slower anneals, the CFO nanostructure grows along an in-plane direction, rather than an out-of-plane one.

It is natural to ask why our CFO nano-pillars grew in-plane, and why growth rate can make a difference in morphology. Two growth mechanisms for BTO-CFO perovskite-spinel

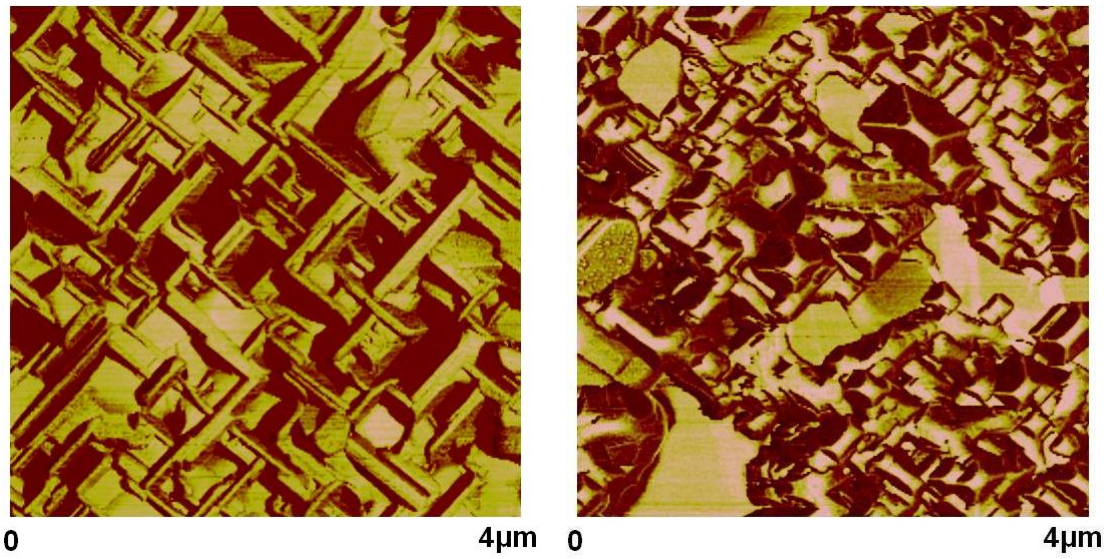

(a) BFCF/STO quick anneal at 1270K (b) BFCF/STO slow anneal at 1290K

Figure 4.9 AFM images of $BaTiO_3$-$CoFe_2O_4$ nano-composite thin films for (a) quick ramp rate and (b) slow ramp rate anneals for layers grown on (001) $SrTiO_3$ substrates; and (c) with and (b) without an additional CFO buffer layer on (001) $SrTiO_3$ substrates grown using a slow ramp rate. The images illustrate the different $CoFe_2O_4$ nano-structures that can be grown under different growth conditions.

nano-composite thin films may take effect during annealing. First, there is a conventional diffusion-controlled mechanism. If the anneal temperature is high enough to allow ions to diffuse readily, the cubic symmetry of the perovskite and spinel phases will result in a net diffusion coefficient of one in the other with cubic symmetry. Consequently, CFO grains will crystallize with pyramidal square bases. Secondly, our experiment results also suggest a ledge growth mechanism [145, 148]. In this case, growth occurs on the surface of nuclei by a step-by-step or layer-by-layer mechanism, resulting in smooth surface. Furthermore, ledge growth in spinels is known to be anisotropic, resulting in CFO growth along the [110].

D. Effect of nano-structure on magnetization:

Finally, the magnetization of BTO-CFO nano-pillar, BTO-CFO nano-belt, and single-phase CFO thin films are shown in Figures 4.10a, b and c respectively. These results show general trends. The remnant magnetization (out-of-plane) was lower and the field required to approach magnetization saturation was higher for CFO nano-belts than for CFO nano-rods. The reason is seemingly simple: the nano-belts have magnetization directions that preferentially lie in-plane due to the shape anisotropy. The structure of the nano-belts makes it more difficult to magnetize out-of-plane, relative to nano-rods.

E. Section Summary

In summary, for two phase BTO-CFO epitaxial thin films deposited on (001) STO, we have found that the spinel phase anisotropically grows along the [110]. We attribute this to an anisotropic ledge growth mechanism. Evolution of the CFO nano-belt morphology elongated along the [110] was observed to be favored with increasing temperature and slower annealing

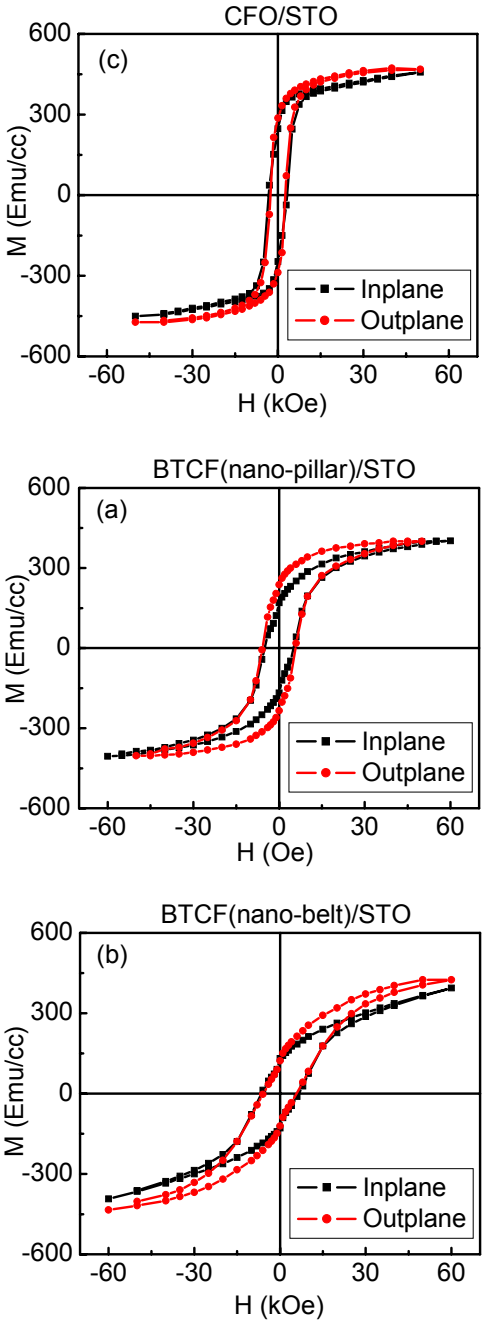

Figure 4.10 SQUID results for (a) $BaTiO_3$-$CoFe_2O_4$ nano-pillars, (b) $BaTiO_3$-$CoFe_2O_4$ nano-belts, and (c) $CoFe_2O_4$ single layer thin film, the value of magnetization is normalized by the volume ratio of the CFO phase in the nano-composite. The results illustrate the different magnetization behaviors of the $CoFe_2O_4$ phase in the various nano-structures that we observed.

ramp rates. The nano-belt structure notably reduces the remnant magnetization and increases the field required to reach saturation, relative to nano-rods or single CFO phase layers.

4.3 Magnetoelectric and multiferroic properties of variously oriented epitaxial $BiFeO_3$-$CoFe_2O_4$ nano-structured thin films

4.3.1 Background

BFO-CFO is a multiferroic material. Multiferroics are materials that have more than one primary ferroic order parameter. The term multiferroic was first used by Schmid [7], which initially only referred to single phase materials, but was later expanded to include any material that had two or more types of long range spontaneous (magnetic, ferroelectric, and/or ferroelastic) orderings. An early and important type of multiferroic was magnetoelectric (ME) materials, which possessed both ferromagnetic and ferroelectric orderings. The ferroelectric properties of the composite are similar to the single ferroelectric phase in the composite. But the ferromagnetic and magnetoelectric properties of the composite are sophisticated.

It has been reported that CFO nano-pillars embedded in a BTO matrix have strongly anisotropic magnetic properties [26]. The M-H curve measured in the out-of-plane direction is square with relatively large coercive fields (5kOe) that saturate quickly on further increase of H (10kOe). However, the magnetization along the in-plane direction is slim loop, with a small coercive field (1kOe) that saturates much more slowly with increasing H (50kOe). After comparing the magnetic anisotropy of CFO nano-pillar structures prepared at different deposition temperatures, Zheng et al. [26, 81] found that this anisotropy was induced by the

constraint stress of the hetero-structure. With increase of deposition temperature, this magnetic anisotropy was found to decrease [81].

Recent investigations have revealed a relationship between the magnetic anisotropy and the height/diameter ratio of NFO nano-pillars [149]. It was found with increasing film thickness that the height of the NFO nano-pillars increased: as a result, the aspect ratio obviously also increased. The magnetic anisotropy is strongly related to the aspect ratio of the spinel phase. For thinner films (1:2 aspect ratio for NFO), the M-H curves in the in-plane and out-of-plane directions were almost the same; but for thicker films (10:1 aspect ratio for CFO), the M-H curve for in-plane was much slimmer and harder to saturate, relative to out-of-plane.

Not only can nano-pillars with out-of-plane orientations be deposited, but our research group has found that nano-belts elongated along in-plane directions can also be deposited. This makes it possible to study the relationship between various nano-structures and magnetic behaviors.

The first indication of ME coupling in self-assembled nano-composite thin films was reported for the BTO-CFO system in 2004 [26]. A kink was observed in the magnetization at the ferroelectric Curie temperature of the BTO phase. At this temperature, the BTO matrix underwent a phase transformation from cubic to tetragonal. The change in the perovskite crystal structure of the BTO matrix then resulted in a distortion of the CFO crystal structure. As a consequence, the magnetization of CFO was reduced at this temperature, via magnetostriction.

Other evidence of ME coupling has been provided by studies of electric field assisted magnetization switching using a MFM method [93]. On applying a voltage of -16V to the film and no magnetic field applied, approximately 50% of the magnetization of the CFO nano-pillars

was rotated due to a ME coupling between BFO and CFO. If the film was then exposed to a magnetic field while under this voltage of -16V, the percentage of spin rotation increased with increasing DC magnetic field: up to 90% could rotate under H=800Oe.

There have also been several reports of ME coupling in (0-3) and (2-2) type composite thin films by other measurement methods. These include: (i) the saturation polarization being decreased from 80μC/cm^2 to 25μC/cm^2 when a DC magnetic field of 10kOe was applied to (0-3) CFO-PZT thin films [150]; (ii) the ferroelectric coercive field being increased from 4.8MV/m to 6.6MV/m under application of DC magnetic field of 5kOe for (2-2) PZT/CFO thin films [151]; (iii) the ferromagnetic resonance frequency of yittrium iron garnet or YIG layers being increased by 5Oe when a voltage of 25V was applied to (Ba,Sr)TiO_3 or BSTO layers which were deposited on the top of the YIG one [152]; and (iv) a ME voltage output of 5μV that was observed when a square wave AC magnetic field of 6Oe was applied to a (2-2) NFO/BTO composite thin film [133].

4.3.2 Magnetoelectric and multiferroic properties of epitaxial $BiFeO_3$-$CoFe_2O_4$ nano-structured thin films

A. Nano-structure

Epitaxy of BFO-CFO films deposited on (001), (110) and (111) STO substrates with SRO buffer layers was confirmed by XRD, as shown in Figure 4.11a. For (001) layers, the peaks between 43°<x<47° were (004) CFO, (002) BFO, (002) SRO and (002) STO. The (002) of BFO and SRO were very close. For (110) layers, the peaks between 30°<x<33° were (220) CFO, (110) BFO, (110) SRO and (110) STO. For (111), the peaks between 37°<x<40° were (222) CFO, (111) BFO, (111) SRO and (111) STO.

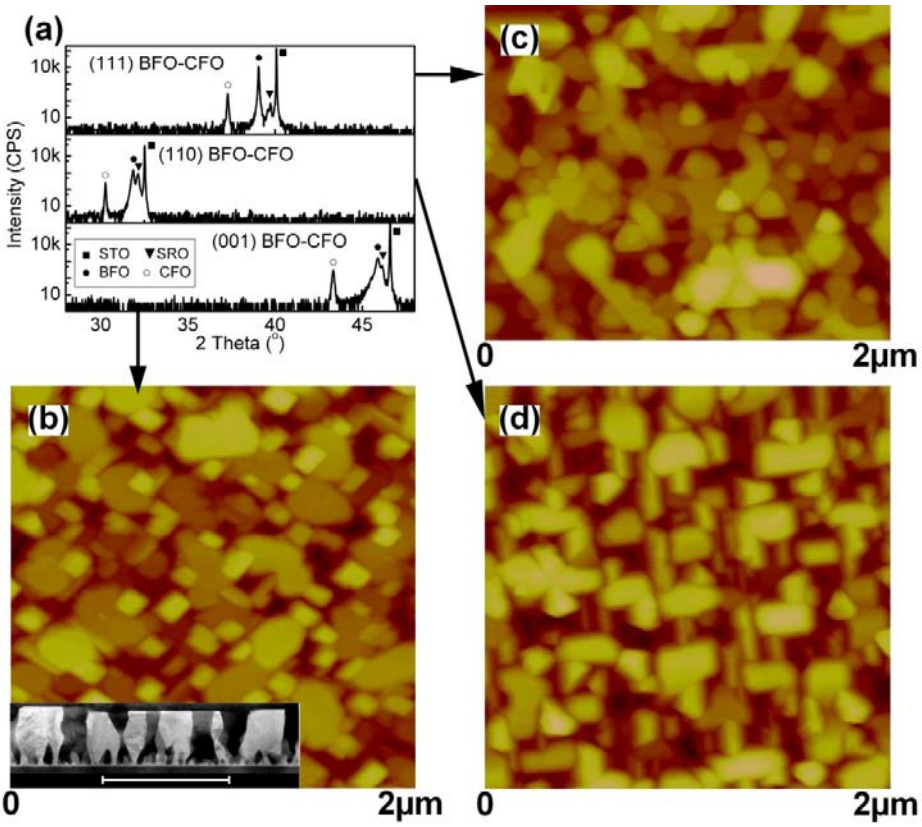

Figure 4.11 X-ray diffraction line scan and atomic force microscopy image for (001), (110) and (111) BFO-CFO thin films. (a) XRD line scan over a wide range of angles that demonstrate phase purity and good epitaxy; and AFM images that demonstrate the nano-structures of (b) (001), (c) (110) and (d) (111) oriented thin films, where the inset of (b) is cross-section TEM image of (001) BFO-CFO film.

The nano-structures of (001), (110) and (111) oriented BFO-CFO layers were studied by AFM, as shown in Figure 4.11b-d respectively. The nano-structures for these various orientations were similar to that previously reported [79]. On (001) STO, the CFO phase formed as pyramidal nano-pillars defined by (111) facets and [110] edges, which was embedded in a BFO matrix. On (110) STO, CFO formed as a nano-ridge with (111) facet roofs and [110] ridges, embedded in a BFO matrix. On (111) STO, CFO formed as the matrix phase, with embedded BFO triangular nano-pillars. The cross-sectional TEM image of the film is shown in the inset of Figure 4.11b: from bottom to top are $SrTiO_3$, $SrRuO_3$ and BFO-CFO layers respectively. The CFO appears as the dark pillars embedded in a bright BFO matrix.

B. Ferroelectric properties

First, the dielectric properties were studied to insure that the BFO-CFO nano-composite films had a relatively high resistance. The room temperature dielectric constants of (001), (110) and (111) BFO-CFO were 143, 97, and 93; and the loss tangents were 0.092, 0.098 and 0.205 respectively. Prior investigations have reported that the dielectric constant of BFO and CFO are 95 and 38 [153-154], and that the loss tangents are 0.05 and 0.24, respectively. Clearly, our BFO-CFO nano-composite films have reasonable properties of dielectric insulators.

The P-E loops for (001), (110) and (111) films were measured at room temperature, as shown in Figure 4.12. Polarization saturation is evident in these data; however, some leakage can also be seen at higher electric fields, as evidence by rounding of the corners of the loops. The saturation polarization followed a trend of $P_{s(111)}>P_{s(110)}>P_{s(001)}$ ($86\mu C/cm^2$, $65\mu C/cm^2$, $60\mu C/cm^2$). The remnant polarization followed a trend of $P_{r(111)}>P_{r(110)}>P_{r(001)}$ ($79\mu C/cm^2$,

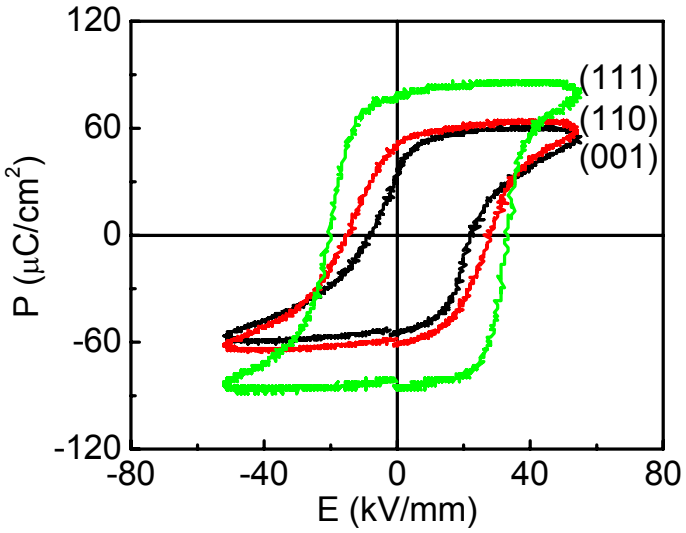

Figure 4.12 Polarization or P-E hysteresis loops for (111), (110) and (001) BFO-CFO nano-composite thin films.

55μC/cm^2, 44μC/cm^2). The coercive fields had a trend of $E_{c(111)}>E_{c(110)}>E_{c(001)}$ (27kV/mm, 22kV/mm, 15kV/mm).

The longitudinal piezoelectric d_{33} coefficients were then measured by piezo-force microscopy as shown in Figure 4.13. Maximum values of d_{33} for (001), (110) and (111) BFO-CFO films were determined to be about 50pm/V, 40pm/V and 30pm/V, respectively. An asymmetry can be seen between the right and left wings for both the (110) and (111) films: where the right side is much lower than the left. Furthermore, the coercive fields for the films were asymmetric: this indicates a built-in field or charge in the thin film, possibly due to defects at the interphase interfaces.

In general, the ferroelectric properties of our BFO-CFO nano-composites were similar to those previous reports for single phase BFO thin films regardless of nano-structure. For example, P_s and E_c for (111) BFO were higher than for the other orientations, both for single phase BFO films [155] and our BFO-CFO nano-composite ones. Furthermore, d_{33} was highest for the (001) oriented BFO, both as a single phase layer [155] and as a BFO-CFO nano-composite one.

C. Ferromagnetic properties

Next, the ferromagnetic properties were measured at 250K by SQUID, as shown in Figure 4.14. The magnetization values were normalized to the volume fraction of the CFO phase. The shapes of the out-of-plane M-H hysteresis loops of (001), (110) and (111) BFO-CFO were similar to that previously reported for CFO single phase films [156-159]. This is because the CFO nano-structures for BFO-CFO films along the out-of-plane direction are the same as that for single phase CFO ones: i.e., spin rotation is not limited in the out-of-plane direction. The

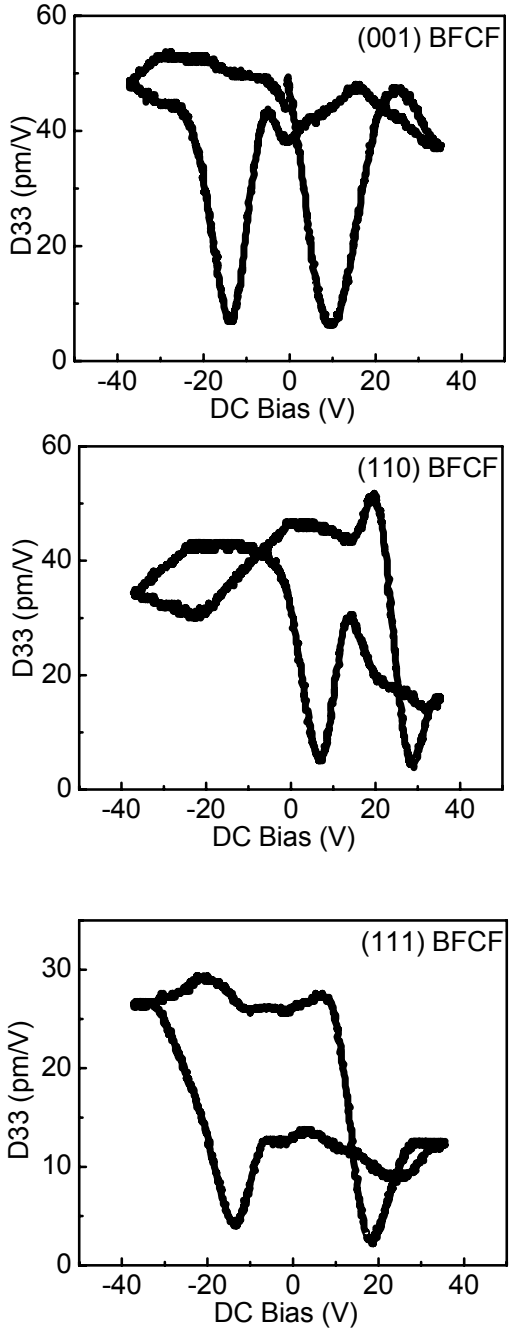

Figure 4.13 Longitudinal piezoelectric d_{33} coefficient as a function of DC electric bias for (a) (001), (b) (110) and (c) (111) BFO-CFO nano-composite thin films.

saturation magnetization was M_s=400emu/cc and the coercive field was H_c=2~3kOe. Please note that these values for M_s were a little smaller than those for single phase CFO films, which was reported to be 530emu/cc [156-159].

The M-H loop for the in-plane direction of (001) BFO-CFO is shown in Figure 4.14a. Compared with the out-of-plane loop, the in-plane one has a lower H_c, a lower remnant magnetization M_r, and a higher saturation field (H_s). Because the CFO phase in this case forms as nano-pillars embedded in a BFO matrix, the translational symmetry of the CFO phase is broken and the various nano-pillars do not connect to each other along the in-plane direction. As a consequence, the spin can not be stably aligned along the in-plane direction: this makes spin rotation easy, but saturation difficult to achieve in-plane.

The M-H loops for the in-plane direction of (111) BFO-CFO were also similar to those previously reported for single phase CFO films [156-159], as shown in Figure 4.14c. This is because the CFO phase is the matrix phase, processing dimensional connectivity along the in-plane direction. In addition, the M-H loops for in-plane and out-of-plane directions had similar values of H_c and M_r; although M_r in-plane was slightly higher than that out-of-plane, as the spin state is more stable in-plane due to the spread of the CFO matrix phase.

The M-H loops for the in-plane direction of (110) BFO-CFO were intermediate in characteristics between those of (001) and (111) films. The (110) films had in-plane M_r and H_c values that were intermediate in those for (001) and (110): this may simply reflect the fact that the CFO phase of the nano-structure for (110) did not spread out as much as that for (001), and also was not as well dimensionally inter-connected along the in-plane direction as that for (111).

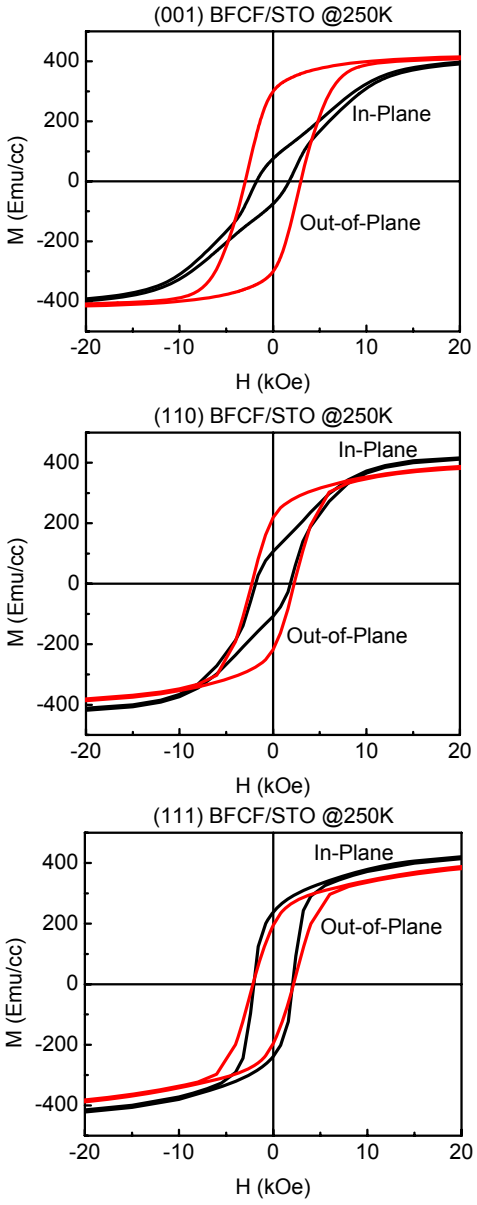

Figure 4.14 Magnetization or M-H hysteresis loops in both in-plane and out-of-directions for (a) (001), (b) (110) and (c) (111) BFO-CFO nano-composite thin films. The magnetization was normalized to the volume fraction of the CFO phase.

In general, the ferromagnetic properties of BFO-CFO nano-composite thin films were strongly dependent on the nano-structures of the CFO phase. The more dimensionally interconnected the CFO nano-structures were, the more the M-H loops resembled that of CFO single phase layers. Correspondingly, the more dimensionally isolated the CFO nano-structures were, the more unstable the spin alignment was along that direction. For example, the CFO phase for (001) BFO-CFO was only connected in the out-of-plane direction, thus the M-H loops along that direction were similar to CFO single phase films; whereas, on (111) substrates, the CFO phase was connected in all directions, and the M-H loops for in-plane and out-of-plane directions were both similar to each other and similar to those for CFO single phase layers.

D. Multiferroic properties, as measured by AFM and MFM.

The FE and FM natures of the BFO-CFO nano-composites were also studied by piezo-force (PFM) and magnetic-force (MFM) microscopies, respectively. A PFM image of (001) BFO-CFO film is shown in Figure 4.15a: a 7μm×7μm square was poled by -10V, where a 5μm×5μm area was subsequently reversely poled by +10V. Switching of the polarization was evidenced by the change in contrast in the PFM images between the $5\times5\mu m^2$ sub-area and the layer $7\times7\mu m^2$ one. This notable contrast change indicates a change in the sense of the polarization direction under E. In addition, magnetic force images of (001) films magnetized by +1kOe and -1kOe are shown in Figures 4.15b and 4.15c respectively. Cross lines are used to identify near-exact positions in the figures, making visual comparisons easier. On comparing these two images some regions can be seen to be nearly opposite in contrast upon changing the sense of H. This shows that the magnetization orientation is nearly reversed between applied fields of -1kOe and 1kOe. These images in Figure 4.15 demonstrate the multiferroic

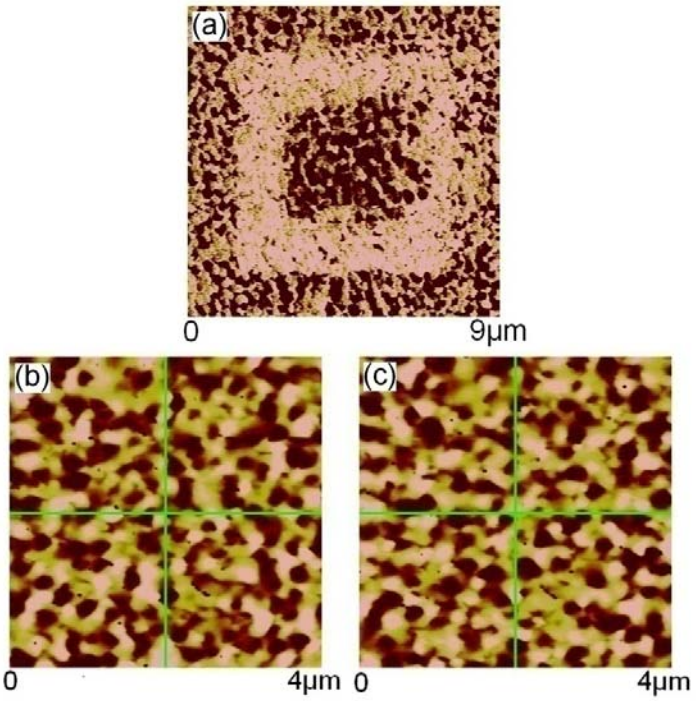

Figure 4.15 Multiferroic properties of (001) BFO-CFO nano composite thin films. (a) PFM images of BFO-CFO thin film after poled by E=-10V applied to a 7μm×7μm and E=+10V applied to a 5μm×5μm area, which demonstrate polarization rotation; and MFM images of BFO-CFO thin films magnetized by (b) H=+1kOe and (c) H=-1kOe applied to same regions as those in PFM image, which demonstrate spin rotation.

characteristics and a local scale for our ME nano-composites, which are similar in nature to the average ones measured by P-E and M-H hysteresis loops.

E. Magnetoelectric properties

Our method for directly measuring the ME voltage of BFO-CFO thin films is illustrated in Figure 4.16, which was built in our lab. A photo is given in Figure 4.16: a shaker was used to generate a vibration at a constant frequency and amplitude, which was then used to excite the vibration of a magnet cantilever. The detailed structure of the magnetic cantilever is illustrated in the inset of Figure 4.16. Permanent magnets were fixed to both ends of a steel slither. By adjusting the input voltage signal to that of the drive of the shaker, the vibration amplitude of the magnetic cantilever was controlled: the larger the vibration amplitude, the larger the AC magnetic field. The relationship between the vibration amplitude of the magnetic cantilever and the value of the induced AC magnetic field was calibrated using a Gauss meter. The BFO-CFO nano-composite thin film was placed in the center of the two magnets at a distance of 3.5mm from each of them. The polarization was measured in the out-of-plane direction, and the AC magnetic field was applied along the in-plane or out-of-plane directions. The ME voltage signal was read by a lock-in amplifier. Using this magnetic cantilever ME measurement method, it was found possible to generate large AC magnetic fields of up to $H_{AC}=10^3$Oe. This then made it possible to induce ME voltage responses of larger than 1mV. By this method, we found it possible to avoid near-field electric coupling to the wires bonded to the sample, which following conventional ME measurement methods had inductive coupling to the AC magnetic field, resulting in enhanced noise.

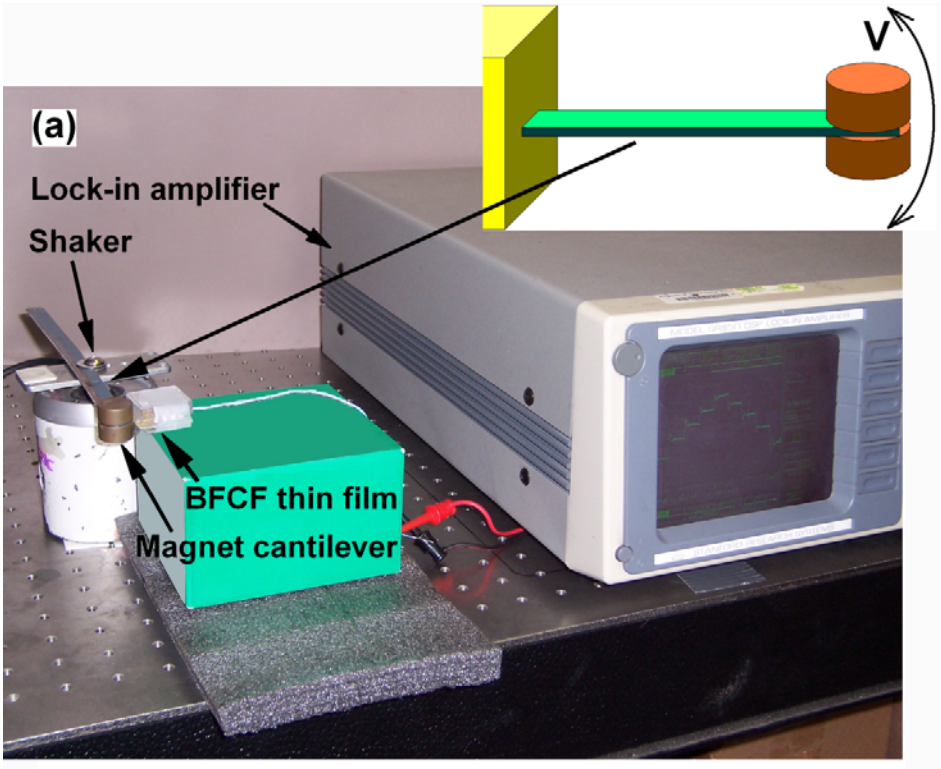

Figure 4.16 Photo of our magnetic cantilever ME measurement method, where the inset is a schematic structure of the magnetic cantilever

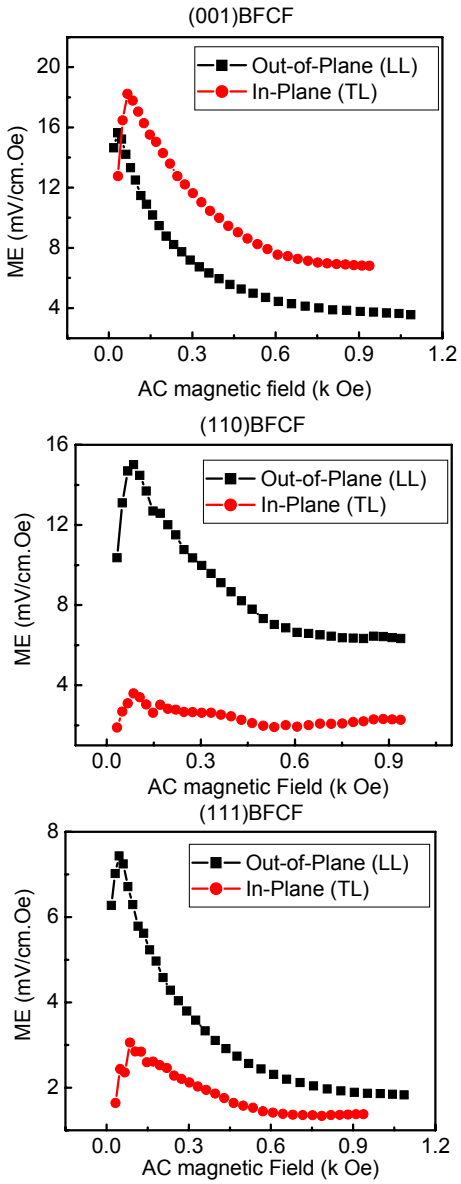

Figure 4.17 Magnetoelectric coefficient for (a) (001), (b) (110) and (111) oriented self-assembled BFO-CFO nano-composite thin films as a function of AC magnetic field amplitude in both out-of-plane (longitudinal-longitudinal) and in-plane (transverse-longitudinal) directions.

We measured the ME coefficient as a function of AC magnetic field for the (001), (110) and (111) BFO-CFO nano-composite films along both in-plane and out-of-plane directions as shown in Figure 4.17. Please note that the L-L mode designates a longitudinally magnetized and longitudinally poled coefficient, whereas the T-L mode designates a transversely magnetized and longitudinally poled one. The L-L and T-L mode coefficients were measured by applying an AC magnetic field along the out-of-plane and in-plane directions, respectively. In this figure, the ME coefficient can be seen to increase rapidly with increase of AC magnetic field, reaching a maximum value near HAC≈100Oe, and the decreasing gradually with further increase of HAC.

For (110) and (111) films, the ME coefficients for the out-of-plane direction were about 3 to 4 times higher than those in-plane, this is similar in trend to that between L-L and T-L modes for bulk ME composites, as previously reported [9]. In the case of the L-L mode, the magnetostriction strain of the CFO phase is oriented along the longitudinal direction. Due to elastic coupling at the interphase interfaces, this strain is then transferred to the FE phase: which in turn generates a voltage, via the piezoelectric d_{33} coefficient, along the longitudinal direction. For the T-L mode, the magnetostriction strain of the CFO phase is oriented along the transverse direction, which is elastically coupled at the interphase interfaces to BFO, generated a voltage via d_{31}. Since $d_{31}<d_{33}$, the ME voltage for the T-L mode is notably less than that of the L-L.

However, for (001) films, the ME coefficients in the T-L mode were slightly higher than that for L-L - an anomalous result for the anisotropy of the ME tensor coefficients. The origin of this anomaly is not certain at this time. We could conjecture that this anomalous ME behavior may reflect an asymmetric magnetic behavior for (001) BFO-CFO films (see Figure 4.14), where H_c for the in-plane direction was only half that for the out-of-plane one. Consequently, the magnetization of (001) CFO might rotate more easily along the in-plane direction than it can for

the other orientations of CFO thin films. If that was the case, the effective linear magnetostricive coefficient for CFO nano-pillars along the in-plane direction might be appreciably enhanced.

In general, the maximum value of the ME coefficient for the L-L mode of BFO-CFO films follows the trend of $ME_{(001)}>ME_{(110)}>ME_{(111)}$ (16mV/cm·Oe, 15mV/cm·Oe, 8mV/cm·Oe). The underlying reason may be simply that the longitudinal piezoelectric d_{33} coefficient of the BFO phase of the BFO-CFO films follows the trends of $d_{33\ (001)}>d_{33\ (110)}>d_{33\ (111)}$. Another contributing reason may be the fact that the constraint stress imposed by the substrates follows the trend of $\sigma_{(111)}> \sigma_{(110)}> \sigma_{(001)}$; accordingly, the constraint stress for the CFO nano-pillars on (001) STO substrates may be less than that for a CFO matrix phase on (111) STO.

F. Section Summary

The FE, FM and ME properties of (001), (110) and (111) two phase BFO-CFO nano-structured thin films were studied. Our results demonstrate that (i) the FE properties are similar to those of single phase BFO, following a trend of $P_{(111)}>P_{(110)}>P_{(001)}$; (ii) the FM properties depend on the nano-structure of the CFO phase, with a difference between in-plane and out-of plane directions that follows a trend of (001)>(110)>(111); and (iii) the ME properties depend on the combined effects of FE/FM properties and the nano-structure, where the ME coefficient follows a trend of $ME_{(001)}>ME_{(110)}>ME_{(111)}$.

4.4 Summary

We have studied various developments in multiferroic two-phase nano-composite thin films: with emphasis on our efforts to explore their new nano-structures, to understand their ferroelectric and ferromagnetic behaviors, and to improve their ME voltage output signals. Our

finding included: (i) nano-belt structures in perovskite-spinel systems that can be explained by an anisotropic ledge growth mechanism for the CFO phase; (ii) the ferroelectric properties of composite thin films, which are similar to those of single ferroelectric phase; (iii) a strong magnetic anisotropy for nano-structure thin films, which is related to aspect ratio of the ferrite phase of the nano-structure; and (iv) the ME coupling between the piezoelectric and magnetostrictive phases as observed by several ways, such as a change in ferrite magnetization induced at the ferroelectric Curie temperature, a rotation of spin under weak magnetic fields that is assisted by electric fields, and the direct measurement of the ME voltage output generated by AC magnetic fields.

Chapter 5: Quasi-Ordered CFO-BFO nano-array composite thin films

Engineered heterostructures with two or more phases have been of increasing research interest for the last few years due to the possibility of obtaining novel properties that are quite different from those of the individual single phase material [160-162]. Examples of such structures include magneto-electric (ME) structures with magnetic and electrical phases, highly ordered periodic nano-arrays of two phases (i.e., chessboard structures), amongst others [26, 163-164]. It is possible to obtain electric/magnetic field control of the magnetic/electric response in ME structures. If this could be achieve in periodic nano-arrays with known in-plane co-ordinates for each phase, then the novel feat of local control in magnetic/electric properties with electric/magnetic fields in addition to easy identification of the respective phases could be realized. It can easily be seen that such structures might be very useful for future sensors, data storage, memory, logic, and communication device applications. There have previously been several reports on near-randomly distributed nano-pillar-embedded-in-matrix type ME composite structures [78-79, 83]. However, there has not been a prior demonstration of highly ordered magneto-electric nano-arrays with significant ME coupling between two phases.

5.1 Introduction

The ME effect originates from a cross-coupling between magnetic and electric dipole moments [165], resulting in a change of the polarization with applied magnetic field H, or a change in magnetization with applied electric field E. However, in single phase materials at room

temperature, the coupling between the magnetic and electric degrees of freedom is small [166]. On the other hand, engineered composite structures of magnetic and electrical phases have significantly higher ME responses [89, 92]. Both hetero- and nano-pillar-embedded-in-matrix structures with various magnetic-electrical phase connectivity configurations have previously been investigated [152, 167]. The nano-pillar thin film structures are expected to offer a better phase connectivity and reduced clamping effects from the substrate than hetero-epitaxial thin layer structures, giving rise to higher ME responses. However, the lack of control of the nano-pillar distribution has so far restricted such structures from being practical useful. If one could achieve a highly ordered ME structure, then one could have: (i) control over the spatial distribution of both phases on the nano scale with tunability of magnetism/polarization by electric/magnetic fields and (ii) a high ME coupling due to coherent interphase interfacial connectivity between the magnetic and electric phases.

There are several means by which to obtain the ordered periodic thin film structures. There have been several recent reports of self-assembled chessboard structures using both two phase composite targets and single phase targets that decompose into two ordered phases during deposition [164, 168]. The formation of these ordered structures is highly sensitive to the crystal structures, lattice parameters, and atomic positions of the two phases and the substrate [169]. Therefore, this approach highly restricts the achievement of such ordered magneto-electric structures with good magnetic (for example, $CoFe_2O_4$ or CFO) and ferroelectric (for example, $BiFeO_3$ or BFO) properties, since the conditions for the ordered structure formation are not easy to fulfill [169].

Another approach to obtaining ordered structures is a combination of several depositions followed by lithography. For example, one could first deposit a continuous piezoelectric thin

film, then pattern the film to a desired ordered shape making arrays of holes, and finally deposit the magnetic phase to fill the holes in order to achieve the ordered magneto-electric structure. For this approach the crystal structures and lattice parameters of the magnetic and electric phases need to be relatively close in order to maintain lattice coherency, however it offers much more flexibility in the choice of magnetic and electric phases than the self-assembled ordered structures whose formation conditions are much more highly restrictive [169]. Furthermore, one could control the location, size and shape of the magnetic/electric phases by lithography in order to optimize the magneto-electric coupling between the magnetic and electric phases. There has been only one report so far on ordered ME structures using this type of approach that mostly concentrated on structure and morphology, and did not show any control of the ME response [170].

Here, we report a significant control of the magnetic response by applied electric fields for an ordered magneto-electric heterostructure made by a combined deposition and lithography approach. The structure is composed of a magnetostrictive CFO nano-array embedded in a piezoelectric BFO matrix. Magnetic force microscopy (MFM) images revealed a change in the CFO magnetization on application of a voltage across the BFO matrix, demonstrating good magneto-electric coupling across the interphase interfaces of the structure. Furthermore, atomic force microscopy (AFM), piezoresponse force microscopy (PFM), and MFM images confirmed the ordered spatial distribution and desired magnetic and electric properties of the respective phases.

5.2 Experiment

The films were deposited using a Lambda 305i KrF laser with wavelength of 248nm, focused to a spot size of $2mm^2$ on the target. The distance between the substrate and target was 6cm, and the base vacuum of the chamber was $<10^{-5}$Torr. The processing flow is shown in Figure 5.1. First, a 50nm $SrRuO_3$ (SRO) bottom electrode was deposited on top of a (001) STO substrate at 660°C degree under 150mTorr O_2 pressure; then a 200nm BFO ferroelectric layer was deposited at 670°C degree under 30mTorr O_2 pressure. A 200nm Al_2O_3 (AO) sacrifice layer was then deposited on the top at 350°C degree under 100mTorr O_2 pressure.

A FEI Helios 600 NanoLab Focus Ion Beam (FIB) was used to cut ordered hole-arrays in the BFO thin films that had a AO sacrifice layer. The FIB was operated at 30kV and 93pA, and the dwell time was 60μs. The hole depth was controlled by the cutting time and was about 400nm. Three kinds of hole-arrays were cut: which were 200nm, 300nm and 400nm in diameter. After cutting, a 200nm CFO ferromagnetic layer was deposited as a top layer. By dipping into a 1 Mol/l NaOH solution for 20min, the AO layer was etched off. The areas which had CFO directly on top of AO were then also removed. This process resulted in CFO nano-arrays that were embedded in a BFO matrix. Because the AO sacrifice layer can survive at high temperature where most oxide thin films are deposited by PLD, and because NaOH does not react with most oxides, this method might be widely used to deposit patterned nano-structure composite thin films by PLD or other deposition methods.

The nano-structures of the thin films were studied using the FEI Helios 600 NanoLab Focus Ion Beam and an atomic force microscopy (AFM). The piezoelectric and magnetic

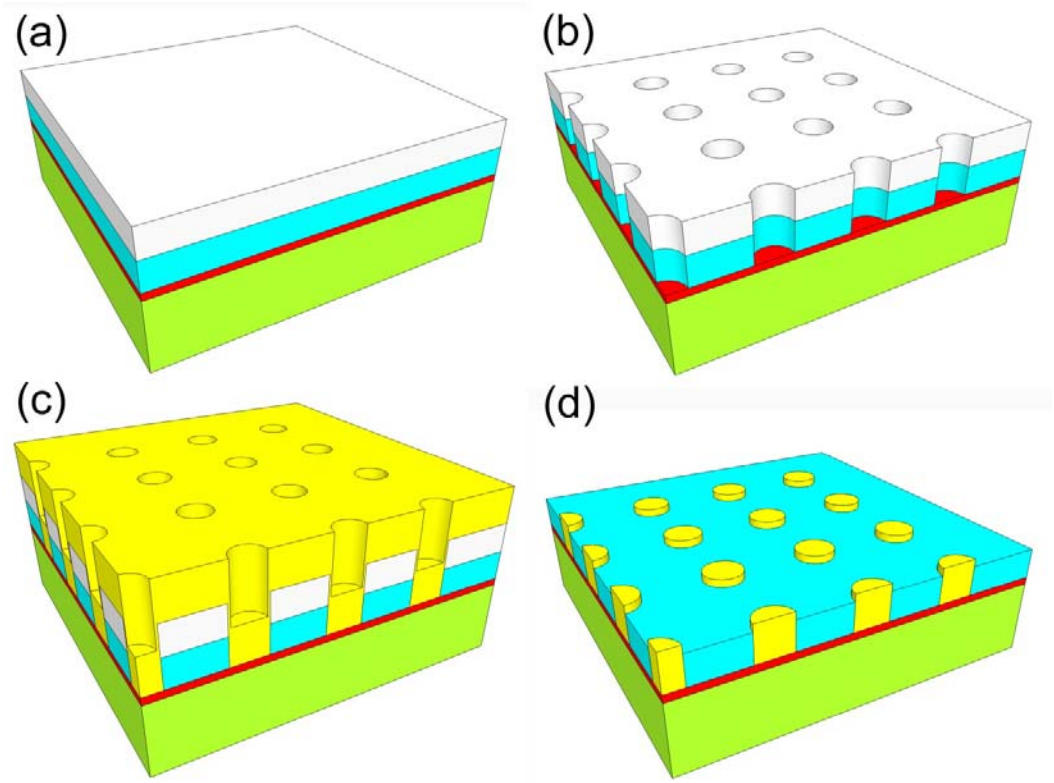

Figure 5.1 Process flow diagram of deposition of ordered CFO nano-array embedded in BFO matrix. (a) AO/BFO/SRO was deposited on top of STO substrate by PLD; (b) regular hole-array was cut in thin films by FIB; (c) CFO was deposited on top of patterned thin film; and (d) CFO/AO layers were removed by NaOH solution.

properties were measured using a Vecco Dimension 3100 with a Nano Scope V controller. The magnetization of the thin films was studied using a LakeShore Vibration Sample Magnetometer (VSM).

5.3 Multiferroic properties of ordered CFO-BFO thin films

Figure 5.2 shows schematic diagrams of our ordered structure, along with a brief illustration of the magneto-electric coupling mechanism. Part (a) shows the ordered magnetostrictive CFO nano-arrays embedded in a piezoelectric BFO matrix on top of a $SrRuO_3$ (SRO) layer and $SrTiO_3$ (STO) substrate, as indicated. The SRO layer serves as one of the electrodes by which to apply a voltage across the BFO layer. The magneto-electric exchange mechanism between the BFO and CFO phases is governed by strain mediated coupling between magnetic and electrical phases. Parts (b) and (c) show schematics of a patterned out-of-plane magnetized CFO nano-structure and the surrounding BFO matrix under positive and negative voltages, respectively. The CFO magnetization is indicated by an arrow with a solid circle at the other end, and the BFO polarization by arrows. When a voltage is applied across the BFO matrix, piezoelectricity results in an expansion of the BFO lattice. This in turn results in a strain in the adjacent magnetostrictive CFO phase regions which are elastically bonded to the BFO across coherent interfaces. It should be noted that the expansion of the BFO thin layer is asymmetric with sign of the voltages: the saturation d_{33} value is higher under negative voltage than under a positive one [24], due to a clamping effect from the substrate and charge accumulation at the BFO-substrate interface. Accordingly, the CFO magnetization is expected to decrease as the voltage is cycled from positive to negative across the BFO, as schematically illustrated in (b) and

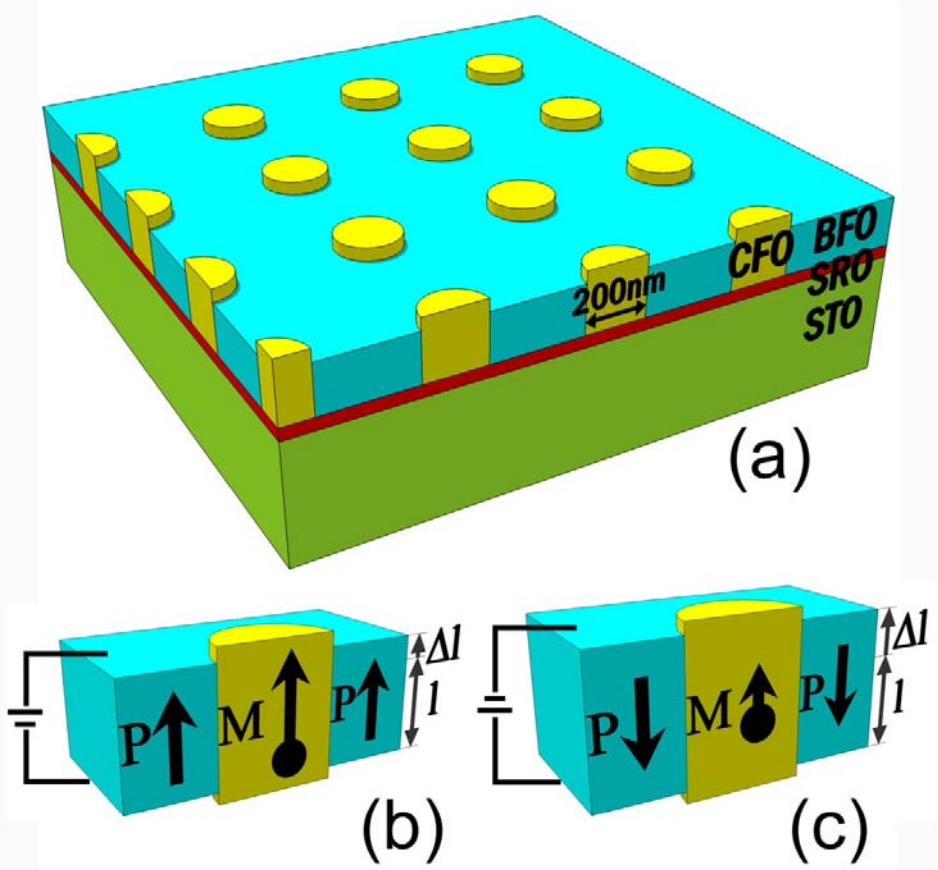

Figure 5.2 Diagram of ordered CFO nano-array embedded in BFO matrix. (a) Nano structure of CFO-BFO composite thin films; (b) and (c) change in the CFO magnetization due to different expansions of the BFO phase, with positive and negative applied voltages.

(c). It should also be noted that the ME coupling depends on the relative directions of the magnetization of the magnetic phase and polarization of the dielectric phase, easy and hard directions of the magnetization, and expansion and compression directions on the piezoelectric phase [171-172]. The concept expressed by the schematics above is specific to our CFO-BFO structure.

Figure 5.3 shows AFM and scanning electron microscope (SEM) images of our ordered ME nano-composites at different process steps. An AFM image of the top surface of the AO/BFO/SRO/STO film after FIB cutting is shown in Part (a). It can clearly be seen that an ordered hole-array (200nm diameter holes) was successfully obtained. Part (b) shows an AFM image after CFO deposition. It can be seen that the hole-array nearly maintains the original pattern after CFO layer deposition and that the diameters of the holes remain nearly the same: i.e., CFO uniformly grows on top of the nano-pattern engineered by the FIB process. Part (c) shows an AFM image after etching off the AO layer by the NaOH solution. In this figure, one can clearly see the ordered CFO nano-arrays embedded in the BFO matrix. It should be noted by changing the thickness of the CFO phase that the height of the CFO nano-rods could be controlled to be higher than the BFO matrix, or more importantly to be nearly the same. Since the CFO nano-array was slightly higher than the BFO matrix, we could observe the nano-pattern of this composite film by AFM. Please note that a few square-particulate structures were also found in the image of Figure 5.3c, which were due to a non-flat BFO surface: they originate because BFO prefers to grow as a cube, surrounded by (001) facets.

The top surface of the CFO-BFO nano-array assembly observed by SEM measurements is shown in Fig. 5.3 (d). One can see that the CFO phase nano-rod structures crystallize well in

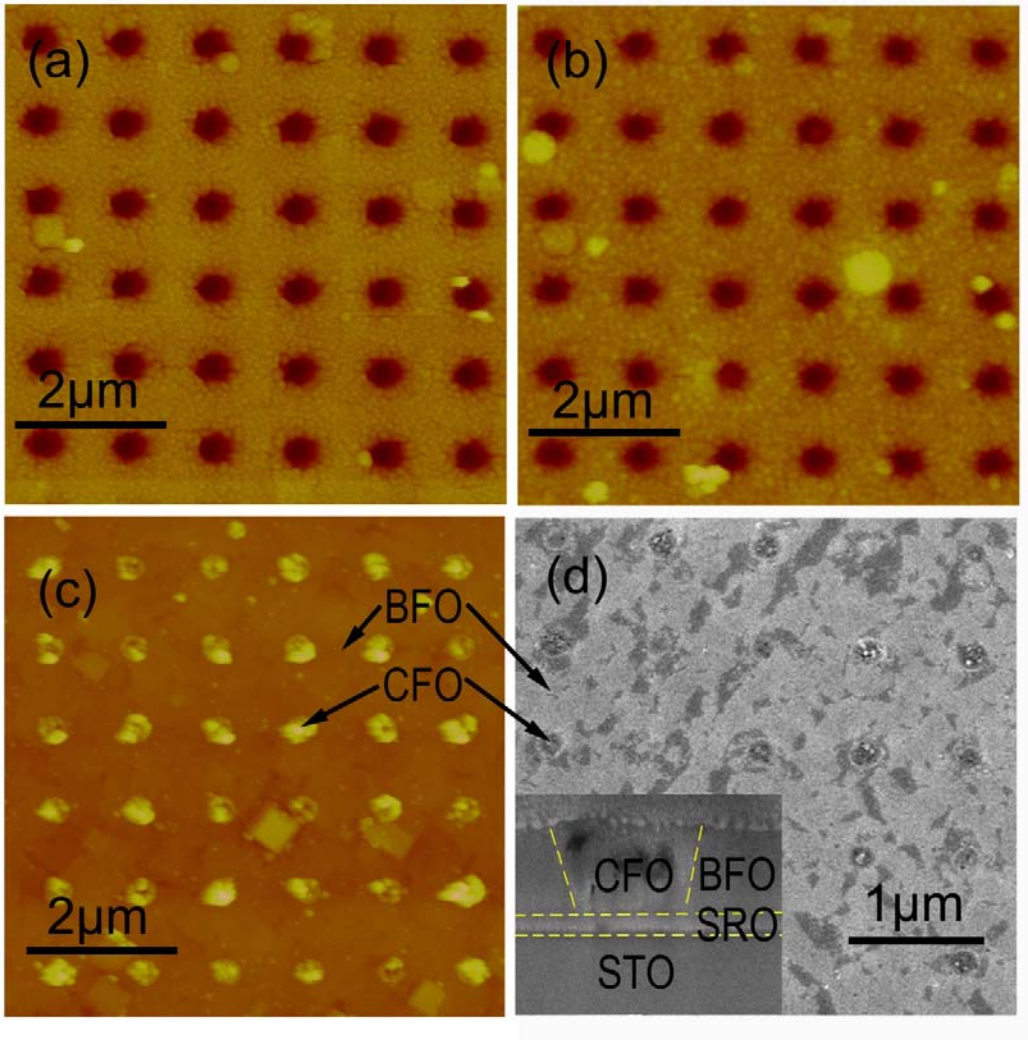

Figure 5.3 AFM and SEM results of thin films at different process steps. (a) Regular hole-array was cut in thin films by FIB; (b) CFO layer was deposited on top of patterned thin films before etching with NaOH; (c) regular CFO nano-array embedded in BFO matrix after etching by NaOH; and (d) SEM results of ordered CFO nano-array in BFO matrix, where the insert is the cross section view of the CFO-BFO composite.

the holes within the BFO matrix. The two phases are elastically coherent, capable of making good bonding across the interphase interfaces. The top surface is also quite smooth. The cross-sectional view of the CFO phase embedded in the BFO matrix is shown in the insert of this figure. It can be seen that the CFO phase nucleates within the hole and grows from the bottom SRO layer upwards. The side wall is not exactly vertical to the substrate: this is because during the FIB cutting process, the ions move in and out of the hole positions, resulting in an angular cut of the thin film layers. After CFO deposition, the holes were filled but maintained their original shape.

Figure 5.4 shows the piezoelectric response results for the BFO phase. Part (a) shows a PFM image for a poled CFO-BFO nano-array structure. The structure was first poled by -8 V in a 6μm×6μm area using the AFM tip, and then subsequently by +8 V in a 3.5μm×3.5μm area within the center of the prior square. One can see that the center area is bright (or yellow) while the outer area looks darker (or orange). Part (b) shows a schematic cut of the nano-array structure. The yellow part represents the BFO film where +8 V has been applied, while the orange part represents the BFO film under -8 V. One can see that the reverse electric field results in a switching of the polarization direction in the BFO layer. During the PFM measurements, the area under positive field responded oppositely to an ac electric signal applied by the tip relative to the chuck, giving rise to a contrast in the PFM image as shown in Part (a). In this image, it can also be seen that the CFO nano-arrays did not respond to the ac electric signal: clearly evidencing that the CFO phase is not piezoelectric in nature, as expected.

A line scan of the piezoresponse across the CFO-BFO nano-array taken from the PFM image is shown in Part (c). The BFO portions under +8V and -8V are as indicated. One can

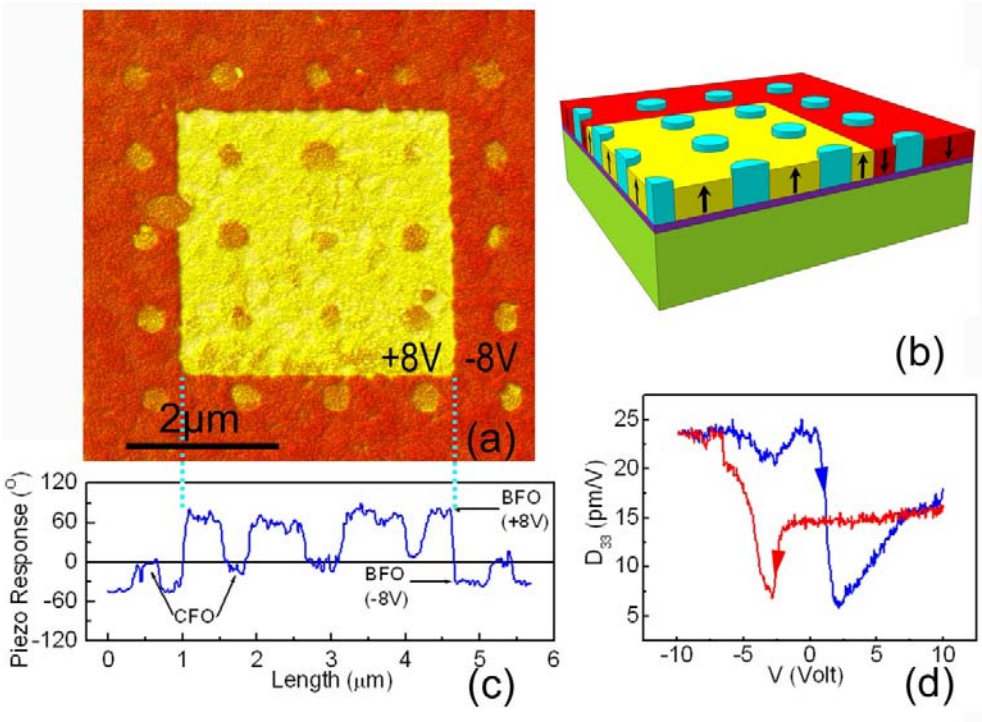

Figure 5.4 Piezoelectric properties of ordered CFO-BFO composite thin films. (a) PFM results of CFO-BFO composite films, where the thin film is poled by -8V in a 6μm×6μm area, and then by -8V in a 3.5μm×3.5μm area; (b) schematic illustration of ferroelectric domain in CFO-BFO composite thin film; (c) a line scan taken from the PFM image showing the piezo-response in different regions; and (d) d_{33} of the BFO phase as a function of applied voltage.

clearly see that the responses from the BFO areas under positive and negative voltages are opposite to each other. Furthermore, a careful observation indicates that the phase angle for the +8 V BFO region is around 65 degrees, while for the -8 V BFO region is about -45 degrees: i. e. there is an asymmetry in the BFO polarization response between positive and negative signs of fields. The response from the CFO nano-rod regions remained close to zero, as expected for a non-piezoelectric phase.

The longitudinal piezoelectric coefficient d_{33} for the BFO matrix as a function of applied voltage is shown in Part (d), both positive-to-negative and negative-to-positive voltage sweeps are given. In this figure, one can clearly see the asymmetry in the d_{33} vs. E loop. The value of d_{33} is 15 pm/V under voltages > +8V, and 25pm/V under voltages < -8V. Such an asymmetry between forward and reverse fields originates from the constraint of the substrate on the BFO film, and the accumulation of defects at the interface between film and substrate: the elastic strain of the BFO phase when acted against the substrate is clamped. Because of this compromised situation, the piezo-response (see Fig. 5.4c-d) of the BFO phase is smaller under positive voltage compared to negative. Even after switching off the voltage, the remnant d_{33} remained nearly at the saturation value. This fact will play a crucial role during our PFM and MFM measurements of the magneto-electric response, as the same tip can then be used for application of voltage as for measurement.

Figure 5.5 shows the magnetic response results for the CFO nano-rod phase. Parts (a) and (b) show the MFM images of CFO-BFO nano-array structure magnetized by external magnetic fields of -6 kOe and +6 kOe, respectively. The CFO areas had a dark contrast under -6 kOe, indicating downward orientation of the magnetization. Under +6 kOe, the CFO areas exhibited a

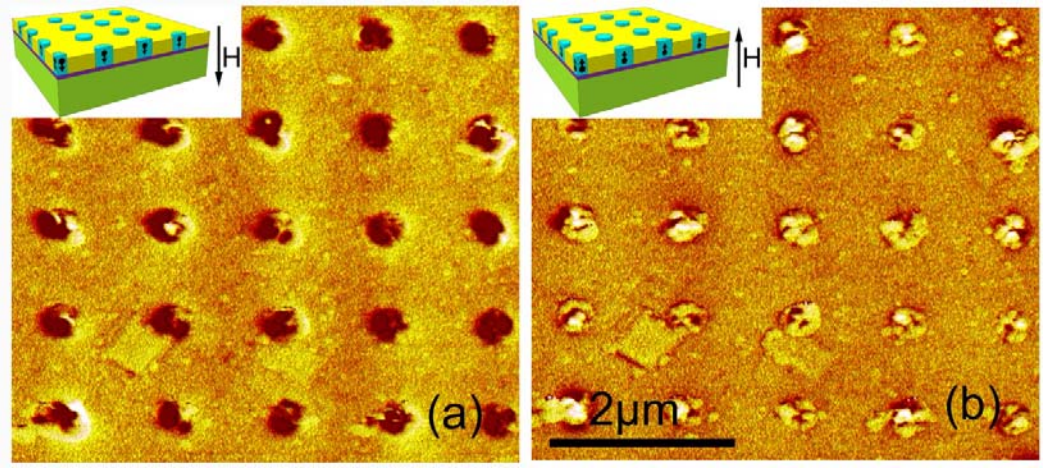

Figure 5.5 MFM images of the ordered CFO-BFO composite thin films under magnetic fields of (a) -6 kOe and (b) +6 kOe. The inserts show schematics of the CFO spin and magnetic field directions.

bright contrast, indicating that the magnetization is oriented upwards from the plane of the film. The schematic diagrams in the inserts of Parts (a) and (b) illustrate this switching of the CFO magnetization. The changes in contrast observed in our MFM images demonstrate that the magnetization orientation of the CFO nano-rods rotates under applied magnetic field. Furthermore, one does not see any noticeable change in the MFM images in the areas of the BFO matrix, even though the BFO phase is a canted antiferromagnet with a small effective magnetic moment. Since the saturation magnetization for a 200 nm thick BFO layer is much smaller than that for the ferrimagnetic CFO phase [24], the inversion in magnetization is much more clear for the CFO array than the BFO matrix.

Finally, we studied the magneto-electric response of the ordered CFO-BFO nano-array structure by MFM. A magnetic field of +6 kOe was applied in the out-of-plane direction to magnetize the CFO phase. Positive and negative voltages were applied across the BFO phase through the MFM tip. We then performed two sets of experiments with different voltage application schemes to rigorously study the ME effect. Figure 5.6 shows the results for both measurement sets. Images (a), (b), and (c) show representative results from the first measurement set which was taken under voltages of 0, -6, and +6V applied across a 5μm×5μm area of the BFO matrix, respectively. One can see that the CFO array appears bright in (a), which is indicative that the magnetization direction points upwards from the phase nearby. Under -6 V, the CFO array has an even brighter contrast in the image, as seen from (b). However when the sign of voltage was reversed to -6V in (c), the CFO arrays appeared much darker, indicating that the magnetization orientation has been rotate towards the in-plane direction. These results clearly demonstrate that the CFO magnetization orientation is affected by application of voltage across

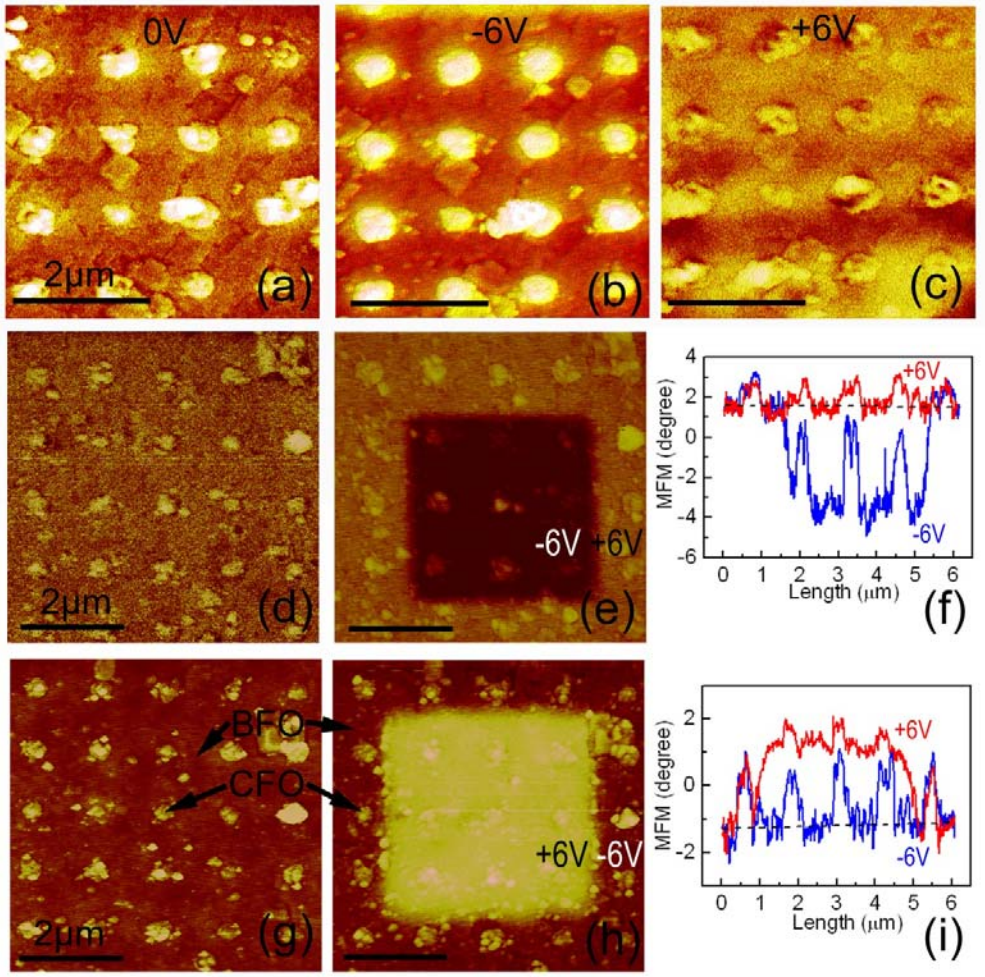

Figure 5.6 MFM results for ordered CFO-BFO composite thin film before/after applying an electric field. First set of MFM results were obtained by applying voltages of (a) 0V, (b) -6V and (c) +6V to the films. The second set of MFM results were obtained by applying voltages of (d) +6V and (e) -6V to the center; (f) line scan taken from (e) showing how the magnetization in different regions is changed by voltage. The third set of MFM results were obtained by applying voltages of (g) -6V and (h) +6V in the center; and (i) line scan taken from (h) showing how the magnetization in different regions is changed by voltage.

the BFO phase; or in other words that there is a ME coupling between the magnetic and electric phases in our ordered BFO-CFO nano-array structure.

To obtain a better understanding of the magneto-electric phenomena, we next performed a second set of MFM experiments. In a 6μm×6μm area, we applied +6 V using the MFM tip (see Part (d)), and then subsequently applied -6 V in a 3.5μm×3.5μm area at the center of the prior square (see Part (e)). Part (f) shows line profiles extracted from the MFM images of the CFO-BFO nano-array obtained under positive and negative voltages, as indicated. In these line scans, one can see under +6 V that there are small humps at regular intervals which are indicative of magnetic contrast from the CFO nano-array. However for the line scan obtained under -6 V applied to the smaller square, the contrast signal from the BFO matrix was reduced and the humps from the CFO became much clearer. It should be noted that the amplitude of the CFO signal was also decreased some, indicating a slight rotation of the magnetization away from the saturation direction normal to plane of the film under negative voltage. The decrease in the BFO matrix signal can be attributed to polarization switching on reversal of the sign of the electric field.

Then, for the second set of MFM images, we reversed the voltage scheme and first applied -6 V to the larger 6μm×6μm area, and then +6 V to the smaller 3.5μm×3.5μm center area. Parts (g) and (h) show these MFM images, respectively. Part (i) shows representative line scans taken from the array. For the line scan under –6V, one can see humps from the CFO nano-rods. Then, under +6V, the line scan shows that the amplitudes of both the CFO and BFO signals were increased. These results demonstrate an increase in the CFO magnetization on switching the sign of the voltage. Please note that the MFM contrast of brightness or darkness from the CFO phase is relative to that of the BFO matrix. Accordingly, in Part (b) under -6 V, even

though the CFO magnetization decreases, one observes a brighter CFO line profile due to a significantly lower intensity for the BFO matrix. In consideration that the CFO array was initially magnetized in the upwards direction normal to the plane of the film, we can understand the difference in changes of magnetization under positive vs negative voltage as follows. The ME exchange mediated by the strictive interactions between BFO and CFO is quadratic with magnitude of the field. Thus, even though we can switch the orientation of the spontaneously polarization under electric field, we not switch that of the magnetization by 180° (i.e., + to -) but rather only reorient it by less than 90°. These results are consistent with the quadratic ME coupling of heterostructured layers not being able to achieve time inversion of the magnetization under electric field.

The change in the CFO magnetization with electric field applied across the BFO matrix demonstrates a strain mediated ME coupling between the magnetostrictive and piezoelectric phases, consistent with the concepts expressed in the schematics of Fig. 5.2. As one applies a positive voltage, the BFO phase expands following the d_{33} data shown in Fig. 5.4 (d). Accordingly, the electric-field-induced-strain is transmitted to the adjacent CFO nano-rod phase which it is coherent with, resulting in a change in the magnetization as evidenced in Figs. 5.6 (a) and (b). Negative voltages result in a larger strain in BFO than positive voltages, as shown in Fig. 5.4 (d). This results in a higher elastic strain in the CFO arrays, decreasing the CFO magnetization as shown in Figs. 5.6 (f) and (i). It should be noted that the ME coupling between the CFO and BFO phases might be more complicated than the mechanism described above, as it will depend on the direction that the respective magnetic and electric fields are applied (i.e., clamping) and on the how the CFO magnetostriction and BFO piezo strains depend on the fields (i.e., nonlinearities) [94, 173].

5.4 Summary

In summary, we have prepared ordered magneto-electric nano-array structures by a combination of pulsed laser deposition and focused ion beam etching techniques. The structures are comprised of magnetostrictive CFO nano-structures embedded in a piezoelectric BFO matrix. Magnetic force microscopy images clearly showed a control of the CFO magnetization under electric fields applied across the BFO phase. This is the first demonstration of ME coupling between magnetic and electric phases in a highly ordered structure: which is a structure that should be of immense potential for data storage, sensors, logic and communication device applications. We hope these results will stimulate research activities on ordered magneto-electric heterostructures.

Chapter 6: Conclusions and Future Work

6.1 Conclusion

In this dissertation, I have performed systematic investigations of the crystal structure, nano-structure, ferroelectric properties, ferromagnetic properties, and magnetoelectric properties of ferroelectric ($Pb(Fe_{1/2}Nb_{1/2})O_3$, $Pb(Zr_{0.52}Ti_{0.48})O_3$, $BiFeO_3$) epitaxial thin films, and multiferroic ($BaTiO_3$-$CoFe_2O_4$ and $BiFeO_3$-$CoFe_2O_4$) composite thin films. The experimented methods that I have used include x-ray diffraction, scanning force microscopy, SQUID, and other measuring systems that were in the laboratory. The main findings can be summarized as follows:

- Epitaxial lead iron niobate thin films with thicknesses of 50nm<t<500nm have been deposited by pulsed laser deposition (PLD). I have identified the deposition conditions that result in insulating layers. These critical conditions are essential to (i) prevent semi-conducting resistivity characteristics; (ii) achieve higher induced polarizations of 70μC/cm^2 under E=190kV/mm; and (iii) obtain remnant polarizations of 17.7μC/cm^2, coercive fields of 9.5kV/mm, and dielectric constants of ~1200 at room temperature.
- The lattice structure has been studied for variously oriented lead iron niobate (PFN) thin films with thicknesses of 50<t<500nm that were deposited by pulsed laser deposition (PLD). I have identified that (001), (110), and (111) oriented PFN thin films have tetragonal, orthorhombic, and rhombohedral phases at room temperature, respectively. The change in phase stability, when deposited on substrates of different orientations, is discussed with respect to the influence of epitaxial stress.

- Multiferroic properties have been studied for $Pb(Fe_{1/2}Nb_{1/2})O_3$ (or PFN) epitaxial thin-layers grown on (001), (110), and (111) $SrTiO_3$ substrates, with and without a $SrRuO_3$ buffer. My findings are as follows: (i) the constraint stress on (001) substrates is >10x larger than that on (110) and (111); (ii) this large constraint stress induces higher piezoelectric constants, magnetic permeability and magnetization for (001) PFN compared with (110) and (111) layers; (iii) epitaxy distorts the structure of (001) PFN causing the films to be weakly ferromagnetic, whereas (110) films are antiferromagnetic; and (iv) a significant increase of the coercivity of (001) layers occurs due to clamping by a SRO buffer layer.
- The structural and ferroelectric properties have been studied for $Pb(Zr_{0.52}Ti_{0.48})O_3$ (PZT) epitaxial thin films grown on (001), (110), and (111) $SrRuO_3/SrTiO_3$ substrates by pulsed laser deposition. A monoclinic C (M_c) phase has been found for (101) films; whereas (001) and (111) ones were tetragonal (T) and rhombohedral (R), respectively. I found that the ferroelectric polarization of the M_c phase is higher than that in either the T or R ones. These results are consistent with predictions (i) of epitaxial phase diagrams, and (ii) that the enhanced ferroelectric properties of morphotropic phase boundary PZT are related to a low symmetry monoclinic phase.
- A triclinic phase has been observed in perovskite $BiFeO_3$ (BFO) epitaxial thin films grown on (130) and (120) oriented $SrTiO_3$ substrates. The lattice constants of the BFO thin films changed with tilt of the substrates: from (001) towards (110). These lattice parameters result from the epitaxially engineering of structurally bridging phases of the lowest possible symmetry.

- A nano-belt structure along the <110> direction has been observed in perovskite-spinel ($BiFeO_3$-$CoFe_2O_4$ or BFO-CFO) composite epitaxial thin films deposited on $SrTiO_3$ (STO) substrates by pulsed laser deposition. The results reveal the nucleation and growth mechanism of the nano-structure: first nucleation of perovskite phase regions on STO, followed by segregation of spinel out of the perovskite phase, and finally by evolution of spinel nano-belts that are elongated along the <110>. The reason for control of the nano-structure evolution is a ledge growth mechanism of spinel along the <110> direction.
- A nano-belt structure oriented along the <110> direction has been observed in perovskite-spinel ($BaTiO_3$-$CoFe_2O_4$ or BTO-CFO) composite epitaxial thin films deposited on (001) $SrTiO_3$ (STO) substrates by pulsed laser deposition. The effects of annealing, ramp rate, and buffer layers on the nano-structure growth process were studied by atomic force microscopy and x-ray diffraction. The magnetization of BTO-CFO nano-belt thin films was also compared with that of BTO-CFO nano-pillar and CFO monolayer thin films.
- The ferroelectric (FE), ferromagnetic (FM), and magnetoelectric (ME) properties of self-assembled epitaxial $BiFeO_3$-$CoFe_2O_4$ (BFO-CFO) nano-structure composite thin films have been studied which are deposited on (001), (110), and (111) $SrTiO_3$ (STO) single crystal substrates. These various properties are shown to depend on orientation. The maximum values of the relative dielectric constant, saturation polarization, longitudinal piezoelectric coefficient, saturation magnetization, and ME coefficient at room temperature were 143, 86μm/cm^2, 50pm/V, 400emu/cc, and 20mV/cm·Oe, respectively.
- An ordered $CoFe_2O_4$ nano-array embedded in $BiFeO_3$ matrix was deposited by pulsed laser deposition method, assisted by a focused ion beam using Al_2O_3 as a sacrifice layer.

Using this method, it is possible to control the nano-structure in oxide composite thin films, as each phases can be deposited at their best deposition condition. Results of piezoresponse force and magnetic force microscopies exhibited good ferroelectric and ferromagnetic properties for the $BiFeO_3$ and $CoFe_2O_4$ phases, respectively. Magnetoelectric coupling between two phases was also observed by magnetic force microscopy.

6.2 Recommendations for future work

- $Pb(Fe_{1/2}Nb_{1/2})O_3$ (or PFN) epitaxial thin-layers grown on $SrTiO_3$ substrates are good multiferroic thin films. The values for the polarization and magnetization can reach $70\mu C/cm^2$ and 80Emu/cc, respectively. The ferroelectric Curie temperature is about 385K, at which temperature there is a phase change from paraelecric to ferroelectric. However, the antiferromagnetic Neel temperature at which a transformation occurs from paramagnetic to antiferromagnetic occurs around 140K, which is much lower than room temperature. The lower Neel temperature prevents the further application of this material. In order to increase the Neel temperature, PFN could be doped with $BiFeO_3$, whose Neel temperature is about 640K. The Neel temperature of PFN-BFO could be adjusted by increasing the volume ratio of BFO materials to be just near room temperature.
- A triclinic phase has been observed in perovskite $BiFeO_3$ (BFO) epitaxial thin films grown on (130) and (120) oriented $SrTiO_3$ substrates. Monoclinic A and monoclinc B were also observed in (001) and (110) orientated BFO epitaxial thin film in the reports. $PbTiO_3$ is tetragonal ferroelectric at room temperature. New phases might be observed when $PbTiO_3$ deposited on (130), (120) and other low-symmetry oriented substrates. A

systematic study of the classic material $PbTiO_3$ deposited on variously oriented substrate would be an interesting topic for future research, which could more fully elucidate the generic nature of my approach.

- Ordered $CoFe_2O_4$ nano-arrays embedded in a $BiFeO_3$ matrix have been deposited by PLD, assisted by Focused Ion Beam using Al_2O_3 as a sacrifice layer. However, the area of the ordered CFO-BFO was only 20μm × 20μm. It is necessary to deposit regular CFO-BFO nano-arrays over a larger area. Using a conventional lithographic method, one could pattern a larger area on top of the thin layers. Hydrofluoric acid could be used to etch regular hole-arrays in $Al_2O_3/BiFeO_3$ thin films. After the photo resist is removed, a large area with ordered hole-array would be formed. The rest of the process flow would be similar to that used in Chapter 5 of this thesis.
- $BiFeO_3$-$CoFe_2O_4$ composite thin films having a (1-3) self-assembled nano-structure and a (2-2) layered structure were both systematically studied. If the (1-3) nano-structure layer could be sandwiched between (2-2) layers, then several new composite thin films structures with unique phase connectivities could be deposited: such as (0-3), (3-0), (2-3), and (3-2). New ferroelectric, ferromagnetic, and magnetoelectric properties might be anticipated using such composite thin films, with unique type of phase distributions.

REFERENCE

1. P. Curie , J Phys 3, 393 (1894).

2 I. E. Dzyaloshinshii , Zh Eksp Teor Fiz 37, 881 (1959).

3 D. N. Astrov, Zh Transl Soviet phys 11, 708 (1960).

4 G. T. Rado, and V. J. Folen, Phys Rev Lett 7, 310 (1961).

5 L. D. Landau and E. M. Lisfshitz, Addison-Wesley Co., Inc., Reading, Mass., (1960)

6 van Run, A. M. J. G., Terrell, D. R. & Scholing, J. H., J. Mater. Sci. 9, 1710 (1974).

7 H. Schmid, Ferroelectrics 162, 317 (1994).

8 S. X. Dong, J. F. Li and D. Viehland, Applied Physics Letters 83, 2265 (2003).

9 S. X. Dong, J. F. Li and D. Viehland, IEEE Transaction son Ultrasonics Ferroelectrics and Frequency Control 50, 1253 (2003).

10 S. X. Dong, J. R. Cheng, J. F. Li and D. Viehland, Applied Physics Letters 83, 4812 (2003).

11 H. Wiegelmann, A. A. Stepanov, I. M. Vitebsky, A. G. M. Janseb and P. Wyder, Phys. Rev. B 49, 10039 (1994).

12 J. P. Rivera and H. Schmid, J. Appl. Phys. 70, 6410 (1991).

13 A. M. Kadomtseva, A. K. Zvezdin, Y. F. Popov, A. P. Pyatakov and G. P. Vorobev, JETP Lett. 79, 571 (2004).

14 Z. J. Huang, Y. Cao, Y. Y. Sun, Y. Y. Xue and C. W. Chu, Phys. Rev. B 56, 2623 (1997).

15 Y. Yang, J. M. Liu, H. B. Huang, W. Q. Zou, P. Bao and Z. G. Liu, Phys. Rev. B 70, 132101 (2004).

16 C. W. Nan, Physical Review B 50, 6082 (1994).

17 J. Ryu, A. V. Carazo, K. Uchino and H. E. Kim, J. Electroceramics 7, 17 (2001).

18 C. W. Nan, M. Li and J. H. Huang, Physical Review B 63, 144415 (2001).

19 C. W. Nan, L. Liu, N. Cai, J. Zhai, Y. Ye, Y. H. Lin, L. J. Dong and C. X. Xiong, Applied Physics Letters 81, 3831 (2002).

20 G. Srinivasan, E. T. Rasmussen and R. Hayes, Physical Review B 67, 014418 (2003).

21 S. X. Dong, J. F. Li and D. Viehland, Applied Physics Letters 85, 5305 (2004).

22 S. X. Dong, J. F. Li and D. Viehland, Journal of Applied Physics 95, 2625 (2004).

23 K. J. Choi, M. Biegalski, Y. L. Li, A. Sharan, J. Schubert, R. Uecker, P. Reiche, Y. B. Chen, X. Q. Pan, V. Gopalan, L. Q. Chen, D. G. Schlom, and C. B. Eom, Science 306, 1005 (2004).

24 J. Wang, J. B. Neaton, H. Zheng, V. Nagarajan, S. B. Ogale, B. Liu, D Viehland, V. Vaithyanathan, D. G. Schlom, U. V. Waghmare, N, A. Spadlin, K. M. Rabe, M. Wuttig, and R. Ramesh, Science 299, 1719 (2003).

25 J. Wang, A. Scholl, H. Zheng, S. B.Ogale, D. Viehland, D. G. Schlom, N. A. Spaldin, K. M. Rabe, M. Wuttig, L. Mohaddes, J. Neaton, U. Waghmare, T. Zhao and R. Ramesh, Science 307, 1203b (2005)

26 H. Zheng, J. Wang, S. E. Lofland, Z. Ma, L. Mohaddes-Ardabili, T. Zhao, L. Salamanca-Riba, S. R. Shinde, S. B. Ogale, F. Bai, D. Viehland, Y. Jia, D. G. Gchlom, M. Wuttig, A. Roytburd and R. Ramesh, Science 303, 661 (2004).

27 H. Wiegelmann, I. M. Vitebsky, and A. A. Stepanov, Physical Review B 55, 15304 (1997).

28 B. B. Van Aken, T. T. M. Palstra, A. Filippetti, and N. A. Spaldin, Nature Materials 3, 164 (2004).

29 T. Kimura and S. Kawamoto, I Yamada, M. Azuma, M. Takano, and Y. Tokura, Physical Review B 67, 180401 (2003).

30 G. A. Smolenskii, A. Agranovskaya, S. N. Popov, and V. A. Isupov, Sov. Phys. Tech. Phys. 28, 2152 (1958).

31 V. A. Vokov ed al., Sov. Phys. JETP 15, 447 (1962).

32 Y. Yang, S. T. Zhang, H. B. Huang, Y. F. Chen, Z. G. Liu, and J. M. Liu, Materials Letters 59, 1767 (2005).

33 G. L. Platonov, L. A. Drobyshev, Y. Y. Tomashpolskii, and Y. N. Venevtsev, Sov. Phys. Crystallogr. 14, 692 (1970).

34 T. Watanabe, and K. Kohn, Phase Trans. 15, 57 (1989).

35 V. V. Bhat, K. V. Ramanujachary, S. E. Lofland, and A. M. Umarji, Journal of Magnetism and Magnetic Materials 280, 221 (2004)

36 D. Viehland, Journal of Applied Physics 88, 4794 (2000)

37 D. Viehland, S. J. Jang, L. E. Cross, and M. Wuttig, Journal of Applied Physics 69, 414 (1991).

38 O. Raymond, R. Font, N. Suárez-Almodovar, J. Portelles, and J. M. Siqueiros, Journal of Applied Physics 97, 084107 (2005).

39 M. Sedlar, and M. Sayer, J. Appl. Phys. 80, 372 (1996).

40 Q. Lin, G. Yi, and D. Barber, Materials Letters 38, 239 (1999).

41 X.S. Gao, X.Y. Chen, J. Yin, J. Wu, Z.G. Liu, and M. Wang, Journal of Materials Science 35, 5421 (2000).

42 X. R. Wang, S. S. Fan, Q. Q. Li, B. L. Gu, and X. W. Zhang, Jpn. J. Appl. Phys. 35, L1002 (1996).

43 B. Jaffe, W. R. Cook, and H. Jaffe, Piezoelectric Ceramics, 136 (1971).

44 B. Noheda, D. E. Cox, G. Shirane, J. A. Gonzalo, L. E. Cross, and S. E. Park, Applied Physics Letters 74, 2059 (1999).

45 B. Noheda, J. A. Gonzalo, L. E. Cross, R. Guo, S. E. Park, D. E. Cox, and G. Shirane, Physical Review B 61, 8687 (2000).

46 B. Noheda, D. E. Cox, G. Shirane, R. Guo, B. Jones, an L. E. Cross, Physical Review B 63, 014103 (2000).

47 H. Fu, and R. E. Cohen, Nature 403, 281 (2000).

48 B. Noheda, D. E. Cox, G. Shirane, S. E. Park, L. E. Cross, and Z. Zhong, Physics Review Letters 86, 3891 (2001).

49 J. M. Kiat, Y. Uesu, B. Dkhil, M. Matsuda, C. Malibert, and G. Calvarin, Physics Review B 65, 064106 (2002).

50 H. Cao, J. Li, D. Viehland, and Guangyong Xu, Physical Review B 73, 184110 (2006).

51 N. A. Pertsev, V. G. Kukhar, H. Kohlstedt, and R. Waser, Physical Review B 67, 054107 (2003).

52 J. Li, J. Wang, M. Wuttig, R. Ramesh, N. Wang, B. Ruette, A. P. Pyatakov, A. K. Zvezdin, and D. Viehland, Applied Physics Letter 25, 5261 (2004).

53 G. Xu, H. Hiraka, G. Shirane, J. Li, J. Wang, and D. Viehland, Applied Physics Letters 86, 182905 (2005).

54 S.V. Kiselev, R. P. Ozerov, and G. S. Zhdanov, Sov. Phys. Sokl, 7, 742 (1963).

55 G. A. Smolenskii and I. Chupis, Sov. Phys. Usp. 25, 475 (1982).

56 E. K. H. Salje, Phase Transitions in Ferroelastic and Co-elastic Crystals (Cambridge University Press, Cambridge, England, (1990).

57 Yu. E. Roginskaya, Yu. Ya. Tomashpol'skii, Yu. N. Venevtsev, V. M. Petrov, and G. Zhdanov, Sov. Phys. JETP 23, 47 (1966).

58 Yu. N. Venevtsev, G. Zhdanov, and S. Solov'ev, Sov. Phys. Crystallogr. 4, 538 (1960).

59 G. A. Smolenskii, V. Isupov, A. Agranovskaya, and N. Krainik, Sov. Phys. Solid State 2, 2651 (1961).

60 P. Fisher, M. Polomskya, I. Sosnowska, and M. Szymansksi, J. Phys. C 13, 1931 (1980).

61 G. A. Smolenskii, V. Yudin, E. Sher, and Yu. E. Stolypin, Sov. Phys. JETP 16, 622 (1963).

62 C. Michel, J.-M. Moreau, G. D. Achenbach, R. Gerson, and W. J. James, Solid State Commun. 7, 701 (1969).

63 J. D. Bucci, B. K. Robertson, and W. J. James, J. Appl. Crystallogr. 5, 187 (1972).

64 J. R. Teague, R. Gerson, and W. J. James, Solid State Commun. 8, 1073 (1970).

65 I. Sosnowska, T. Perterlin-Neumaier, and E. Steichele, J. Phys. C 15, 4835 (1982).

66 J.F. Li, Junling Wang, M. Wuttig, R. Ramesh, N. Wang, B. Ruette, A. P. Pyatakov, A. K. Zvezdin, and D. Viehland, Appl. Phys. Lett. 84, 5261 (2004).

67 G. Xu, H. Hiraka, G. Shirane, J. Li, J. Wang, and D. Viehland, Appl. Phys. Lett. 86, 182905 (2005).

68 G. Xu, J. Li and D. Viehland, Appl. Phys. Lett. 89, 222901 (2006).

69 S.-E. Park and T. R. Shrout, J. Appl. Phys. 82, 1804 (1997).

70 S. F. Liu, S-E. Park, T. R. Shrout, and L. E. Cross, J. Appl. Phys. 85, 2810 (1999).

71 D. La-Orauttapong, B. Noheda, Z. G. Ye, P. M. Gehring, J. Toulouse, D. E. Cox, and G. Shirane, Phys. Rev. B 65, 144101 (2002).

72 B. Noheda, Z. Zhong, D. E. Cox, G. Shirane, S. E. Park, and P. Rehrig, Phys. Rev. B 65, 224101 (2002).

73 K. Ohwada, K. Hirota, P. Rehrig, Y. Fujii, and G. Shirane, Phys. Rev. B 67, 094111 (2003).

74 Z. G. Ye, B. Noheda, M. Dong, D. Cox, and G. Shirane, Phys. Rev. B 64, 184114 (2001).

75 B. Noheda, D. E. Cox, G. Shirane, J. Gao, and Z. G. Ye, Phys. Rev. B 66, 054104 (2002).

76 H. Cao, F. Bai, N. Wang, J. Li, D. Viehland, G. Xu, and G. Shirane, Phys. Rev. B 72, 064104 (2005).

77 K. Saito, A. Ulyanenkov, V. Grossmann, H. Ress, L. Bruegemann, H. Ohta, T. Kurosawa, S. Ueki, and H. Funakubo, Jap. J. Appl. Phys. 45, 7311 (2006).

78 Zheng, H. Zhan, Q. Zavaliche, F. Sherburne, M. Straub, F. Cruz, M. O. Chen, L. Q. Dahmen, U. Ramesh, R. Nano Letters 6, 1401 (2006).

79 Zheng, H. Straub, F. Zhan, Q. Yang, P. L. Hsieh, W. K. Zavaliche, F. Chu, Y. H. Dahmen, U. Ramesh, R. Advanced Materials 18, 2747 (2006).

80 Zheng, H. Wang, J. Mohaddes-Ardabili, L. Wuttig, M. Salamanca-Riba, L. Schlom, D. G. Ramesh, R. Applied Physics Letters 85, 2035 (2004).

81 Zheng, H. Kreisel, J. Chu, Y. H. Ramesh, R. Salamanca-Riba, L. Applied Physics Letters 90, 113113 (2007).

82 Zhan, Q. Yu, R. Crane, S. P. Zheng, H. Kisielowski, C. Ramesh, R. Applied Physics Letters 89, 172902 92006).

83 Levin I. Li, J. Slutsker, J. Roytburd, A. Advanced Materials 18, 2044 (2006).

84 Li J. Levin, I. Slutsker, J. Provenzano, V. Schenck, P. K. Ramesh, R. Ouyang, j. Roytburd, A. L. Applied Physics letters 87, 072909 (2005).

85 Slutsker, J. Levin, I. Li, J. Artemev, A. Roytburd, A. L. Physical Review B 73, 184127 (2006).

86 Murakami, M. Chang, K. S. Aronova, M. A. Lin, C. L. Yu, M. H. Hattrick Simpers, J. Gao, C. Hu, B. Lofland, S. E. Knauss, L. A. Bendersky, L. A. Applied Physics Letters 87, 112901 (2005).

87 Chang, K. S. Aronova, M. A. Lin, C. L. Murakami, M. Yu, M. H. Hattrick-Simpers, j. Famodu, O. O. Lee, S. Y. Ramesh, R. Wuttig, M. Takeuchi, I. Gao, C. bendersky, L. A. Applied Physics Letters 84, 3091 (2004).

88 Ryu, H. Murugavel, H. Lee, J. H. Chae, S. C. Noh, T. W. Oh, Y. S. Kim, H. J. Kim, K. H. Jang, J. H Kim, M. Bae, C. Park, J. G. Applied Physics Letters 89, 102907 (2006).

89 Wan, J. G. Zhang H. Wang X. W. Pan, D. Liu, J. M. Wang G. Applied Physics Letters 89, 122914 (2006).

90 Wan, J. G. Wang, X. W. Wu, Y. J. Zeng, M. Wang, Y. Jiang, H. Zhou, W. Q. Wang, G. H. Liu, J. M. Applied Physics Letters 86, 122501 (2005).

91 He, H. C. Zhou, J. P. Wang, J. Nan, C. W. Applied Physics Letters 89, 052904 (2006).

92 Zhou, J. P. He, H. C. Shi, Z. Nan, C. W. Applied Physics Letters 88, 013111 (2006).

93 Zavaliche, F. Zhao, T. Zheng, H. Straub, F. Cruz, M. P. Yang, P. L. Hao, D. Ramesh, R. Nano Letters 7, 1586 (2007).

94 Zavaliche, F. Zheng, H. Mohaddes-Ardabili, L. Yang, S. Y. Zhan, Q. Shafer, P. Reilly, E. Chopdeka, R. Jia, Y. Wright, P. Schlom, D. G. Suzuki, Y. Ramesh, R. Nano Letters 5, 1793 (2005).

95 Zhao, T. Scholl, A. Zavaliche, F. Zheng, H. Barry, M. Doran, A. Lee, K. Cruz, M. P. Ramesh, R. 90, 123104 (2007).

96 Nan, C. W. Liu. G. Lin, Y. Physical Review Letters, 94, 197203 (2005).

97 J. S. Speck, A. Selfert W. Pompe and R. Ramesh J., Appl. Phys. 76, 477 (1994).

98 J. Lee, G. Park, C. Park and H. Kim, Applied Physics Letters 88, 072908 (2006).

99 F. Hsu, C. Leu, Y. Lu, S. Ho and C. Hu, J. Am. Ceram. Soc. 92, 389 (2009).

100 J. W. Matthews and A. E. Blakeslee J. Cryst. Growth 27, 118 (1974).

101 R. People and J. C. Bean Applied Physics Letters 47, 322 (1985).

102 Y. B. Chen, H. P. Sun, M. B. Katz, X. Q. Pan, K. J. Choi, H. W. Jang and C. B. Eom Applied Physics Letters 91, 252906 (2007).

103 G. F. Huang and S. Berger Journal of Applied Physics 93, 2855 (2003).

104 S. P. Alpay, I. B. Misirlioglu, A. Sharma and X. G. Ban Journal of Applied Physics 95, 8118 (2004).

105 O. Trithaveesak, J. Schubert and Ch. Buchal Journal of applied Physics 98, 114101 (2005).

106 A. Petraru, N. A. Pertsev, H. Kohlstedt, U. Poppe, R. Waser, A. Solbach and U. Klemradt Journal of Applied Physics 101, 114106 (2007).

107 V. Nagarajan, I. G. Jenkins, S. P. Alpay, H. Li, S. Aggarwal, L. Salamanca-Riba, A. L. Roytburd and R. Ramesh Journal of Applied Physics 86, 595 (1999).

108 D. M. Kim, C. B. Eom, V. Nagarajan, J. Ouyang, R. Ramesh, V. Vaithyananthan and D. G. Schlom Applied Physics Letters 88, 142904 (2006).

109 K. Saito, A. Ulyanenkov, V. Grossmann, H. Ress, L. Bruegemann, H. Ohta, T. Kurosawa, S. Ueki and H. Funakubo Janpanese Journal of Applied Physics 45, 7311 (2006).

110 J. S. Speck, A. C. Daykin, A. Seifert, A. E. Romanov and W. Pompe J. Appl. Phys. 78, 1696 (1995).

111 S. P. Alpay and A. L. Roytburd J. Appl. Phys. 83, 4714 (1998).

112 B. Tuttle, T. Headley, C. Drewien, J. Michael, J. Voigt and T. Garino Ferroelectrics 221, 209 (1999).

113 K. S. Lee, J. H. Choi, J. Y. Lee and S. Baik J. Appl. Phys. 90, 4095 (2001).

114 K. J. Choi, M. Biegalski, Y. L. Li, A. Sharan, J. Schubert, R. Uecher, P. Reiche, Y. B. Chen, X. Q. Pan, V. Gopalan, L. Q. Chen, d. G. Schlom, C. B. Eom Science 306, 1005 (2004).

115 L. Yan, J. F. Li, C. Suchicital, and D. Viehland, Applied Physics letters 89, 132913 (2006).

116 V. Bonny, M. Bonin, P. Sciau, K. J. Schenk, and G. Chapuis, Solid State Communications 102, 347 (1997).

117 F. W. Lytle, Jounal of Applied Physics 35, 2212 (1964).

118 K. Itoh, K. Ochiai, H. Kawaguchi, C. Moriyoshi, and E. Nakamura, Feroelectrics 159, 85 (1994).

119 D. de Ligny and P. Richet, Physcial Review B 53, 3013 (1996).

120 M. Yokosuka, Jpn. J. Appl. Phys. 32, 1142 (1993).

121 M. V. Radhika Rao and A. M. Umarji, Materials Research Bulletin 30, 1031 (1995).

122 V. V. S. S. Sai Sunder and A. M. Umarji, Materials Research Bulletin 30, 427 (1995).

123 K. Motida, and S. Miyahara, Journal of the physical society of Japan 28, 1188 (1970).

124 G. A. Sawatzky, W. Geertsma, and C. Haas, Journal of magnetism and magnetic materials 3, 37 (1976)

125 J. Kanamori, J. phys. Chem. Solids 10, 87 (1959).

126 J. B. Goodenough, Physical Review 100, 564 (1955).

127 C. M. Foster, G. R. Bai, R. Csencsits, J. Vetrone, R. Jammy, L. A. Wills, E. Carr, and Jun Amano, Journal of Applied Physics 81, 2349 (1997).

128 S. Yokoyama, Y. Honda, H. Morioka, S. Okamoto, H. Funakubo, T. Iijima, H. Matsuda, K. Saito, T. Yamamoto, H. Okino, O. Sakata, and S. Kimura, Journal of Applied Physics 98, 094106 (2005).

129 H. Cao, J. Li, D. Viehland, G. Xu, G. Shirane, Applied Physics Letters 88, 072915 (2006).

130 J. Ryu, A. V. Carazo, K. Uchino, H. E. Kim, Japanese Journal of Applied Physics Part 1 40, 4948 (2001).

131 J. Ryu, S. Priya, K. Uchino, H. E. Kim, Journal of Electroceramics 8, 107 (2002).

132 Ziese M, Bollero A, Panagiotopoulos I, Moutis N. Appl Phys Lett 88, 212502 (2006).

133 Deng C, Zhang Y, Ma J, Lin Y, Nan CW. J Appl Phys 102, 074114 (2007).

134 Ryu S, Park JH, Jang HM. Appl Phys Lett 91, 142910 (2007).

135 He HC, Wang J, Zhou JP, Nan CW. Adv Funct Mater 17, 1333 (2007).

136 Zhong XL, Wang JB, Liao M, Huang GJ, Xie SH, Zhou YC, Qiao Y, He JP. Appl Phys Lett 90, 152903 (2007).

137 Liu M, Li X, Lou J, Zheng S, Du K, Sun NX. J Appl Phys 102, 083911 (2007).

138 J. Slutsker, Z. Tan, A. L. Roytburd, I. Levin J. Mater. Res. 22(8), 2087 (2007)

139 I. Levin, J. Slutsker, J. Li, Z. Tan and A. L. Roytburd Applied Physics Letters 91, 062912 (2007).

140 S. Ren, R. M. Briber and M. Wuttig Applied Physics Letters 93, 173507 (2008).

141 R. Muralidharan, N. Dix, V. Skumryev, M. Varela, F. Sanchez and J. Fontcuberta Journal of Applied Physics 103, 07E301 (2008).

142 J. X. Zhang, J. Y. Dai, W. Lu, H. L. W. Chan, B. Wu and D. X. Li J. Phys. D: Appl. Phys. 41, 235405 (2008).

143 A. Artemev, J. Slutsker and A. L. Roytburd Acta Materialia 53, 3425 (2005).

144 J. Slutsker and A. Roytburd Phase Transitions 79, 1083 (2006).

145 S. V. Yanina and C. B. Carter Mat. Res. Soc. Symp. 620, M9.4.1 (2002).

146 L. Yan, J. F. Li, D. Viehland Philos. Mag., DOI: 10.1080/14786430902967702 (2009).

147 L. Yan, F. M. Bai, J.F. Li, and D. Viehland Journal of the American Ceramic Society 92, 17. (2009)

148 D. A. Porter and K. E. Easterling, “Phase transformation in metals and alloys”, Chapman & Hall, (1992)

149 S. P. Crane, C. Bihler, M. S. Brandt, S. T. B. Goennenwein, M. Gajek and R. Ramesh Journal of magnetism and magnetic Materials 321, L5 (2009)

150 N. Ortega, P. Bhattacharya, R. S. Katiyar, P. Dutta, A. Manivannan, M. S. Seehra, I. Takeuchi and S. B. Majumder J. Appl. Phys. 100, 126105 (2006).

151 J. X. Zhang, J. Y. Dai, C. K. Chow, C. L. Sun, V. C. Lo and H. L. W. Chan Applied Physics letters 92, 022901 (2008).

152 J. Das, Y. Y. Song, N. Mo, P. Krivosik and C. E. Patton Adv. Mater. 21, 2045 (2009).

153 Yun KY, Noda M, Okuyama M, Seaki H, Tabata H, Saito K. J Appl Phys 96, 3399 (2004).

154 Soliman Selim M, Turky G, Shouman MA, El-Shobaky GA. Solid State Ionics 120, 173 (1999).

155 Wang JL. Thesis, University of Maryland, College Park (2005).

156 Wang YC, Ding J, Yi JB, Liu BH, Yu T, Shen ZX. Applied Physics Letters 84, 2596 (2004).

157 Dorsey PC, Lubitz P, Chrisey DB, Horwitz JS. Journal of Applied Physics 79, 6338 (1996).

158 Suzuki Y, van Dover RB, Gyorgy EM, Phillips JM, Korenivski V, Werder DJ, Chen CH, Cava RJ, Krajewski JJ, Peck Jr. WF, Bo KB. Applied Physic Letters 68, 714 (1996).

159 Suzuki Y. Annu Rev Mater Res 31, 265 (2001).

160 Huijben, M., Rijnders, G., Blank, D. H. A., Bals, S., van Aert, S., Verbeeck, J., van Tendeloo, G., Brinkman, A. & Hilgenkamp, H., Nature Materials 5, 556-560 (2006).

161 Reyren, N., Thiel, S., Caviglia, A. D., Fitting Kourkoutis, L., Hammerl, G., Richter, C., Schneider, C. W., Kopp, T., Ruetshci, A. S., Jaccard, D., Gabay, M., Muller, D. A., Triscone, J. M. & Mannhart, J., Science 317, 1196-1199 (2007).

162 Wu, Y., Cheng, G., Katsov, K., Sides, S. W., Wang, J., Tang, J., Fredrickson, G. H., Moskovits, M. & Stucky, G. D., Nature Materials 3, 816-822 (2004).

163 Ramesh, R. & Spaldin N. A., Nature Materials 6, 21-29 (2007).

164 MacManus-Driscoll, J. L., Zerrer, P., Wang, H., Yang, H., Yoon, J., Fouchet, A., Yu, R., Blamire, M. G. & Jia, Q,. Nature Materials 7, 314-320 (2008).

165 Fiebig, M., J. Phys. D: Appl. Phys. 38, R123-R152 (2005).

166 Cheong, S. W. & Msotovoy M., Nature Materials 6, 13-20 (2007).

167 Yan, L., Xing, Z. P., Wang, Z. G., Wang, T., Lei. G. Y., Li, J. F. & Viehland, D., Applied Physics Letters 94, 192902 (2009).

168 Guiton, B. S. & Davies, P. K., Nature Material 6, 586-591 (2007).

169 Ni, Y., Rao, W. & Khachaturyan, A. G., Nano Letters 9, 3275-3281 (2009).

170 Pan, Z., Alem, N., Sun, T. & Dravid V. P., Nano Letters 6, 2344-2348 (2006)

171 Zhai, J., Xing, Z., Dong, S., Li, J. F. & Viehland, D., Applied Physics Letters 88, 062510 (2006).

172 Liu, M., Obi, O., Lou, J., Chen, Y., Cai, Z., Stoute, S., Espanol, M., Lew, M., Situ, X., Ziemer, K. S., Harris V. G. & Sun, N. X., Advanced Functional Materials 19, 1826-1831 (2009).

173 Bhame, S. D. & Joy, P. A., Journal of Applied Physics 100, 113911 (2006).

Permissions Letter

Ref # 09-29540

DATE: Wednesday, December 16, 2009

TO: Li Yan
213 Holden Hall
Virginia Tech
Blacksburg, VA 24060

FROM: Elizabeth Sandler, Rights and Permissions
RE: Your request for permission dated 12/14/09

Permission is valid for use of the following AAAS material only:
Fig 3A from Zheng et al., SCIENCE 303:661 (2004)
In the following work only:
In Chapter 3, TWO PHASE MAGNETOELECTRIC EPITAXIAL COMPOSITE THIN FILMS published by VIRGINIA TECH/UMI
FEE: Permission fees are waived in this instance. AAAS reserves the right to charge for reproduction of AAAS controlled material in the future.

Regarding your request, we are pleased to grant you non-exclusive, non-transferable permission, to republish the AAAS material identified above in your work identified above, subject to the terms and conditions herein. We must be contacted for permission for any uses other than those specifically identified in your request above.

The following credit line must be printed along with the AAAS material: "From [Full Reference Citation]. Reprinted with permission from AAAS."

All required credit lines and notices must be visible any time a user accesses any part of the AAAS material and must appear on any printed copies and authorized user might make.

This permission does not apply to figures / photos / artwork or any other content or materials included in your work that are credited to non-AAAS sources. If the requested material is sourced to or references non-AAAS sources, you must obtain authorization from that source as well before using that material. You agree to hold harmless and indemnify AAAS against any claims arising from your use of any content in your work that is credited to non-AAAS sources.

If the AAAS material covered by this permission was published in Science during the years 1974 - 1994, you must also obtain permission from the author, who may grant or withhold permission, and who may or may not charge a fee if permission is granted. See original article for author's address. This condition does not apply to news articles.

The AAAS material may not be modified or altered except that figures and tables may be modified with permission from the author. Author permission for any such changes must be secured prior to your use.

Whenever possible, we ask that electronic uses of the AAAS material permitted herein include a hyperlink to the original work on AAAS's website (hyperlink may be embedded in the reference citation).

AAAS material reproduced in your work identified herein must not account for more than 30% of the total contents of that work.

AAAS must publish the full paper prior to use of any text.

AAAS material must not imply any endorsement by the American Association for the Advancement of Science.

This permission is not valid for the use of the AAAS and/or Science logos.

AAAS makes no representations or warranties as to the accuracy of any information contained in the AAAS material covered by this permission, including any warranties of merchantability or fitness for a particular purpose.

If permission fees for this use are waived, please note that AAAS reserves the right to charge for reproduction of this material in the future.

Permission is not valid unless payment is received within sixty (60) days of the issuance of this permission. If payment is not received within this time period then all rights granted herein shall be revoked and this permission will be considered null and void.

This Permission may not be amended except by written document signed by both parties.
The terms above are applicable to all permissions granted for the use of AAAS material. Below you will find additional conditions that apply to your particular type of use.

FOR A THESIS OR DISSERTATION
If you are using figure(s)/table(s), permission is granted for use in print and electronic versions of your dissertation or thesis. A full text article may be used in print versions only of a dissertation or thesis.

Permission covers the distribution of your dissertation or thesis on demand by ProQuest / UMI, provided the AAAS material covered by this permission remains in situ.

If you are an Original Author on the AAAS article being reproduced, please refer to your License to Publish for rules on reproducing your paper in a dissertation or thesis.

Questions about these terms can be directed to the AAAS Permissions department permissions@aaas.org.